ParisTech
INSTITUT DES SCIENCES ET TECHNOLOGIES
PARIS INSTITUTE OF TECHNOLOGY

MINES ParisTech

École doctorale n° 364 : Sciences fondamentales et appliquées

# Doctorat ParisTech

# T H È S E

**pour obtenir le grade de docteur délivré par**

## l'École nationale supérieure des mines de Paris

### Spécialité " Mécanique Numérique "

*présentée et soutenue publiquement par*

**Zhigang LIU**

le 23 Avril 2012

# Numerical and experimental study of AZ31-O magnesium alloy warm sheet forming

Directeur de thèse : **Michel BELLET**

Co-Directeur de thèse : **Elisabeth MASSONI**

**Jury**

| | |
|---|---|
| **Mme Salima BOUVIER**, Professeur, Robertval , Université technologique de Compiégne | Rapporteur |
| **M.Tudor BALAN**, Maître de conférences – HDR, LEM3, Arts et Métiers ParisTech | Rapporteur |
| **M. Jean-Claude GELIN**, Professeur, ENSMM | Examinateur |
| **M. Patrice LASNE**, Ingénieur, Transvalor | Examinateur |
| **Mme Elisabeth MASSONI**, Maître de recherche, CEMEF, Mines ParisTech | Co-Directeur de thèse |
| **M. Michel BELLET**, Professeur, CEMEF, Mines ParisTech | Directeur de thèse |

T H È S E

**MINES ParisTech**
**Centre de Mise en Forme des Matériaux**
Rue Claude Daunesse B.P.207, 06904 Sophia Antipolis Cedex, France

# Abstract

Lightweight materials have been studied widely at present. Because weight reduction while maintaining functional requirements is one of the major goals in industries in order to save materials, energy and costs, etc. As the lightest structural alloys, magnesium alloys offer great potential to displace the most commonly used materials, because its density is about 2/3 of aluminum and 1/4 of steel. However, due to HCP (Hexagonal Close-Packed) crystal structure, magnesium provides only limited ductility for cold forming operations. But its formability improved obviously at elevated temperature. In this project, the material is AZ31-O magnesium alloy sheet, including 3% aluminum and 1% zinc. The sheet thickness is 1.2mm. The thermal ductility and formability of AZ31 are studied deeply by experiments and finite element simulations.

Warm tensile tests are performed in laboratory to study ductility of AZ31 magnesium alloy, the temperature and strain rate influence are included in all tests. The test reliability is validated at the beginning. The analysis result shows that the ductility is enhanced with temperature increasing and strain rate decreasing, the hardening and softening phenomenon both happen in the forming tests, the softening phenomenon is obvious with temperature increasing. Moreover, three kinds of specimens are used with various orientations with respect to the rolling direction in order to study material anisotropy property. The experiment results obviously indicate that the material shows anisotropy in lower temperature, but anisotropy decreases with temperature increasing. The anisotropy is much less obvious over $200^0$C. So, the anisotropic property is not considered in this project. The true stress and true strain data are derived from the load stroke data initially getting from experiment. The constitutive equations are identified with stress and strain data in order to describe the deformation behavior. Two kinds of behavior laws are used in the project, i.e., power law and Gavrus law. The power law which just include strain hardening exponent $n$ and strain rate sensitivity exponent $m$ can only fit well with experimental curves at the work hardening stage. Gavrus law including eight parameters and two parts, i.e., hardening and softening, can fit well with experimental curves at the hardening and softening stage despite of discrepancy. The genetic algorithm has been used to obtain the global optimal fitting parameters. The simple tensile test simulations are also performed in simulation to validate and prove the effectiveness of the models.

Warm Nakazima tests with hemisphere punch are performed to study forming limits of AZ31 magnesium alloy. These tests are carried out with Dartec® hydraulic tension testing machine in laboratory. Six kinds of specimens are used and each specimen represents a strain path. Three temperatures and two test velocities are considered in these tests in order to analyze forming influence parameters. The ARAMIS strain measurement system is used to obtain the principal strains (major strain and minor strain). Three types of blanks are obtained after experiment, i.e., safe, necking and fracture specimens respectively. Finally, the FLD (Forming Limit Diagram) is obtained and the comparison distinctly shows that the formability is better at higher temperature. Then the experimental influence parameters have been taken into account in order to analyze their respective influence on formability, e.g., temperature, velocity, lubricant and strain path, etc. The detailed analysis results are presented in the thesis. Moreover, the forming limits predictions are performed in M-K model. The prediction FLD with M-K model have compared with experiment FLD at various temperature and imperfection status. It is clearly shown that the curves near the plane strain state fit much better, and the curves fit better at $300^0$C. However, the tendency of experimental and theoretical FLD clearly indicates the same conclusion, i.e. the formability is better at higher temperature.

Finite element simulation analysis is a powerful tool in the metal forming process and virtual manufacturing field. The simulation is more and more closed with reality following the development of theory and application. Firstly, the hemisphere punch deep drawing simulations are performed in FORGE® and ABAQUS®. Punch forces, temperature and thickness distributions are compared between simulations and experiments. The punch load results indicate that the simulation curves are higher than experimental curves. The temperatures located at the punch radius zone are higher than another zone during the process. In the thickness distribution, maximum thinning has been observed in punch radius zone for both simulation and experiment. However, less thickening and more thinning has been observed in the simulation as compared with experiments. In addition, the simulation conducted in FORGE and ABAQUS are compared in order to study the difference of various finite element simulation code. The comparison shows that the curve from simulation is higher than experimental curve. But the discrepancy between simulation and experiment is different in this two simulation software. The discrepancy increases with temperature in ABAQUS. Secondly, the damage behavior are studied in FORGE, the default damage model is Cockcroft & Latham model. But the damage prediction with this model is not precise because it does not consider the deformation history. Since the Lemaitre damage model with

several damage parameter is introduced. The damage parameters obtained from warm tensile test simulation are used directly in deep drawing simulation based on the assumption that the damage mechanism is not variable with different forming process for same material. The damage values with deformation path are compared at $200^0$C and $300^0$C. It is clearly shown that the damage value is lower at higher temperatures, and there is no obvious fluctuation for damage value at each temperature.

Finally, the cross-shaped deep drawing cup simulation which is a benchmark of NUMISHEET 2011 conference is performed with FORGE. The objective of this benchmark is to validate the capability of numerical simulation for a warm forming process. This warm forming process simulation is a coupled thermal-deformation analysis considering the effect of temperature and strain-rate on material properties. The punch load, thickness and temperature distribution are obtained and compared for each simulation. The meshing influence is also studied in simulation with various mesh sizes. In the punch load comparison, the punch loads have not much difference with various mesh size, and there is slight fluctuation for each punch force curve especially at high displacement. For the thickness and temperature distribution, the thickening occurs at flange zone and thinning at cup wall zone. The maximum thinning is observed at the die corner radius for both punch displacement. The temperature distributes gradually along the wall during forming process. And there are no obvious temperature changes at the punch radius and die radius zone. Furthermore, this benchmark simulation results (FORGE) are also compared with other various simulation software in conference, such as explicit method (LS-Dyna®, Radioss®, JSTAMP®, Dynaform®) and implicit method (ABAQUS, FORGE). The CPU time is also compared in this case, and the explicit method takes less time than implicit method. The detailed analysis results are presented in this thesis.

**Keywords:** Magnesium alloy, AZ31, Thermo mechanical experiment, Nakazima warm stamping test, Formability, Finite element method.

# Table of contents

# Chapter 1 Introduction

## Contents

# 1. General introduction

In modern manufacturing engineering, weight reduction while maintaining functional requirements is one of the main goals in such as automotive, appliance, aircraft and electronics industries in order to save fuel consumption, materials, and reduce environment damage, etc [1]. Magnesium alloys offer great potential to reduce weight by displacing the most commonly used materials, because its density is about 2/3 of aluminum and 1/4 of steel [2]. Magnesium alloys have excellent specific strength and stiffness, high damping capacity, and high recycle ability [3]. Based on these superior properties and combinative requirements, the research and development of magnesium alloys have increased overwhelmingly for practical industrial application during the past two decades [4]. In terms of process difference, magnesium alloys can be divided into cast magnesium alloys and wrought magnesium alloys. It also can be classified by the alloy additional components such as AZ series (Mg-Al-Zn), ZK series (Mg-Zn-Zr), AM series (Mg-Al-Mn), etc [3]. Comparing with cast magnesium alloys, wrought magnesium alloys have more promising perspective of application, that is why the researches are increasingly attracting the attention of wrought magnesium alloys. Nowadays, the magnesium alloy research interests are mainly focused on improving specific strength, ductility and creep resistance, etc (Fig.1) [4].

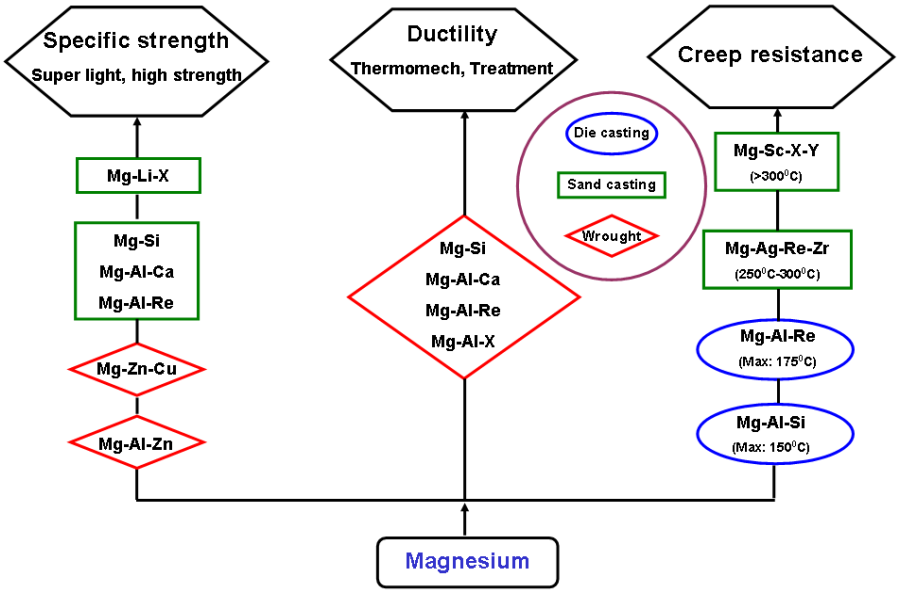


Fig.1. Direction of the magnesium alloy development.

In micro aspect, Magnesium alloy has HCP (Hexagonal Closed-Packed) crystal structure, and shows low ductility for cold forming process. Gehrmann *et al.* [5] studied magnesium alloy ductility at room temperature through analyzing the role of texture on the deformation mechanisms. They found that magnesium has limited ductility and poor formability at room

temperature due to an insufficient number of operative slip and twinning systems. There are three different directions in the basal plane, only two of them are independent. Slip on other non-basal systems have larger critical resolved shear stresses (CRSS) and therefore are harder to operate at room temperature. Doege *et al.* [6] reported that magnesium alloy additional slip planes can be activated thus increasing ductility and decreasing the yield stress at temperature above $225^0$C (Fig.2). The micro deformation mechanism details will be explained in following sections.

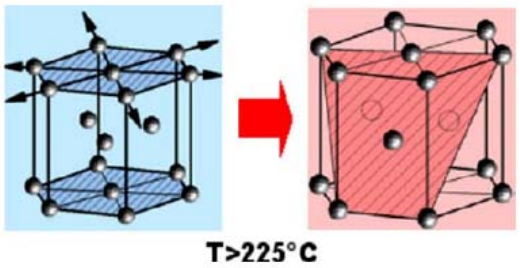


Fig.2. Activation of additional sliding planes for magnesium at elevated temperatures [6].

In macro aspect, many researches are being done to gain the knowledge about the specific deformation behaviours for magnesium alloy parts. Especially, the flow curves and their dependencies from temperature and strain rate have to be carefully studied prior to all forming experiments, specific effects like work softening have to be taken into account when theoretically describing the forming behaviour [7]. As the cold forming of magnesium alloy is difficult to perform, magnesium alloy sheet has to be carried out at elevated temperatures. But hot forming tests are more complicated than cold forming, because it involves more influences such as temperature, friction, velocity and tool geometry, etc. It is challenging that it is necessary to consider the comprehensive influence between rheology, tribology, metallurgy and thermal effects [8]. Therefore, it is important to evaluate magnesium alloy behavior with a simple hot forming experiment set-up. The uniaxial tensile test is commonly used to obtain material data because of simple implementation compared with other tests and classic metal forming theories are used maturely to convert the results into a suitable material model. Moreover, deep drawing test is also commonly used to study the thermal formability of material in laboratory and industry. In the hot deep drawing tests, due to the significant sensitivity of formability to temperature, the temperature controlling play an important role in the experiment, partially heated blank holders are able to control the forming process very accurately especially for complex geometries [2].

The numerical simulation is also widely studied in the sheet metal forming process to reduce design time cycle and manufacturing costs in industry nowadays. As in the numerical simulations, the FEM (Finite Element Method) is the most popular used method. The application of finite element method in sheet metal forming field can be traced back to the work by Alexander Hrennikoff (1941) and Richard Courant (1942), etc [9]. Its initial application is mainly used to solve elasticity and structural problems. With the devolvement in industrial application, finite element method can solve complex non-linear and dynamic problems now. In recent years, there were some achievements to study formability of AZ31 magnesium alloy using finite element method. Takuda *et al.* [10] have extensively investigated material properties of Magnesium alloy AZ31sheets by the combination of finite element simulation with Oyane's ductile fracture criterion. The cylindrical deep drawing test and the Erichsen test have been carried out, and the numerical results have been compared with observations. The comparisons demonstrate the fracture initiation and the critical punch stroke are successfully predicted by simulation. Palaniswamy *et al.* [11] studied magnesium alloy sheet forming at elevated temperatures by finite element simulation using DEFORM®. And it is found that punch temperature plays a critical role in warm forming process and influence the temperature of cup walls thereby increasing the strength compared with flange. Meanwhile, the punch load comparison shows that the simulation results overestimate at each temperature. Bolt *et al.* [12] applied coupled FEM for simulating the warm sheet forming process using the commercial code MARC®, and concluded that numerical simulation results underestimated the punch load versus stroke comparing with experiment. Many other magnesium alloy numerical simulation researches have been published so far. The details of using FEM in magnesium alloy sheet forming will be presented in the following sections.

# 2. State of the art

In the last two decades, the AZ series magnesium alloy have been extensively studied and used for structural components, because of their high specific strength and good castability. Particularly, the AZ31 which contains 3% aluminium and 1% zinc is the most commonly used in industry, which is considered as the suitable magnesium alloy for the stamping process at the present [13].

## 2.1 Microstructure of AZ31 magnesium alloy

As HCP (Hexagonal Closed-Packed) crystal structure material, Mg shows much limited ductility compared with Al, whose crystal structure is FCC (Face-Centered Cubic). Fig.3 shows slip planes of Mg and their critical resolved shear stress (CRSS). Slip system of Mg is composed of three slips, which are parallel to basal, prismatic and pyramidal slips. Since the CRSS of pyramidal slip is much larger than that of the other slips, it is difficult to activate pyramidal slip at room temperature. Thus, slip in the *c*-axis direction (the vertical direction in Fig.3) can not be expected in Mg crystal at low temperature [14].

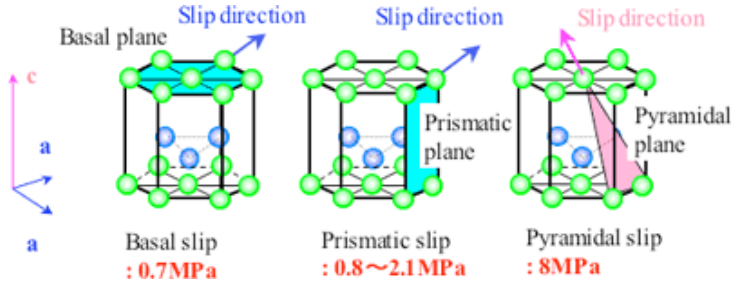


Fig.3. Slip planes of magnesium and their critical resolved shear stress [14].

Due to the limited slip systems of magnesium alloy in low temperature, Barnett [15] studied intensively the mechanisms of twinning and the ductility for magnesium alloys. Deformation twinning is often observed in polycrystalline Mg to compensate for the insufficiency of independent slip systems. The most common twinning modes are $\{1\ 0\ \bar{1}\ 2\}$ and $\{1\ 0\ \bar{1}\ 1\}$ twinning. The twinning of Mg is inhomogeneous, and different modes of twinning are not initiated simultaneously. Generally, single twinning mode can not completely activate plastic deformation. At room temperatures, twinning deformation is localized, which leads to low ductility for Magnesium alloys. Al-samman *et al.* [16] studied the dynamic recrystallization of magnesium deformation. It is found that dynamic recrystallization plays an important role in the deformation of magnesium alloy, especially at temperature of 200°C, where magnesium perform a transition from brittle to ductile behaviour. In addition, the influence of deformation conditions on the dynamic recrystallization (DRX) behavior and texture evolution have been examined by uniaxial compression tests. AZ31 magnesium alloy shows virtually no grain growth at elevated temperatures (i.e., $400^0$C), even at low strain rates ($10^{-4}$ $s^{-1}$), which is contrast to pure magnesium deformation mechanism (Fig.4). In short, the magnesium alloy AZ31 deformation is influenced significantly by forming condition. The micro mechanisms are still being studied by theoretical and experimental method [4].

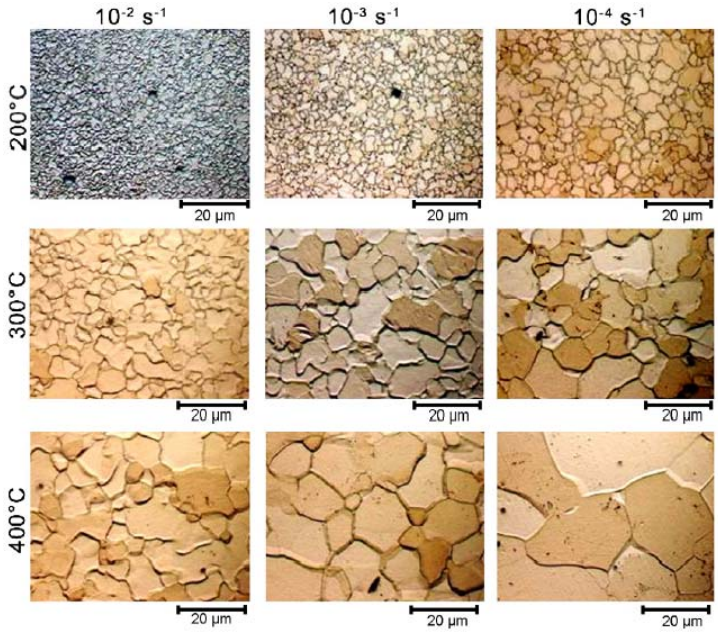


Fig.4. Optical micrographs specimens illustrating the DRX microstructure under uniaxial compression at various deformation conditions ranging from 200 to 400$^0$C and $10^{-2}$ to $10^{-4}$ $s^{-1}$ [16].

## 2.2 Anisotropy and strain hardening

Kaiser *et al.* [17] studied the anisotropic properties of magnesium sheet AZ31 by tensile test in 1.0mm and 1.6mm thickness. It is found that AZ31 exhibits obvious anisotropy at room temperature, which could be explained with the rolling texture. But it is shown a declining anisotropy at higher temperatures. The similar experimental results have been obtained between 150$^0$C and 200$^0$C, where the yield stress is approximately half of its corresponding value at room temperature in both transverse direction and rolling direction, even the anisotropy is not observed anymore at 250$^0$C (Fig.5).

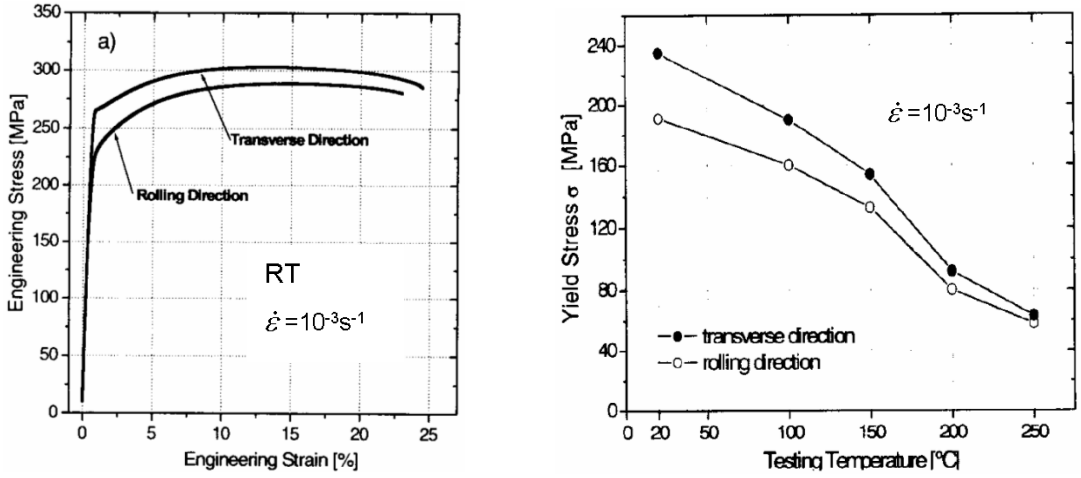


Fig.5. Stress-strain curves and yield stress for rolling direction and transverse direction [17].

The strain hardening is distinct property of plastic deformation comparing with elastic deformation. Lou *et al.* [18] studied intensively hardening evolution of AZ31B magnesium sheet in combination of mechanical and microstructural techniques. It is found that the AZ31 monotonic deformation behavior involves multiple deformation mechanisms, i.e., basal slip, non-basal slip and twinning. They test in four strain path to interpret the different deformation mechanisms in micro aspect, i.e., uniaxial tensile test, in-plane compression, in-plane tension test and in-plane simple shear. For example, uniaxial tensile deformation is dominated initially by basal slip with other contributions of non-basal slip and twinning for annealed AZ31 sheet. And then, it changes progressively to non-basal slip as the flow stress rises.

In 2005, Agnew and Duygulu [19] proposed an outstanding report about plastic anisotropy and the role of non-basal slip in magnesium alloy AZ31B forming. A polycrystalline approach involving both experimental and theoretical simulation is used to explain AZ31B magnesium alloy deformation behavior, and this polycrystal plasticity modeling has still been studying so far. It is mentioned that the AZ31 flow strength decreases with increasing temperature, and the strain hardening exponent is essentially constant up to $200^0$C. On the other hand, they give quantitative analysis for strain rate sensitivity, which increases from 0.01 to 0.15 when temperatures arise from room temperature to $200^0$C. This result suggests that the dramatically improved strain rate sensitivity may be the most important macroscopic constitutive parameter responsible for inducing the formability of magnesium alloys at high temperatures. In addition, the high r-values observed at low temperatures drop rapidly with increasing temperature. It is not suggested that this change in r-value is directly responsible for the increasing formability. However, it provides indirect evidence that there is a change in the underlying deformation mechanisms. The details can be referred in the publication and similar bibliography [19, 2, 5].

## 2.3 The mechanical behavior of AZ31 magnesium alloy

As mentioned in the introduction, the restricted cold forming capability is a fundamental disadvantage of magnesium because of its Hexagonal Closed-Packed (HCP) structure and the associated insufficient slip planes at low temperature. The intuitional way is to activate the additional slip system in order to using magnesium sheet metal to produce complex components in industry. The main solution is forming at elevated temperature. Fig.6 illustrates the temperature dependency of the flow curve for the magnesium alloy AZ31B (initial thickness $t_0$ = 1.3 mm) [4].

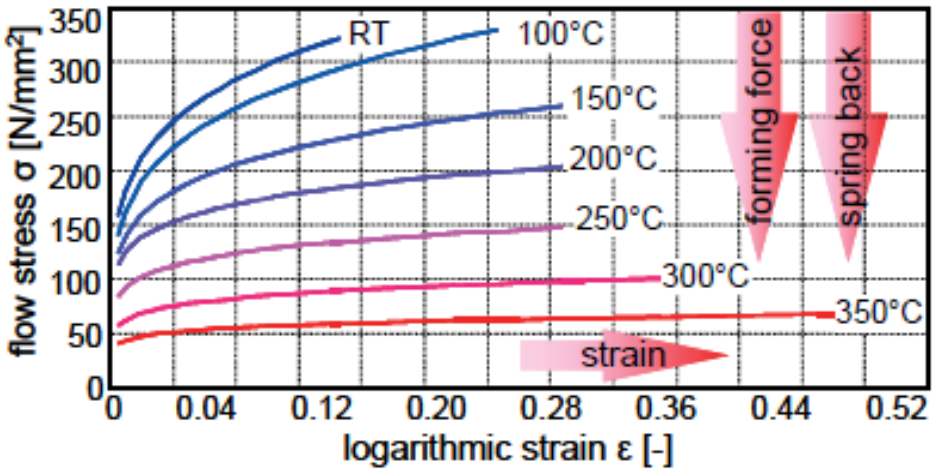


Fig.6. Effect of elevated temperatures on the flow curve of magnesium [4].

The above figure demonstrates clearly the flow stress and strain relationship at various temperatures. Firstly, elevated temperatures contribute to improve ductility and increase forming capability, and secondly reduce the yield point of the material therefore decrease the forming forces. Besides, the spring back behavior decreases with temperature increasing.

The specific influences in forming flow stress have also been studied extensively. Jager *et al.* [20] reported the tensile properties of AZ31 Mg alloy sheets at various temperatures in 2004. It is found that the yield stress and the maximum flow stress decrease dramatically with increasing temperature. The yield stress decrease from 230MPa at room temperature to about 7.5MPa at 350$^0$C, the maximum stress decrease from 343MPa at room temperature to about 14MPa at 350$^0$C, and the ductility of AZ31 increases significantly with temperature, reaching about 420% at 400$^0$C (Fig.7). The strain hardening rate also decreases with increasing temperature, and it becomes very close to zero at high temperatures.

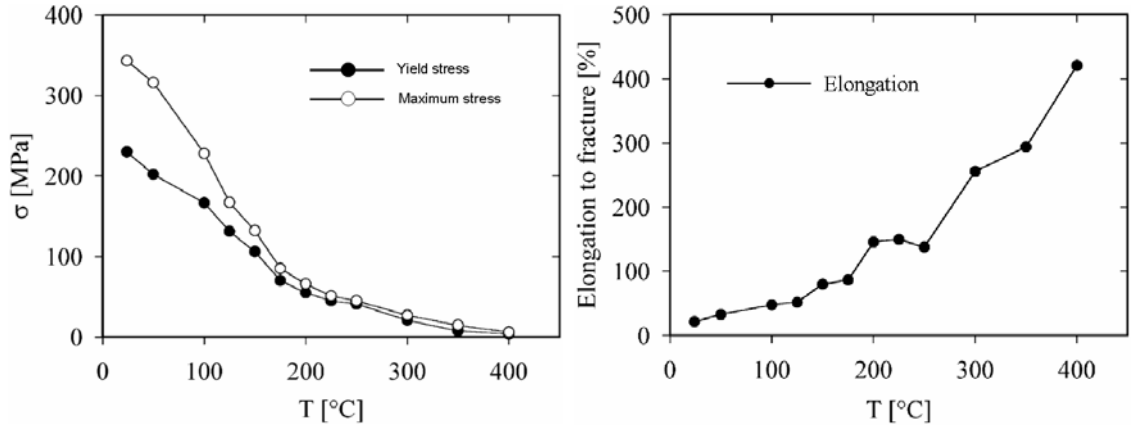


Fig.7. Stress and elongation to fracture with various temperatures [20].

Moreover, Doege and Droder [21] also studied the formability of magnesium wrought alloy AZ31B and obtained influence of strain rate on flow stress for the determination of strain rate sensitivity by tensile tests. Fig.8 shows the influence of testing strain rate on flow stress for AZ31 at 200°C. It is apparently shown that the flow stress exhibit a considerable increasing when the strain rate rise from 0.002 $s^{-1}$ to 2.0 $s^{-1}$. But the effect is less significant if the experiments are performed at lower temperature. Furthermore, the tensile tests show that the maximum elongation is lower with strain rate increasing at any temperature.

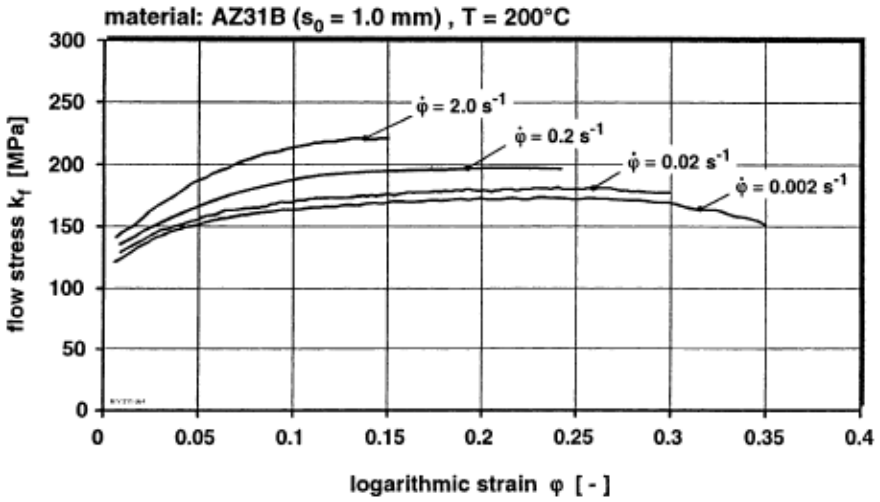


Fig.8. Strain rate dependent flow curves of AZ31B determined in the uniaxial tensile test at $200^0$C [21].

In addition, the material behaviors have influenced in the yield locus. Naka *et al.* [22] have studied significantly the effects of strain rate, temperature and sheet thickness on yield locus of AZ31 magnesium alloy sheet. It is found that the size of yield locus drastically decreases with increasing temperature and decreasing strain rate. They test two kind specimens in 0.5mm and 0.8mm thickness. And they found sheet thickness has no influence on the yield locus, which is contrast with the temperature and strain-rate dependence of the yield locus. In the study, four yield criteria have been used in yield locus prediction, i.e., von Mises yield criterion, Hill yield criterion, Logan-Hosford yield criterion and Barlat'2000 yield criterion. Fig.9 shows the comparison of experimentally obtained yield loci of Mg alloy sheet with those predicted by these four criteria at various temperatures. The shape of the yield locus is far from the predictions calculated by the yield criterion of von Mises and Hill. Instead of these, the yield criterion of Logan-Hosford and Barlat is a better choice for the accurate description of biaxial tension stress-strain responses at high temperature.

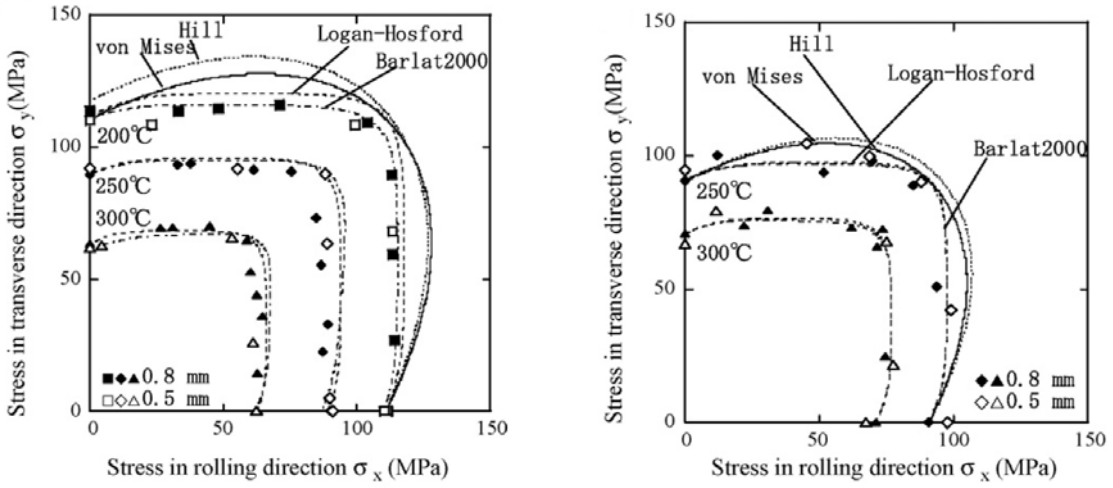


(a) $\dot{\varepsilon}$ =$10^{-3}$ $s^{-1}$ (b) $\dot{\varepsilon}$ =$10^{-2}s^{-1}$

Fig.9. Comparison of experimentally obtained yield loci of Mg alloy sheet with those predicted by the von Mises, Hill, Logan-Hosford and Barlat criteria ($t_0$ = 0.8 and 0.5mm) [22].

## 2.4 The constitutive relationship of AZ31 magnesium alloy

The constitutive models of AZ31 magesium alloy have been studied extensively to describe material behavior so far. In 2008, Cheng *et al.* [23] reported a flow stress equation of AZ31 magnesium alloy sheet during warm tensile deformation. They proposed a new mathematical model containing a softening item through the uniaxial warm tensile tests at various temperatures and strain rate. The equation can be divided into two parts. Firstly, it is based on power law at the strain hardening stage. The expression is described as follow:

$$\sigma = K\varepsilon^n \dot{\varepsilon}^m \tag{1.1}$$

Where, the parameter $K$ is the strength coefficient, $n$ is the strain hardening exponent, and $m$ is the strain rate sensitivity exponent. The parameters are identified by mathematical fitting after experiment. The identified parameter equations are following:

$$n = 0.031 + 0.031\log\dot{\varepsilon} + \frac{97.1}{T} \tag{1.2}$$

$$m = \frac{-145.263}{T} + 0.377 \tag{1.3}$$

$$K = -156.4 + 9.1\log\dot{\varepsilon} + \frac{244980.4}{T} \tag{1.4}$$

$$[0.02 \le \varepsilon \le 0.3,\ 10^{-4} \le \dot{\varepsilon} \le 10^{-1}\ (s^{-1}),\ 423 \le T \le 573\ (K)]$$

The comparison of experimental curves and calculated curves have been conducted intensively and it demonstrates that the equation can describe appropriately the strain hardening behavior, but the material has obvious softening phenomenon at higher temperature,

the equation can not describe the softening behavior of AZ31. Therefore, a new model including softening items is introduced as follow:

$$\sigma = 18015\varepsilon^{0.16}\dot{\varepsilon}^{0.083}\exp(-0.0078T - 0.8903\varepsilon) \tag{1.5}$$

$$[0.15 \le \varepsilon \le 0.45,\ 10^{-4} \le \dot{\varepsilon} \le 10^{-1}\ (\mathrm{s}^{-1}),\ 473 \le \mathrm{T} \le 573\ (K)]$$

The above equation includes the softening item which involves temperature and strain influence. The comparisons of experimental and calculated curve have been carried out identically. From the comparison, the flow stress calculated by the modified equation containing a softening items approaches better at the softening stage. However, there are still discrepancies on the curves, and the using condition of equation is limited.

Takuda *et al.* [24] also reported a model by means of the temperature compensated strain rate, *i.e.* the Zener-Hollomon parameter, denoted *Z*. The equation is expressed as follows:

$$\sigma_{\mathrm{y}}(MPa) = B\ln(Z/Z_0) + C \qquad Z = \dot{\varepsilon}\exp(Q/RT) \tag{1.6}$$

Where, the parameters $B$ and $C$ are the stress constant, $\dot{\varepsilon}$ is the strain rate, $Q$ is the activation energy for deformation, $R$ is the molar gas constant and $T$ is the temperature. The parameters are also identified by the mathematical fitting with experimental curves and described as follows:

$$R = 8.31\ (\mathrm{J\ mol^{-1}\ K^{-1}}),\ Q = 136\ (\mathrm{kJ\ mol^{-1}}),\ Z_0 = 109\ (\mathrm{s^{-1}}) \tag{1.7}$$

$$B = 5.8\ (\mathrm{MPa}),\ C = 33\ (\mathrm{MPa}) \tag{1.8}$$

$$[\,533 \le T \le 753\ (K),\ 8.3\times10^{-5} \le \dot{\varepsilon} \le 8.3\times10^{-2}\ (\mathrm{s^{-1}})]$$

In this report, only the proof stress was discussed, the flow stress usually varies with strain. From the comparison between experimental and fitting data, it is demonstrated that the above equation equation fits the experimental curves with temperature from 533K to 753K. It is necessary to improve the model describing the softening behaviour. So, Takuda et al. [25] derived a new constitutive model by analyzing deeply the stress-strain curves under various temperatures and strain rates. The formula is also expressed with the strain hardening exponent, n, the strain rate sensitivity exponent, m, and the strength coefficient, K. And they are given with functions of temperature. The equation expressed as follows:

$$\sigma(MPa) = K\varepsilon^{n}(\dot{\varepsilon}/\dot{\varepsilon}_0)^{m} \tag{1.9}$$

$$K = 3.24\times10^{5}/T(K) - 406 \tag{1.10}$$

$$n = A\log(\dot{\varepsilon}/\dot{\varepsilon}_0) + B\,, \quad \mathrm{A}=0.016, \quad B = 62/T(K) + 0.053 \tag{1.11}$$

$$m = -105/T(K) + 0.303 \tag{1.12}$$

$$[0.05 \le \varepsilon \le 0.7,\ 10^{-2} \le \dot{\varepsilon} \le 1.0\ (\mathrm{s^{-1}}),\ 423 \le \mathrm{T} \le 573\ (K)]$$

It is verified that the flow stresses calculated by the formula give a good fit with tensile experimental data. But the condition of equation is also limited for high temperature.

Due to the difficulty for describing constitutive relationship of material, Sheng *et al.* [26] proposed a new way to study the constitutive relationship of magnesium alloy. This model bases on the deformation mechanism of Hexagonal Closed-Packed (HCP) structure material. It reflects temperature, strain and strain rate effect by introducing Zener-Hollomon parameter. And the flow stress process has been divided into four stages. The first stage is work hardening, the hardening rate is higher than the softening rate in this stage and thus the stress increases rapidly at beginning of deformation (0.1%-1%), and then increases with a decreased rate. The second stage is stable stage, in which equilibrium is obtained between the dislocation generation and annihilation rate. Generally, this stage is short. The third stage is softening, the macro phenomenon is the stress drops dramatically with strain increasing, and the explanation in micro aspect is that large number dislocations are annihilated through the migration of a high angle boundary. And the last stage is steady stage, the stress becomes steady when a new balance is formed between softening and hardening (Fig.10).

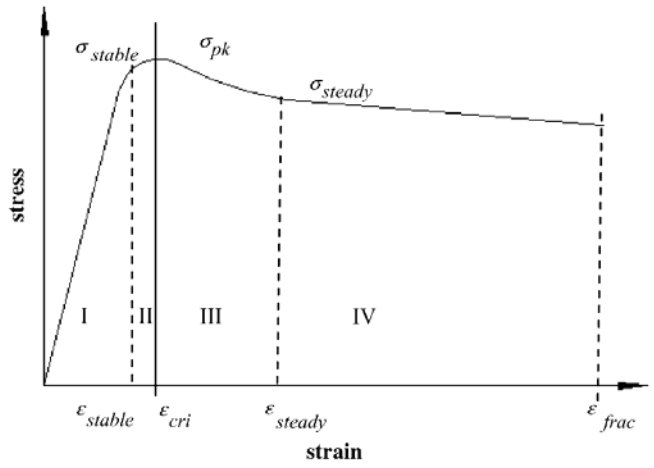


Fig.10. Typical flow stress curve at the elevated temperature for HCP structural material [26].

The Zener-Hollomon parameter denoted $Z$ is widely used to describe the material deformation behavior by temperature-compensated strain rate. The parameter expression is following:

$$Z = \dot{\varepsilon} \exp\left(\frac{Q}{RT}\right) \tag{1.13}$$

Where, the parameter $\dot{\varepsilon}$ is the strain rate, $Q$ is the activation energy for deformation, $R$ is the molar gas constant and $T$ is the temperature. In this model, every stage is expressed by

separate model which is identified by specific experiment. Finally, the material property is described by piecewise functions.

***1) Hardening and stable stage:***

The hardening behaviour can be described by Zener-Hollomon parameter while the strain hardening coefficient *n* and stress coefficient *K* are strongly influenced. Thus, the power law equation is extended to express both temperature and strain rate effect as follow:

$$\sigma = K(Z)\varepsilon^{n(Z)} \qquad [\varepsilon_{0.002} < \varepsilon < \varepsilon_{stable}] \tag{1.14}$$

In the above expression, $K(Z)$ and $n(Z)$ are represented by following two order polynomial equations respectively.

$$K(Z) = A_1\left[\log\left(\frac{Z}{2}\right)\right]^2 + B_1\log\left(\frac{Z}{2}\right) + C_1 \tag{1.15}$$

$$n(Z) = A_2\left[\log\left(\frac{Z}{2}\right)\right]^2 + B_2\log\left(\frac{Z}{2}\right) + C_2 \tag{1.16}$$

Where, the constants $A_1$, $A_2$, $B_1$, $B_2$, $C_1$ and $C_2$ can be determined by regression on the experimental data. Consequently, at the stable stage, the equation is expressed as follow:

$$\sigma = \sigma_{stable} + \alpha(\varepsilon - \varepsilon_{stable}) \qquad [\varepsilon_{stable} < \varepsilon \le \varepsilon_{cri}] \tag{1.17}$$

Where, $\sigma_{stable}$ is the stress value at the end of hardening stage and $\alpha$ is the slope of stable stage which can be determined by experimental data regression analysis.

***2) Softening and steady stage***

The slope of softening is also affected by Zener-Hollomon parameter *Z* and a linear equation is given to describe the flow stress at this stage.

$$\sigma_{sf} = \sigma_{pk} + D(Z)(\varepsilon - \varepsilon_{cri}) \quad [\varepsilon_{cri} < \varepsilon \le \varepsilon_{steady}] \tag{1.18}$$

Where, $\sigma_{pk}$ is the peak stress, $\varepsilon_{cri}$ is the corresponding critical strain. $D(Z)$ is the slope of the softening slope and can be described by the following equation.

$$D(Z) = E\log(\frac{Z}{2}) + F \tag{1.19}$$

Consequently, at the steady stage, the equation is following:

$$\sigma = \sigma_{sft} + G(Z)(\varepsilon - \varepsilon_{steady}) \quad [\varepsilon_{steady} < \varepsilon \le \varepsilon_f] \tag{1.20}$$

Where, $\sigma_{sft}$ is the stress at the end of softening stage and $\varepsilon_{steady}$ is the strain for the steady stage beginning. $G(Z)$ is the slope of the steady slope and can be described as follow:

$$G(Z) = H \log(\frac{Z}{2}) + I \tag{1.21}$$

Where, all of constants in above equations can be determined by experimental data linear regression analysis. Transfer of different stages is described as follow:

$$\varepsilon_i(Z) = L_i \log\left(\frac{Z}{2}\right) + M_i,\ i \in \{stable,\ cri,\ steady,\ frac\} \tag{1.22}$$

Finally, the comparisons are conducted between experimental curves and model fitting curves by verifying three experimental results, and it is found that the flow stress predicted by the proposed model match well with that measured from experiments.

## 2.5 Formability of AZ31 magnesium alloy

The formability of AZ31 magnesium alloy has been studied widely and numerous achievements have been reported in the last two decades. In 2006, Zhang *et al.* [27] studied formability of magnesium alloy AZ31 sheets at warm working conditions and proposed the forming limits diagram of material at various temperature (Fig.11 (a)). The material formability is mainly evaluated by Limit Drawing Ratio (LDR) tests and Limit Dome Height (LDH) tests between room temperature and $240^0$C. It is concluded that LDR increases remarkably with temperatures, while LDH does not seem to increase much with temperatures. Meanwhile, Fuh-Kuo Chen *et al.* [28] also conducted the same experiment to study forming limit of magnesium alloy AZ31 sheets (Fig.11 (b)). The experimental results indicate that AZ31 sheets exhibit poor formability at room temperature, while it is improved significantly at elevated temperatures. They also obtained the forming limit diagram at various temperatures. Both of forming limit diagram (FLD) has demonstrated obviously that the forming limit curve is higher with higher temperature, which means that AZ31 sheets can sustain more deformation at higher forming temperatures (Fig.11).

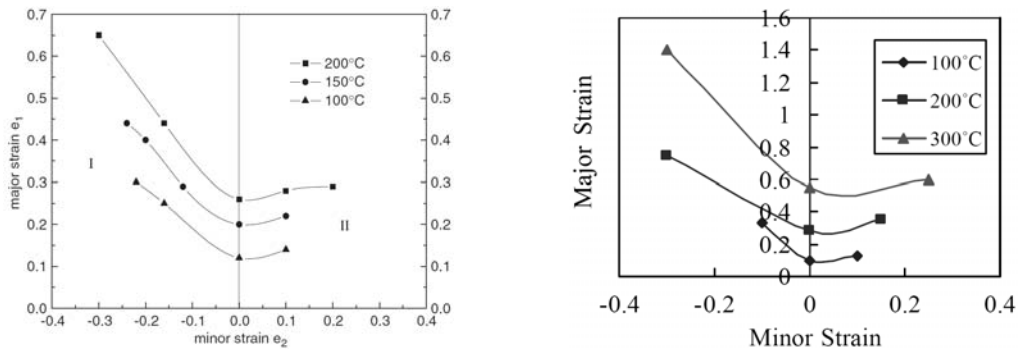


(a) (b)

Fig.11. The forming limit diagrams at various temperature [27, 28].

Doege and Droder [21] reported the formability of magnesium wrought alloys AZ31B by deep drawing test and compared the formability for several materials. It is concluded that the magnesium alloy AZ31B shows better deep drawing properties in comparison to the magnesium alloy materials AZ61B and M1 at same forming conditions. The AZ31B sheet shows excellent limit drawing ratios up to 2.52 between $200^0$C and $250^0$C. Moreover, it is also illustrated that forming velocity is more important for magnesium alloy sheet deep drawing compared to the forming of aluminum alloy $AlMg_{4.5}Mn_{0.4}$. In addition, a special deep drawing experiment with complex tool geometry have been tested and it is confirmed that the deep drawing of magnesium parts for industrial applications is possible at low temperature.

The material formability is also affected by strain rate variation. Therefore, Lee *et al*. [29] studied forming limit of magnesium alloy AZ31 sheet and deeply investigated strain rate influence by sheet forming limit experiment. The Forming Limit Diagram (FLD) is obtained at two strain rates ($0.1s^{-1}$ and $1s^{-1}$). It is concluded that the forming limit is worse with higher strain rate. And the failures occur frequently at high forming velocity in deep drawing test. The strain rate influence for Limit Dome Height (LDH) is also analyzed after experiment, it is concluded that LDH increases until strain rate of $0.1s^{-1}$, but decreases after strain rate of $0.1s^{-1}$ over $300^0$C. However, at $400^0$C, The LDH decreases consistently from $0.01s^{-1}$ to $0.5s^{-1}$. The details have illustrated thoroughly in Fig.12. In short, the strain rate is lower, the formability is better.

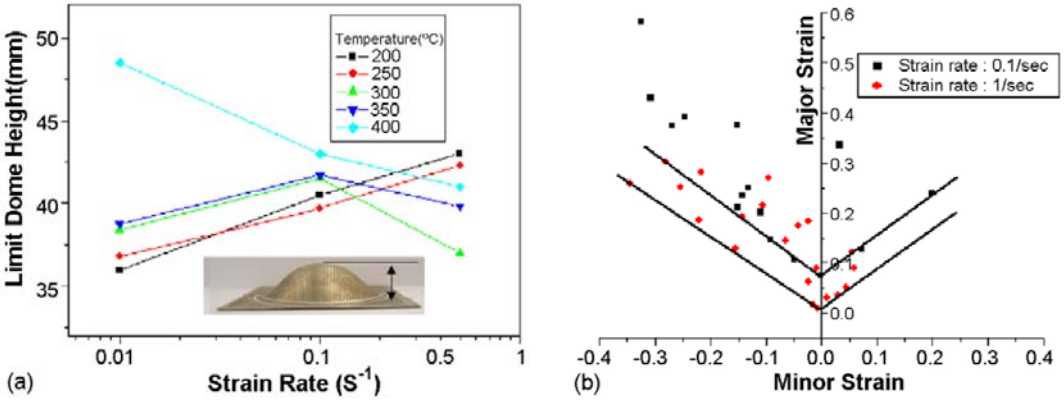


Fig.12. Limit dome height (LDH) and forming limit diagram at various strain rates [29].

The numerical simulation is also widely used to study material formability. Wang *et al*. [30] published a paper about the forming limit prediction of magnesium alloy AZ31 sheets in experimental and numerical method. In the previous studies, predicted forming limit curves (FLC) is frequently based on power law material model. However, the tensile test of

magnesium alloy AZ31 sheet shows softening phenomenon at elevated temperatures and it can not be described simply by power law, which restricts using theoretical FLC model to predict Mg formability at elevated temperatures. On the other hand, the calculated FLC also vary with yield criterion. They compared several yield models using in the numerical FLC calculation, i.e., Swift's theory, Hill's theory, Storen and Rice theory (also called vertex theory). In comparison, the large difference exists between the Hill model predicted curve and the experimental one, which indicates that the Hill model is not suitable to describe the Mg alloy FLC. Meanwhile, the Swift yield model is limited to the right side of FLD, and the vertex theory which can cover both sides of FLD is more consistent with the experimental result. Generally, few theoretical FLC models can accurately describe the Mg formability at elevated temperatures, and the experimental method is still the most accurate way to evaluate the formability of material.

## 2.6 Finite element simulation of AZ31 magnesium alloy

The finite element analysis is a comprehensive used method in AZ31 magnesium alloy forming application, and there are many achievements for the last two decades. Palaniswamy *et al.* [11] studied forming process of AZ31 sheet at elevated temperatures by finite element simulation using DEFORM® commercial software. A round cup and a rectangular pan are simulated and the model is performed under non-isothermal conditions. The punch is initialized under room temperature, and the tools and blank initial temperature are fixed separately under $150^0$C, $200^0$C, $250^0$C and $300^0$C. Then temperature, punch force and thickness distribution are intensively studied in forming processes. Finally, it is concluded that punch temperature plays a critical role in warm forming process which firstly influences the temperature of cup walls, and then increases the strength.

Fig.13 and Fig.14 shows the temperature and thickness distribution in the simulation separately. It is obviously illustrated the temperature is lower in the region of blank in contact with punch compared to the blank in contact with the die (Fig.13). This result is essential for the deep drawing process because it can increase the material capability to resist failure. Meanwhile, the maximum thinning have been observed along the cup wall at various temperatures, this result is contrary to the conventional stamping process where the maximum thinning is observed at punch radius (Fig.14). This could be due to the fact that the strength of the cup wall is not uniform in the AZ31 warm stamping forming process. In the simulation, the maximum punch load obtained from simulation is higher than the load obtained from experiment which performed by experiment lab for each corresponding temperatures. There

are probably several reasons whicj can explain this phenomenon. The details can be referred in the original publication [11].

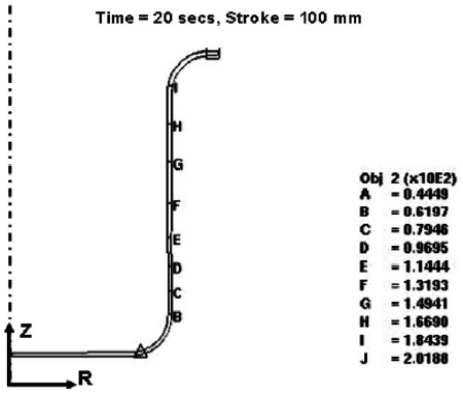


Fig.13. Temperature distribution [11].

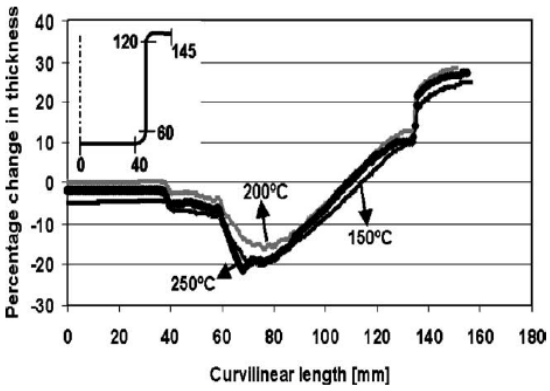


Fig.14. Thickness distribution for LDR of 2.3 [11].

Ren *et al.* [31] studied drawability of magnesium alloy AZ31 on warm deep drawing numerical simulation. It is confirmed that the most important factor affecting the deep drawability of Mg alloy sheet is temperature. Furthermore, the effect of forming velocity is much more significant at higher temperature. For instance, round cups could be formed at $150^0$C with the highest punch velocity of 6 mm/min. However, when the forming temperature is increased up to $250^0$C, it could be drawn with the highest punch velocity of 120 mm/min. Huang *et al.* [32] also studied formability of AZ31B sheets by non-isothermal deep drawing test with finite element analysis. It is concluded that the LDR is higher in the non-isothermal deep drawing simulation compared with conventional deep drawing. In addition, the lubrication effect on deep drawing process is also studied using $MoS_2$ and oil lubricant, and the conclusion is that the highest LDR is 2.63 for $MoS_2$ and 2.37 for oil at $260^0$C for 0.58mm thick AZ31B sheet.

# 3. Application

Today, magnesium alloys are recognized alternatives structural material to steel and aluminum to reduce the weight of product. In the recent years, Mg alloys have been progressively used in industrial field, such as automobile parts, aerospace parts, portable electronic devices, etc. because magnesium alloys offer much advantages such as light weight, high strength ratio, higher vibration absorption, environment friendly, etc. Thanks to the development of new forming technologies, magnesium alloy also exhibit the possibility to forming in lower temperature. In addition, the alloys improved heat resistance and strength have extended their possible range of application [33, 34].

## 3.1 Magnesium application in automotive industries

Magnesium alloy has a long history of usage as lightweight material in the field of commercial and special automotive construction. The earliest usage of magnesium alloy parts is racing vehicles in the 1920's [34]. Their lightweight and high strength to weight ratio provide many teams with a competitive advantage (Fig.15). Today, the most attraction for magnesium alloy application in automotive industry is the combination of high strength properties and low density. Although various problems meet in the application, such as poor formability at low temperature, low ductility at room temperature, creep resistance, etc., magnesium alloy propose promising potential for automotive weight reduction than currently used material.

Fig.15. Application of magnesium alloy components in motor racing industry [34].

Actually, magnesium alloys are not widely used in commercial vehicles until 1936 when the Volkswagen Beetle® was introduced. The car contains around 20Kg of magnesium in the powertrain and its maximum consumption of magnesium reach 42,000 tons per annum in 1971 [34]. However, magnesium alloy forming technology restrict it is application in automobile industry. The high cost result in a long time low development for magnesium and its alloy. But over the last two decades, there has been significant growth of magnesium with technology development [35]. Magnesium alloy have been treated as a strategic lightweight material in the automobile industry based on actual requirement such as fuel reduction, environment conservation, saving energy, etc., which is the driving force behind this growth. With the necessary technological advances in alloy performance and the continuous requirement to minimize weight and fuel consumption, many study have been doing and some achievements have been obtained in the worldwide nowadays [36].

In Europe, using magnesium as a structural lightweight material is initially led by the Volkswagen group, and then was also used by other leading automotive manufacturers such

as DaimlerChrysler (Mercedes Benz), BMW, Ford and Jaguar, etc. The Volkswagen group have proposed the plan to increase magnesium alloy usage from less than 2% recently to about 15% in the future, the magnesium alloy will include in all major groups of car components, i.e., power train, interior, body and chassis. Presently, around 14kgs of magnesium alloy are used in the Volkswagen Passat, Audi A4 and A6. All those vehicles offer about 20%-25% weight saving by using magnesium casting alloy AZ series. As a long term automotive development strategy, European have proposed a huge car project called EUCAR, in which research and development efforts for Mg alloys have been part of the development projects. The primary purpose is to reduce the weight of motor vehicles, and then reduce $CO_2$ emissions and fuel consumption. The main participation in the EUCAR project is the joint research organization established by automobile manufactures such as Fiat, Volvo, Daimler-Chrysler, Volkswagen, BMW, and universities, etc. Meanwhile, independent research organizations and component suppliers in Europe also participate in this project. Figure 16 shows a car and the places where magnesium alloys have been used or where their application continues to be considered [36-38].

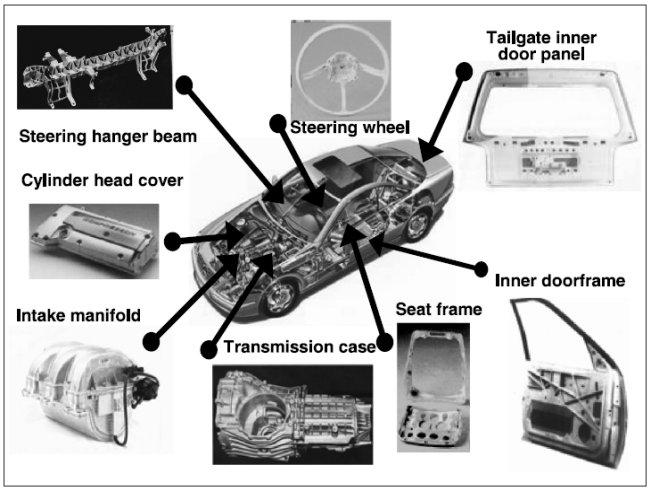


Fig.16. Application of magnesium alloys in motor vehicles [37].

In the U.S.A, the magnesium alloy parts have been used in motor vehicles led by General Motors (GM) and Ford since the 1970s. And then they jointly established the United States Council Automotive Research project called USCAR in 1992. The council worked out a plan for strengthening their competitiveness and environmental conservation, and has made many efforts to implement the plan. As part of this plan, the magnesium alloy components development project started in 2001 under the direction of the United State Automotive

Materials Partnership (USAMP). This project aims to increase the usage of Mg alloys in motor vehicle to about 100Kg in 2020 [39].

In Asia Pacific area, the usage of Mg alloys has increased incrementally initially led by Japanese automotive company. And today China is dominating the primary magnesium market due to strong price competition. The various type magnesium alloys have been widely used in all aspects of vehicle. For instance, the Mg alloy AZ series is the most common used material in various types of covers and cases of vehicle, Mg alloys AM50 and AM60 are mainly used for steering wheel cores with higher ductility and impact resistance, and Mg alloys which contain such as rare earth elements and calcium to provide high heat resistance are used for transmission cases and oil pans, etc. In addition, Japanese automotive companies have already used Mg alloys in more than ten types of parts. Other applications include, but not limited to, engine head covers, air bag plates, electronic control part cases, seat frames and transmission cases, etc. In particular, steering parts made from Mg alloys are used in many car models because these materials have a good vibration damping effect [33, 34].

## 3.2 Magnesium application in aerospace industries

Magnesium alloy used in aerospace industries also base on its attractive advantage of weight reduction. As the lightest structural material, Magnesium alloys have already been used for a range of aircraft component forming although this lightweight material properties have to be further increased. For instance, ZE41 is a magnesium alloy specified for application which can be operated up to $150^0$C due to its excellent castability and good mechanical properties. WE43 is another magnesium alloy with improved corrosion performance and strength, which is widely used in the new helicopter programmes such as MD500, Eurocopter EC120, NH90 and sikorsky S92, etc. the aircraft can support longer lifecycle and meet the longer intervals of overhauls requirement. In addition, WE43 has additional advantage of superior mechanical properties compared to ZE41 which is related to fuel economy [34].

Meanwhile, magnesium alloy are being used successfully in both civil and military aircraft engine. There are many application examples in this aspect. For example, Tay engines are produced with ZE41 and RB21 gearbox is made with EZ33 by Rolls-Royce company. Some military aircraft, such as the F16, Tornado and Eurofighter Typhoon, also produce transmission casting component with magnesium alloy based on its lightweight characteristics. In addition, the new american F22 aircraft gearbox have specified with the new Pratt and

Whitney F119 gearbox which produced by WE43 magnesium alloy because of the excellent high strength properties [34].

## 3.3 Magnesium application in ICT industries

ICT (Information and communications technology) equipment has been developing with an alarming rate since 1990s. It is providing a rapidly expanding market for magnesium alloys through improved technologies, such as diecasting, thixomoulding and press forging, etc [34].

In recent years, digitalization and the need for increased portability are the main characteristics for ICT appliances, such as digital camera, projects, portable PC, compact and mini disc cases, cellular phones and television cabinets, etc. The primary requirements of these appliances are portable and compact. Magnesium alloy exactly provide potential for ICT equipment rapid expansion. Meanwhile, the properties of magnesium are ideally suited to the production of smaller and lighter components and this has led to extensive usage of the magnesium alloy [34, 40].

Magnesium alloys almost offer advantages in all aspects for ICT devices. Comparing with the reinforced plastic or composites, magnesium alloy has higher specific gravity, but its strength to weight ratio and rigidity are significantly higher, which makes it possible to manufacture slimmer and lighter components. In addition, the heat conductivity of magnesium is several hundred times greater than plastic, which led the excellent heat dissipation characteristics. The electromagnetic shielding and recycling characteristics of magnesium are also well suited to this type of application [41].

Today, magnesium alloy has already used extensively by leading ICT production manufacturers, such as Sony, Toshiba, Panasonic, Sharp, Canon, JVC, Hitachi, Nikon, NEC, Ericsson, IBM and HP, etc. Due to its unique physical and mechanical properties, the material is also being considered for a broader range of household appliance now. For instance, Matsushita electric company has successfully produced an all metallic 21 inch television cabinet by magnesium using thixomoulding technology for the first time in 1998. In 1999, Sony successfully launched two models for the Sony mini-disc walkman using magnesium alloy, i.e., the MZ-R90 and the MZ-E90. Both models were manufactured by press forging process with the wrought magnesium alloy AZ31. These components display an excellent surface quality with wall thickness reduced to 0.4mm-0.7mm [42]. In sum, magnesium alloy exhibit brilliant prospects and market for ICT equipment, its applications will be more and more widespread in the future.

## 3.4 Magnesium application in defence industries

In modern defence industry, a wide range of military appliances are produced by magnesium alloy, such as castings, powders and wrought magnesium alloy products. Structural castings magnesium alloy have been used in equipment because its low density offers a significant advantage [34, 43]. Meanwhile, component casting size varies considerably in the practical application. For instance, the military armored vehicles use large size sand casting product in interior component and electronic equipment, but the relatively medium size and complicated sand casting products are extensively used in military equipments, such as radar equipment, portable ground equipment and sting ray torpedoes etc [34]. The newest casting alloy which combines high strength and excellent corrosion resistance are also studied and used in military products, e.g., ZE41 magnesium alloy. Magnesium alloy are also widely used in anti-tank weapon with long time history. For instance, APDS tank ammunition sabot is produced by magnesium alloy, which facilitate the firing of a narrow projectile from a standard 120mm or 100mm gun barrel [41]. AZ80, AZ61 and AZM are the preferred magnesium alloys for this application because of light weight properties [34].

In addition, the magnesium alloy powders are also widely used by the military industry in a range of flare and ordnance applications, such as decoy flares and illumination flares, etc. Decoy flares are designed to defeat a missile's infrared tracking capability. It is commonly composed of a pyrotechnic composition based on magnesium or another hot-burning metal. Ground illumination flares are designed to descend by parachute and illuminate ground terrain and targets. This flares are produced through the combustion of a pyrotechnic composition, mainly including magnesium, charcoal, sulfur, sawdust etc [34].

# 4. Objectives of this thesis

In order to meet the industrial requirements, the overall objective of the proposed study is to increase the formability limits of AZ31-O magnesium alloy through advanced forming process and controlling. Thus the major specific objectives of this study are as follows:

1) *Determine the thermal mechanical properties of AZ31-O with temperature and strain rate influence*: The plasticity of AZ31 is sensitive with temperature and strain rate. And the anisotropy property is also very important for the sheet metal forming. The material thermal plasticity will be studied by experiment and simulation, and the

analyses include the stress and strain relationship, the elongation and strength, the necking and softening phenomenon. The details are presented in chapter 3.

2) *Identify the constitutive equation to describe the stress and strain relationship in various temperatures and strain rate:* The constitutive equations are used to describe the stress and strain relationship in sheet metal forming, and the chosen parameters should describe the material deformation properties. Identification constitutive equations include the mathematical model description and fitting process. The details are described in chapter 3.
3) *Investigate the thermal formability of AZ31-O with temperature and strain rate:* The material formability is the key point for sheet metal forming process. For the AZ31-O magnesium alloy, the formability is limited in lower temperature, the warm formability is very important in industry. The thermal formability study includes the warm forming limit diagram and forming influences. The warm deep drawing experiment and the according simulation should be performed in the study. The details are discussed in chapter 4.
4) *Develop finite element models of the deep drawing process by applying the appropriate parameters and compare predictions with experimental data:* The FORGE and ABAQUS simulation software is widely used in the finite element analysis field. The purpose of deep drawing simulation is to improve the thermal formability of material by means of comparison with experiment. The details are discussed in chapter 5.

# 5. References


[1] S. Kaya. Improving the formability limits lightweight metal alloy Sheet using advanced processes - finite element modeling and experiment validation, PhD dissertation, The Ohio State University, 2008.

[2] M. Kleiner, M. Geiger, A. Klaus. Manufacturing of Lightweight Components by Metal Forming. CIRP Annals - Manufacturing Technology, Volume 52, Issue 2 (2003), pp.521-542.

[3] Z. Yang, J. P. Li, J.X. Zhang, G.W. Lorimer and J. Robson. Review on research and development of magnesium alloys. Acta Metallurgy Sinica (English Letters), Vol.21 No.5 (2008), pp.313-328.

[4] R. Neugebauer, T. Altan, M. Geiger, M. Kleiner, A. Sterzing. Sheet metal forming at elevated temperatures. CIRP Annals - Manufacturing Technology, Volume 55, Issue 2 (2006), pp.793-816.

[5] R. Gehrmann, M. M. Frommert, G. Gottstein. Texture effects on plastic deformation of magnesium. Materials Science and Engineering A, 395 (2005), pp.338-349.

[6] E. Doege, W. Sebastian, K. Droder, G. Kurz, Increased Formability of Mg-Sheets using Temperature Controlled Deep Drawing Tools, in Innovations in Processing and Manufacturing of Sheet Materials, TMS Annual Meeting (2001), pp.53-60.

[7] D. L. Yin, K. F. Zhang, G. F. Wang, W. B. Han. Warm deformation behavior of hot-rolled AZ31 Mg alloy. Materials Science and Engineering A, 392 (2005), pp.320-325.

[8] A. Turreta, A. Ghiotti, S. Bruschi. Testing material formability in hot stamping operations. Proceeding of the IDDRG conference. Deep drawing research group, porto, (2006), pp.99-105.

[9] G. Pelosi. The finite-element method, Part I: R. L. Courant: Historical Corner. 2007.

[10] H. Takuda, T. Yoshii, N. Hatta. Finite-element analysis of the formability of a magnesium-based alloy AZ31 sheet. Journal of Materials Processing Technology, 89-90 (1999), pp.135-140.

[11] H. Palaniswamy, G. Ngaile, T. Altan. Finite element simulation of magnesium alloy sheet forming at elevated temperatures. Journal of Materials Processing Technology, 146 (2004), pp.52-60.

[12] P. J. Bolt, R. J. Werkhoven, A. H. van de Boogaard. Effect of elevated temperature on the drawability of aluminum sheet components, in: Proceedings of the ESAFORM, 2001, pp. 769-772.

[13] R. W. Chan, C. X. Shi, J. Ke. Structure and Properties of Nonferrous Alloys, Science Press, Beijing, 1999.

[14] Web: www.aist.go.jp. A new rolled magnesium alloy with excellent formability at room temperature. Translation of AIST press release of September 16, 2008.

[15] M. R. Barnett. Twinning and the ductility of magnesium alloys. Materials Science and Engineering A, 464 (2007), pp.1-7.

[16] T. Al-Samman, G. Gottstein. Dynamic recrystallization during high temperature deformation of magnesium. Materials Science and Engineering A, 490 (2008), pp.411-420.

[17] K. Kaiser, D. Letzig, J. Bohlen, A. Styczynski, C. Hartig, K. U. Kainer. Anisotropic Properties of Magnesium Sheet AZ31. Material Science Forum, Vols. 419-422 (2003), pp.315-320.

[18] X. Y. Lou, M. Li, R. K. Boger, S. R. Agnew, R. H. Wagoner. Hardening evolution of AZ31B Mg sheet. International Journal of Plasticity, 23 (2007), pp.44-86.

[19] S. R. Agnew, O. Duygulu. Plastic anisotropy and the role of non-basal slip in magnesium alloy AZ31B. International Journal of Plasticity, 21 (2005), pp.1161-1193.

[20] A. Jager, P. Lukac, V. Gartnerova, J. Bohlen, K. U. Kainer. Tensile properties of hot rolled AZ31 Mg alloy sheets at elevated temperatures. Journal of Alloys and Compounds, 378 (2004), pp.184-187.

[21] E. Doege, K. Droder. Sheet metal forming of magnesium wrought alloys - formability and process technology. Journal of Materials Processing Technology, 115 (2001), pp. 14-19.

[22] T. Naka, T. Uemori, R. Hino, M. Kohzu, K. Higashi, F. Yoshida. Effects of strain rate, temperature and sheet thickness on yield locus of AZ31 magnesium alloy sheet. Journal of Materials Processing Technology, 201 (2008), pp.395-400.

[23] Y. Q. Cheng, H. Zhang, Z. H. Chen, K. F. Xian. Flow stress equation of AZ31 magnesium alloy sheet during warm tensile deformation, Journal of Materials Processing Technology, 208 (2008), pp.29-34.

[24] H. Takuda, H. Fujimoto, N. Hatta. Modelling on flow stress of Mg-Al-Zn alloys at elevated temperatures. Journal of Materials Processing Technology, 80-81 (1998), pp.513-516.

[25] H. Takuda, T. Morishita, T. Kinoshita, N. Shirakawa. Modelling of formula for flow stress of magnesium alloy AZ31 sheet at elevated temperatures. Journal of Materials Processing Technology, 164–165 (2005), pp.1258-1262.

[26] Z. Q. Sheng, R. Shivpuri. Modeling flow stress of magnesium alloys at elevated temperature. Materials Science and Engineering A, 419 (2006), pp.202-208.

[27] K. F. Zhang, D. L. Yin, D. Z. Wu. Formability of AZ31 magnesium alloy sheets at warm working conditions. International Journal of Machine Tools & Manufacture, 46 (2006), pp.1276-1280.

[28] F. K. Chen, T. B. Huang. Formability of stamping magnesium-alloy AZ31 sheets. Journal of Materials Processing Technology, 142 (2003), pp.643-647.

[29] Y. S. Lee, Y. N. Kwon, S. H. Kang, S. W. Kim, J. H. Lee. Forming limit of AZ31 alloy sheet and strain rate on warm sheet metal forming. Journal of Materials Processing Technology, 201 (2008), pp.431-435.

[30] L. Wang, L. C. Chan, T. C. Lee. Formability analysis of Magnesium alloy sheets at elevated temperatures with experimental and numerical method. Journal of Manufacturing Science and Engineering, Vol. 130 (2008), pp.1-7.

[31] L. M. Ren, S. H. Zhang, G. Palumbo, D. Sorgente, L. Tricarico. Numerical simulation on warm deep drawing of magnesium alloy AZ31 sheets. Materials Science and Engineering A, 499 (2009), pp.40-44.

[32] T. B. Huang, Y. A. Tsai, F. K. Chen. Finite element analysis and formability of non-isothermal deep drawing of AZ31B sheets. Journal of Materials Processing Technology, 177 (2006), pp.142-145.

[33] H. Watarai. Trend of research and development for magnesium alloys. Journal of Science & Technology Trends, 18 (2006), pp.84-97.

[34] Web: www.magnesium-elektron.com. Magnesium Application, 2011.

[35] B. L. Mordike, F. von Buch. Development of high temperature creep resistant alloys. In, Kainer, K. U. (Ed.), Magnesium Alloys and their Applications, Wiley-VCH, D, 2000, pp.35-40.

[36] C. Jaschik, H. Haferkamp, M. Niemeyer. New magnesium wrought alloys. In: Magnesium Alloys and their Applications, Wiley-VCH, D, 2000, pp.41-46.

[37] B. Closset. Mechanical properties of extruded magnesium alloys. In: Magnesium Alloys and their Applications, Wiley-VCH, D, 2000, pp.274-279.

[38] K. J. Schemme. Magnesium motorcycle wheels for racing applications. In: Magnesium Alloys and their Applications, Wiley-VCH, D, 2000, pp.391-396.

[39] H. W. Wagener, F. Lehnert. Deep drawing of magnesium sheet metal at room temperature. In: Magnesium Alloys and their Applications, Wiley-VCH, D, 2000, pp.615-620.

[40] H. Furuya, S. Matunaga, N. Kogizo. Requirements and feasibility of magnesium alloys for aerospace applications. Materials Science Forum, Vols. 419-422 (2003), pp.261-266.

[41] S. R. Agnew. Wrought Magnesium: A 21st Century Outlook. JOM. 2004.

[42] F. Tsuneya. Magnesium alloy die casting technology for designing and manufacturing engineers. Nikkan Kogyo schimbun, Ltd.

[43] J. A. Horton, C. A. Blue, S. R. Agnew, Magnesium Technology 2003, Ed. H.I. Kaplan (Warrendale, PA: TMS, 2003), pp.243-246.

# Chapter 2 Material model for warm forming

## Contents

# 1. Introduction

An important objective of studying the material deformation process is to produce non-defect parts in industry. This goal can be achieved by better design and control of parameters in the deformation processes. This should be based on a deeper knowledge of the deformation phenomenon of material and the relationships between material properties and the conditions of deformation [1]. The material model plays an important role in describing metal forming process in the numerical calculations. The accuracy of such a material model depends on both the model mathematical structure and the proper experimental determination of the material parameters used in the model [2]. The model's mathematical structure should take into account the physical phenomenon that occur in the deformation process, which depend on the type of material, the conditions of forming, the history of deformation and phenomenon essential for the numerical simulation, etc.

In plasticity mechanics, the hardening and constitutive relationship have widely studied for many years [3]. The equations that describe relationship of flow stress and strain are usually divided into two types [4]. The first type comprises models that describe directly the changes in the flow stress of materials depending on the deformation conditions such as temperature and rate of deformation. These models usually do not take into account deformation history. It is described correctly the flow stress in the cases when strain hardening is the dominant factor that determines the state of the materials. However, when the processes of thermally activated softening become consequential, the models lead to erroneous results. The second type includes models where the deformation history affects the internal state of material, determined primarily by its structure, and the actual response of the material to the deformation conditions depends on its internal state. In such a case, the behavior of material is analyzed through a combination of two separate aspects, the evolution of internal state of the deformed material and the response of the material with a particular internal state to a change in the deformation conditions [5].

The theoretical prediction model for material forming limits is also a study focus in sheet forming field [6]. Various prediction models have been introduced in the literature in the last fifty years. The theoretical prediction model proposed a way to study material forming limits, and it is useful to understand deeply the material formability and deformation property. It is a common method through comparing the experimental forming limit strains and theoretical predicted forming limit strain. In the finite element simulation, it is also used to enhance the

simulation model closer to the real situation of production, especially for complex forming limit prediction and springback [7].

## 2. Yield function for sheet forming

In metal sheet forming process, yield condition is a hypothesis based on the elastic limit state of metal. Transition from the elastic deformation to plastic deformation depends on the following two factors [8]. The first factor is the physical and mechanical properties of material under certain deformation conditions, e.g., deformation temperature and deformation rate. The second factor is the stress state of material deformation. When the combination of stress components satisfy a function, and the external stress state conditions match exactly the internal material yield factors, the material will changes from elastic deformation to plastic deformation.

Generally, yield condition includes stress, strain, time and temperature, etc. It can be simply written as follow [9]:

$$\phi(\sigma_{ij}, \varepsilon_{ij}, t, T) = 0 \tag{2.1}$$

Where, $\sigma_{ij}$ and $\varepsilon_{ij}$ are the components of stress and strain tensor respectively, $t$ is time and $T$ is temperature. If without considering the time and temperature effects, and the material keeps elastic state prior to the initial yield, the stress and strain relations will be corresponding simple. The yield condition can be simplified as follow:

$$F(\sigma_{ij}) = 0 \tag{2.2}$$

In the stress space, the above equation expresses a yield surface which contains the origin point. When the stress point is inside of surface, the material will be in the elastic state. When the stress point is on the surface, the material will starts to yield. This is the simple description of yield criterion [7].

Furthermore, if material is initially isotropic, the yield condition can be expressed by variables which are independent of the direction. The three principal stresses can determine a unique stress state, and then yield condition can be expressed as follow:

$$f(\sigma_1, \sigma_2, \sigma_3) = 0 \tag{2.3}$$

Accordingly, the equation also can be expressed using invariant components of stress tensor as follow:

$$f(I_1, I_2, I_3) = 0 \tag{2.4}$$

Where, $I_1$, $I_2$ and $I_3$ are the first, second and third invariant components of the stress tensor respectively. According to plastic deformation and the hydrostatic stress independent assumption, the above equation accord only with invariant components of deviatoric stress tensor. That is as follow:

$$f(J_1, J_2, J_3) = 0 \tag{2.5}$$

Where, $J_1$, $J_2$ and $J_3$ are the first, second and third invariant components of deviatoric stress tensor respectively. For the ideal plastic deformation material, without considering the Bauschinger effect, yield equation must be an even function for $I_3$, while equation (2.5) must be an even function for $J_3$ [4, 7, 8]. Nowadays, The yield criteria are used mostly without $I_3$ or $J_3$.

## 2.1 Tresca and von Mises isotropy yield criteria

The first yield criterion used to describe the metal material combination stress state was proposed by Henri Tresca in 1864 [11]. And it was further developed in the following years and proposed the mathematical expressions of criterion. This criterion describe that the material start plastic deformation when maximum shear stress reaches the material yield shear limit, the application of shear stress is expressed in mathematical formula as follows:

$$\begin{cases} \tau_{12} = \pm\dfrac{\sigma_s}{2} \\ \tau_{23} = \pm\dfrac{\sigma_s}{2} \\ \tau_{31} = \pm\dfrac{\sigma_s}{2} \end{cases} \tag{2.6}$$

Where, $\sigma_s$ is the yield stress. The equation is expressed by the principal stress as follow:

$$\max(|\sigma_1 - \sigma_2|, |\sigma_2 - \sigma_3|, |\sigma_3 - \sigma_1|) = \sigma_s \tag{2.7}$$

The von Mises yield criterion is generally attributed to Richard Edler von Mises (1913) [12], Maxwell (1865), Hencky and Tytus Maksymilian Huber (1904) also had some contributions for this criterion. So it is also referred to as the Maxwell-Huber-Hencky-von Mises theory [13]. The key point of this criterion is that the yielding begins when the second invariant component of deviatoric stress tensor $J_2$ reaches a critical value $k^2$. For this reason, the von Mises criterion is also called the *$J_2$-plasticity* or *$J_2$ flow theory*. The yield function can be expressed as follow:

$$F(\sigma_{ij}) = J_2 - k^2 \tag{2.8}$$

Where, $k$ can be shown as the yield stress in pure shear state. The function also can be expressed by the principle stress tensor components as follows:

$$(\sigma_1 - \sigma_2)^2 + (\sigma_2 - \sigma_3)^2 + (\sigma_3 - \sigma_1)^2 = 2\sigma_s^2 \tag{2.9}$$

Fig.1 shows the comparison of Tresca and von-Mises criteria in 2D and 3D space. The von-Mises equation defines the yield surface as a circular cylinder, while Tresca equation defines the yield surface as a hexagonal prism in 3D space. From the figure, it is observed that Tresca's yield surface (dashed line) is circumscribed by von-Mises yield surface. As a model for plastic material behavior, Tresca criterion is therefore more conservative [14].

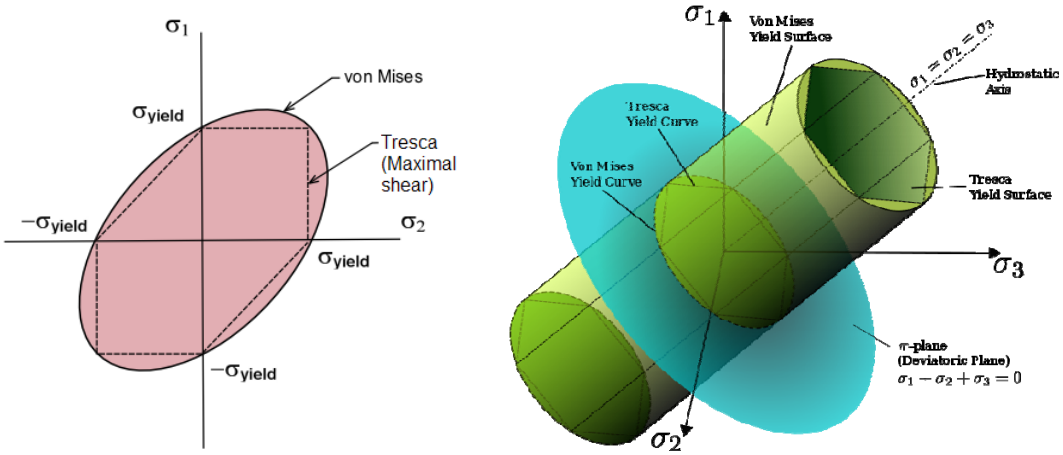


Fig.1. Comparison of Tresca and von-Mises criteria in 2D space and 3D space [14].

Generally, the von Mises stress is widely used to predict yielding of materials under any loading condition from results of simple uniaxial tensile tests. The von Mises stress satisfies the following characteristics, if materials have equal distortion energy in two stress states, they have equal von Mises stress. Because the von Mises yield criterion is independent of the first invariant component of stress tensor $J_1$, it is available for the analysis of plastic deformation when the onset of yield for these materials does not depend on the hydrostatic component of stress tensor.

Tresca and von-Mises yield criterion are only useful for isotropic materials in theory. However, for many engineering materials and calculations, the use of the accuracy of the two yield criteria have been enough, while others yield criterion is much more complex mathematically. So, these two yield criteria are still in use up to now, even it is used to study some anisotropy problems. In the commercial simulation software, such as ABAQUS, ANSYS, LS-Dyna, etc., these criteria are included in the isotropy material models.

## 2.2 Anisotropy yield criterion

### 2.2.1 Hill's anisotropy yield criterion

**1) General description**

In 1948, R. Hill introduced the sheet anisotropy property into yield equation for the first time [15]. He proposed yield criterion for orthotropic materials following the von Mises yield criterion and induce a reasonable mathematical description for sheet anisotropic plastic flow. the expression of this criterion is following:

$$\begin{aligned} 2f(\sigma_{ij}) = F(\sigma_{yy}-\sigma_{zz})^2 + G(\sigma_{zz}-\sigma_{xx})^2 + H(\sigma_{xx}-\sigma_{yy})^2 \\ + 2L\sigma_{yz}^2 + 2M\sigma_{zx}^2 + 2N\sigma_{xy}^2 \end{aligned} \tag{2.10}$$

In the equation, *x, y, z* are the orthotropic coordinates, *F, G, H, L, M, N* are the anisotropy parameters depending on the materials, and can be determined by experiment. If setting *X, Y, Z* as uniaxial tensile yield stress corresponding to the three anisotropy principal axis direction, *R, S, T* as shear yield stress corresponding to the three anisotropy principal axis direction, there are following relationships.

$$G+H=\frac{1}{X^2},\ \ H+F=\frac{1}{Y^2},\ \ F+G=\frac{1}{Z^2},\ \ L=\frac{1}{2R^2},\ \ M=\frac{1}{2S^2},\ \ N=\frac{1}{2T^2} \tag{2.11}$$

When $3F=3G=3H=L=M=N$, the above equation becomes the von Mises yield equation for isotropic materials.

**2) Plane stress expression**

For the sheet metal forming, the stress is often under plane stress state, i.e., $\sigma_{zz}$, $\sigma_{zx}$, $\sigma_{yz}$ equal zero, and the *x, y, z* is the orthotropic principal axis, the equation (2.10) can be described by principle axis as follow:

$$f=(G+H)\sigma_x^2 - 2H\sigma_x\sigma_y + (H+F)\sigma_y^2 + 2N\sigma_{xy}^2 = 1 \tag{2.12}$$

**3) Principal stress expression**

If material is under principal stress state, the stress principal axis are consistent with the anisotropy principal axis, and $\sigma_{xy}$ equal zero, the yield equation can be simplified by principle stress as follow:

$$2f(\sigma_{ij}) = F(\sigma_2-\sigma_3)^2 + G(\sigma_3-\sigma_1)^2 + H(\sigma_1-\sigma_2)^2 = 1 \tag{2.13}$$

The corresponding plane stress state expression is following.

$$2f = (G+H)\sigma_1^2 - 2H\sigma_1\sigma_2 + (H+F)\sigma_2^2 = 1 \tag{2.14}$$

**4) Thickness anisotropy expression**

In 1962, Backofen *et al.* made a simplification for equation (2.14) [16]. And assuming the material anisotropy is just described in thickness direction without in-plane area. If the in-plane yield stress $\sigma_{s_1} = \sigma_{s_2} = \sigma_s$ and $\sigma_{s_3} = \sigma_t$, then it is easy to induce the following relationship, $G+H = F+H = \frac{1}{\sigma_s^2}$, $F+G = \frac{1}{\sigma_t^2}$, $F$=$G$, the equation (2.14) can be expressed as follow:

$$\sigma_1^2 - \frac{2H}{G+H}\sigma_1\sigma_2 + \sigma_2^2 = \sigma_s^2 \tag{2.15}$$

The Lankford coefficient which is the ratio of the lateral ($\varepsilon_w$) and thickness plastic strain ($\varepsilon_t$) is induced into equation as follows.

$$r = \frac{H}{G} = \frac{\varepsilon_w}{\varepsilon_t} = 2\left(\frac{\sigma_t}{\sigma_s}\right)^2 - 1 \tag{2.16}$$

The yield equation can be described by Lankford coefficient as follows:

$$\sigma_1^2 - \frac{2r}{1+r}\sigma_1\sigma_2 + \sigma_2^2 = \sigma_s^2 \tag{2.17}$$

The Lankford coefficient demonstrates the material resisting thinning capability. The higher $r$ value leads the greater $\frac{\sigma_t}{\sigma_s}$ value, the resisting thinning ability of material is stronger. Meanwhile, the stress and strain intensity can be expressed as follows:

$$\sigma_i = \sqrt{\sigma_1^2 - \frac{2r}{1+r}\sigma_1\sigma_2 + \sigma_2^2} \tag{2.18}$$

$$\varepsilon_i = \frac{1+r}{\sqrt{1+2r}}\sqrt{\varepsilon_1^2 + \frac{2r}{1+r}\varepsilon_1\varepsilon_2 + \varepsilon_2^2} \tag{2.19}$$

### 2.2.2 Hosforld's anisotropy yield criterion

In 1972, Hosford proposed a yield criterion used to determine material yielding condition [17]. The form of Hosford's criterion is simple, the expression is following:

$$f = |\sigma_1 - \sigma_2|^n + |\sigma_2 - \sigma_3|^n + |\sigma_3 - \sigma_1|^n = 2\sigma_s^n \tag{2.20}$$

Where, $\sigma_i$ (for $i$ from 1 to 3) are the principal stresses, $n$ is a material dependent exponent and $\sigma_s$ is the yield stress in uniaxial tension. The above equation just used for isotropic material. The equation just includes one parameter $n$ which can be identified from experiment. Barlat [18] found that this criterion is better than von-Mises and Tresca criterion in the forming limit diagram prediction of aluminum alloy. In addition, in order to solve material anisotropy problem, Logan and Hosford revised the equation and introduce the Lankford coefficient for anisotropy material in plane stress state. The expression is following:

$$|\sigma_1|^n + |\sigma_2|^n + r|\sigma_1 - \sigma_2|^n = (1+r)\sigma_s^n \tag{2.21}$$

Where, $r$ is the Lankford coefficient. The yield locus from Hosford's criterion is defined by curve fitting based on polycrystalline plasticity model. In addition, the parameter $n$ is different for various material. e.g., For the BCC (Body-Centered Cubic) material, $n = 6$. For the FCC (Face-Centered Cubic) material, $n = 8$. Fig.2 shows the yield locus defined by Hosford's criterion for three various value of $n$ under plane stress state. When $n = 1$ or $n$ goes to infinity the Hosford criterion reduces to the Tresca yield criterion. When $n = 2$ the Hosford criterion reduces to the von Mises yield criterion. Graf and Hosford [19] have proved that the result calculated by this criterion match well with the experimental result, and the result is better using Lankford coefficient $r$ for forming limit theoretical prediction.

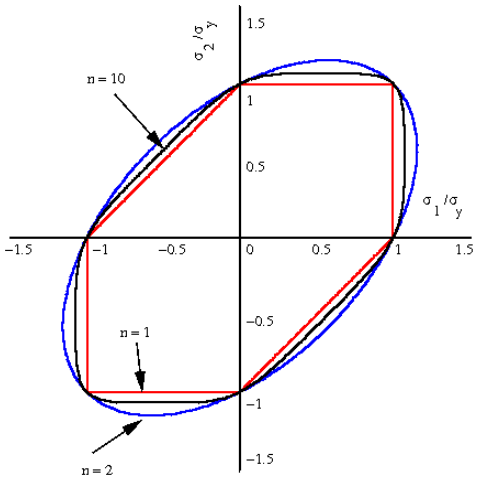


Fig.2. Hosford yield locus for three various values of n under plane stress state [19]

### 2.2.3 Barlat-Lian anisotropy yield criterion

#### 1) Barlat'89 yield criterion [20]

Since the Hosford yield criterion does not include the shear stress components, it can not solve the problem when the anisotropy axis does not coincide with the stress axis. Therefore, Barlat [20] proposed a new yield criterion to deal with in-plane anisotropy in plane stress state

in 1989. It is called Barlat'89 yield criterion in short. This criterion can accurately describe material yield locus by Bishop and Hill material model [7]. The expression is following:

$$f = a\left|K_1 + K_2\right|^m + a\left|K_1 - K_2\right|^m + (2-a)\left|2K_2\right|^m = 2\sigma_s^m \tag{2.22}$$

Where, the parameter $K_1$ and $K_2$ is defined as follows:

$$K_1 = \frac{\sigma_{xx} + h\sigma_{xy}}{2} \qquad K_2 = \sqrt{\left(\frac{\sigma_{xx} - h\sigma_{xy}}{2}\right)^2 + p^2\sigma_{xy}^2} \tag{2.23}$$

Where, the parameter $m$ is non-quadratic yield function exponent and can be identified by experiment, $x$, $y$ and $z$ are respectively the orthogonal coordinate with respect to the rolling direction, perpendicular to the rolling direction, perpendicular to the plane direction. $a, h, p$ are the parameters to characterize the material anisotropy, and there are two method to calculate these parameters. One of methods is based on stress calculation. For instance, introducing parameter $\sigma_{90}$ into expression, which are the stress applied $90^0$ angle with respect to rolling direction. $\tau_{s_1}$ and $\tau_{s_2}$ are the first and second principle shear stress. When the shear stress $\tau_{s_2} = \sigma_{yy} = -\sigma_{xx}$, $\sigma_{yy} = 0$, $\sigma_{xx} = \sigma_{yy} = 0$, $\sigma_{xy} = \tau_{s_1}$, the parameters can be identified as following expression.

$$a = \frac{2\left(\frac{\bar{\sigma}}{\tau_{s2}}\right)^m - 2\left(1 + \frac{\bar{\sigma}}{\sigma_{90}}\right)^m}{1 + \left(\frac{\bar{\sigma}}{\sigma_{90}}\right)^m - \left(1 - \frac{\bar{\sigma}}{\sigma_{90}}\right)^m} \tag{2.24}$$

$$h = \frac{\bar{\sigma}}{\sigma_{90}} \tag{2.25}$$

$$p = \frac{\bar{\sigma}}{\tau_{s1}}\left(\frac{2}{2a + 2^m(2-a)}\right)^{1/m} \tag{2.26}$$

Where, the $\bar{\sigma}$ is equivalent stress. And the parameter expression is related complicated. The second calculation method is based on the thickness anisotropy Lankford coefficient. Introducing three parameters $r_0$, $r_{45}$ and $r_{90}$ into equation, which are respectively Lankford coefficient applied $0^0$, $45^0$ and $90^0$ angle with respect to rolling direction.. The expression is following:

$$a = 2 - 2\sqrt{\frac{r_0}{1+r_0} \cdot \frac{r_{90}}{1+r_{90}}} \tag{2.27}$$

$$h = \sqrt{\frac{r_0}{1+r_0} \cdot \frac{1+r_{90}}{r_{90}}} \tag{2.28}$$

The parameter $p$ can not be calculated directly. But when the parameters $a$ and $h$ are defined, the relationship of parameter $p$ and Lankford coefficient is linear. So, the parameter $p$ can be calculated by iteration method as follow:

$$\frac{2m\sigma_s^m}{\left(\frac{\partial f}{\partial \sigma_{xx}} + \frac{\partial f}{\partial \sigma_{yy}}\right)\sigma_{45}} - 1 - r_{45} = g(p) \tag{2.29}$$

Where, $\sigma_{45}$ is the yield strength applied $45^0$ angle with respect to rolling direction. The independent parameter $m$ is different for various material and can be identified by experiment. For FCC material, $m = 8$. For BCC material, $m = 6$. When $m = 2$, the criterion reduces to the von Mises yield criterion.

Barlat'89 yield criterion include the shear stress component, it can solve the material anisotropy when the anisotropy axis does not coincide the stress axis. But, it is restricted to solve only the plane stress problems. In addition, the parameters $p$ can not be explicitly determined. Consequently, Barlat [20] also pointed out that the yield criterion can well describe the yield locus which obtained based on the Bishop and Hill material models, but it is not accurate to describe material property with large anisotropic coefficient. However, this criterion considers the plane stress state of all cases and the anisotropy property at the same time.

**2) Barlat'91 yield criterion [21]**

Due to the limitation of Barlat'89 yield criterion which just can solve the plane stress problem, Barlat proposed another yield criterion in 1991 and called Barlat'91 criterion in short [21]. The new criterion is more universal and can solve the three dimension stress problem. The new criterion expressed as follows:

$$\Phi = (3I_2)^{m/2}\left\{\left[2\cos\left(\frac{2\theta+\pi}{6}\right)\right]^m + \left[-2\cos\left(\frac{2\theta-3\pi}{6}\right)\right]^m + \left[2\cos\left(\frac{2\theta+5\pi}{6}\right)\right]^m\right\} = 2\sigma_s^m \tag{2.30}$$

Where, the parameters are following.

$$I_2 = \frac{(fF)^2 + (gG)^2 + (hH)^2}{3} + \frac{(aA-cC)^2 + (cC-bB)^2 + (bB-aA)^2}{54} \tag{2.31}$$

$$I_3 = \frac{(cC - bB)(aA - cC)(bB - aA)}{54} + fghFGH - \frac{(cC - bB)(fF)^2 + (aA - cC)(gG)^2 + (bB - aA)(hH)^2}{6} \tag{2.32}$$

$$\theta = \arccos\left(\frac{I_3}{I_2^{2/3}}\right) \tag{2.33}$$

$$A = \sigma_{yy} - \sigma_{zz} \qquad B = \sigma_{zz} - \sigma_{xx} \qquad C = \sigma_{xx} - \sigma_{yy} \tag{2.34}$$

$$F = \sigma_{yz} \qquad G = \sigma_{zx} \qquad H = \sigma_{xy} \tag{2.35}$$

In above equation, the parameter *m* is non-quadratic yield function exponent, generally more than 1. $\theta$ is the angle with respect to rolling direction. The parameters *a, b, c, f, g, h* can be determined by the three direction uniaxial tensile test and shear tests. When the six parameters equal 1, the criterion becomes isotropic. Barlat [21] has used this criterion to predict yield stress of 2024-T3 aluminium alloy by uniaxial tensile test has applied various angle with rolling direction, finally, the calculated result match well with the experiment.

Barlat [21] point out that the criteria can more accurately predict the uniaxial tensile yield stress on different directions. But in the prediction of Lankford coefficient (*r* value), the discrepancy with the experimental results is greater, and the accuracy even lower than the Hill'48 yield criterion. He believes that it should be considered reducing such restrictions for strengthen hypothesis to improve the prediction accuracy.

**3) Barlat'2000 yield criterion [22-24]**

In 1994 and 1996, Barlat proposed two other criterions considering the problem in the former criterions [22, 23]. The Barlat'94 criterion (YLD94) increased several parameters, but it still can not predict accurately Lankford coefficients (*r* value). The Barlat'96 criterion (YLD96) increased the Lankford coefficient of $45^0$ angles with respect to rolling direction, and improved the thickness anisotropy prediction in this criterion. But there is still not the convexity certification, and convexity is necessary condition for the solution in numerical simulation. The parameters of YLD 96 are very difficult to be identified precisely. So it is not very convenient in simulation application. Especially for some three dimensional numerical problems, the criterion is difficult to solve due to the complexity.

Based on the above problem, Barlat *et al.* proposed a new criterion, called YLD2000-2D in 2000 [24]. This criterion is specifically for the plane stress state, the expression is following.

$$\phi = \phi' + \phi'' = 2\sigma_s^a \tag{2.36}$$

$$\phi' = | X_1' - X_2' |^a \tag{2.37}$$

$$\phi'' = | 2X_2'' + X_1'' |^a + | 2X_1'' + X_2'' |^a \tag{2.38}$$

$$X' = L'\sigma \qquad\qquad X'' = L''\sigma \tag{2.39}$$

$$\begin{bmatrix} L_{11}' \\ L_{12}' \\ L_{21}' \\ L_{22}' \\ L_{66}' \end{bmatrix} = \begin{bmatrix} 2/3 & 0 & 0 \\ -1/3 & 0 & 0 \\ 0 & -1/3 & 0 \\ 0 & 2/3 & 0 \\ 0 & 0 & 1 \end{bmatrix} \begin{bmatrix} \alpha_1 \\ \alpha_2 \\ \alpha_7 \end{bmatrix} \tag{2.40}$$

$$\begin{bmatrix} L_{11}'' \\ L_{12}'' \\ L_{21}'' \\ L_{22}'' \\ L_{66}'' \end{bmatrix} = \frac{1}{9} \begin{bmatrix} -2 & 2 & 8 & -2 & 0 \\ 1 & -4 & -4 & 4 & 0 \\ 4 & -4 & -4 & 1 & 0 \\ -2 & 8 & 2 & -2 & 0 \\ 0 & 0 & 0 & 0 & 9 \end{bmatrix} \begin{bmatrix} \alpha_3 \\ \alpha_4 \\ \alpha_5 \\ \alpha_6 \\ \alpha_8 \end{bmatrix} \tag{2.41}$$

Where, the parameter $a$ is determined by uniaxial tensile test and biaxial tensile test in three angle directions. $\alpha_i$ (for $i$ from 1 to 8) are the independent coefficients for linear transformation vector. Meanwhile, Barlat [24] have given the procedure for the use of experimental data to determine the parameters. The accuracy of YLD2000 is no less than YLD96, and the convexity of criterion has been proven. YLD2000-2D has a simple mathematical form comparing with YLD96, so it is relatively easy to use the criterion in finite element simulation. Since the criterion is just for plane stress problems, it can not solve three dimensional stress states, bending and solid element problem in numerical simulation of sheet metal forming.

**4) Barlat'2004 yield criterion**

In 2005, Barlat proposed two anisotropy yield criterions to solve the three dimension plane stress problem based on the linear transform of deviatoric stress tensor [25, 26]. It includes 18 (YLD2004-18P) and 13 (YLD2004-13P) parameters respectively. The expression is as follows:

YLD2004-18P:

$$\begin{aligned} \phi &= \phi(\Sigma) = \phi(\tilde{S}', \tilde{S}'') \\ &= | \tilde{S}_1' - \tilde{S}_1'' |^a + | \tilde{S}_1' - \tilde{S}_2'' |^a + | \tilde{S}_1' - \tilde{S}_3'' |^a + | \tilde{S}_2' - \tilde{S}_1'' |^a + | \tilde{S}_2' - \tilde{S}_2'' |^a \\ &\quad + | \tilde{S}_2' - \tilde{S}_3'' |^a + | \tilde{S}_3' - \tilde{S}_1'' |^a + | \tilde{S}_3' - \tilde{S}_2'' |^a + | \tilde{S}_3' - \tilde{S}_3'' |^a = 4\sigma_s^a \end{aligned} \tag{2.42}$$

$$\tilde{s}' = C'S \tag{2.43}$$

$$\tilde{s}'' = C''S \tag{2.44}$$

$$C' = \begin{bmatrix} 0 & -c'_{12} & -c'_{13} & 0 & 0 & 0 \\ -c'_{21} & 0 & -c'_{23} & 0 & 0 & 0 \\ -c'_{31} & -c'_{32} & 0 & 0 & 0 & 0 \\ 0 & 0 & 0 & c'_{44} & 0 & 0 \\ 0 & 0 & 0 & 0 & c'_{55} & 0 \\ 0 & 0 & 0 & 0 & 0 & c'_{66} \end{bmatrix} \tag{2.45}$$

$$C'' = \begin{bmatrix} 0 & -c''_{12} & -c''_{13} & 0 & 0 & 0 \\ -c''_{21} & 0 & -c''_{23} & 0 & 0 & 0 \\ -c''_{31} & -c''_{32} & 0 & 0 & 0 & 0 \\ 0 & 0 & 0 & c''_{44} & 0 & 0 \\ 0 & 0 & 0 & 0 & c''_{55} & 0 \\ 0 & 0 & 0 & 0 & 0 & c''_{66} \end{bmatrix} \tag{2.46}$$

YLD2004-13P:

$$\begin{aligned} \phi &= \phi'(\tilde{S}') + \phi''(\tilde{S}'') \\ &= |\tilde{S}'_1 - \tilde{S}''_2|^a + |\tilde{S}'_2 - \tilde{S}''_3|^a + |\tilde{S}'_3 - \tilde{S}''_1|^a - \{|\tilde{S}'_1|^a + |\tilde{S}'_2|^a + |\tilde{S}'_3|^a\} + |\tilde{S}''_1|^a \\ &+ |\tilde{S}''_2|^a + |\tilde{S}''_3|^a = 4\sigma_s^a \end{aligned} \tag{2.47}$$

$$\tilde{s}' = C'S \tag{2.48}$$

$$\tilde{s}'' = C''S \tag{2.49}$$

$$C' = \begin{bmatrix} 0 & -1 & -c'_{13} & 0 & 0 & 0 \\ -c'_{21} & 0 & -c'_{23} & 0 & 0 & 0 \\ -1 & -1 & 0 & 0 & 0 & 0 \\ 0 & 0 & 0 & c'_{44} & 0 & 0 \\ 0 & 0 & 0 & 0 & c'_{55} & 0 \\ 0 & 0 & 0 & 0 & 0 & c'_{66} \end{bmatrix} \tag{2.50}$$

$$C'' = \begin{bmatrix} 0 & -c''_{12} & -c''_{13} & 0 & 0 & 0 \\ -c''_{21} & 0 & -c''_{23} & 0 & 0 & 0 \\ -1 & -1 & 0 & 0 & 0 & 0 \\ 0 & 0 & 0 & c''_{44} & 0 & 0 \\ 0 & 0 & 0 & 0 & c''_{55} & 0 \\ 0 & 0 & 0 & 0 & 0 & c''_{66} \end{bmatrix} \tag{2.51}$$

These two criterions are isotropic functions of the independent variables and both are convex, including 18 and 13 parameters to describe the material anisotropy respectively. When $a = 2$ (or 4) and $c_{ij}^{'}$, $c_{ij}^{''}$ equal 1, the criterion become von Mises yield criterion. Parameters $c_{ij}^{'}$ and $c_{ij}^{''}$ can be determined by the uniaxial tensile test and biaxial tensile test in seven different angle with the rolling direction.

Barlat [25, 26] pointed out that YLD2004-18P can accurately describe the flow stress in uniaxial tensile test and Lankford coefficient, so it can predict well the earing phenomenon in the finite element simulation. For the YLD2004-13P, although the accuracy is lower than YLD2004-18P, but it can also provide a reasonable description for main trends. The application is more convenient and has enough flexibility to describe the anisotropy of material

Yoon *et al*. [26] embed YLD2004-18P into the finite element program, and found that the criteria can accurately predict the earring shape and number in deep drawing when the anisotropy parameters have been obtained accurately.

# 3. Constitutive equation

In sheet metal forming analysis, constitutive equation is a relation between stresses and strains. The establishment of constitutive relationship must follow certain principles to ensure the correctness. It mainly include following aspects [27].

(1) *Certainty principle*: the behavior of materials at time *t* determine by the objects all of movement history before the time;

(2) *Local effect principle*: the behavior of material for an object point *P* at time *t* confirm only by the movement history of the point in arbitrary small neighborhood;

(3) *Coordinate invariance principle*: constitutive relationship is independent of the coordinate system (using tensor notation or abstract notation to meet naturally);

(4) *Objectivity principle*: constitutive relationship is independent of the observer who uses different clocks and does different movements, i.e., constitutive relationship is invariant for the rigid motion of reference frame (also known as frame non-difference principle).

## 3.1 Elastic constitutive relationship

The elastic constitutive relationship is related simple. Assuming the material is isotropic and undergoes uniform deformation, the elastic constants do not change with strain and has no relationship with the stress and strain path when material is in elastic deformation state. In

mathematics, the elastic constitutive equation is a single-valued function of instantaneous strain state, it is independent of how the stress state arrival. The state is that the material has no flow and plastic deformation [28].

The first elastic constitutive equation is developed by Robert Hooke and called Hooke's law. Generalized Hooke's Law is the basis for the theory of elasticity, stress components and strain components can be expressed as follows [29].

$$\begin{cases} \varepsilon_x = \dfrac{1}{E}[\sigma_x - \nu(\sigma_y + \sigma_z)] \\ \varepsilon_y = \dfrac{1}{E}[\sigma_y - \nu(\sigma_x + \sigma_z)] \\ \varepsilon_z = \dfrac{1}{E}[\sigma_z - \nu(\sigma_x + \sigma_y)] \end{cases} \tag{2.52}$$

$$\begin{cases} \sigma_x = \lambda\varepsilon_{aa} + 2G\varepsilon_x \quad \lambda = \dfrac{\nu E}{(1+\nu)(1-2\nu)} \\ \sigma_y = \lambda\varepsilon_{aa} + 2G\varepsilon_y \quad G = \dfrac{E}{2(1+\nu)} \\ \sigma_z = \lambda\varepsilon_{aa} + 2G\varepsilon_z \quad \varepsilon_{aa} = \varepsilon_x + \varepsilon_y + \varepsilon_z \end{cases} \tag{2.53}$$

Where, the constant $\lambda$ called lame constant, $G$ is the shear modulus. $E$ and $\nu$ are Young's modulus and Poisson's ratio respectively.

## 3.2 Plastic constitutive relationship

Classical plasticity theory, also known as the abstractive mathematical theory of plasticity, the study objective is the macroscopic phenomena of material plastic deformation [30]. The origins of study the material plastic deformation behavior can be traced back to the French engineer *Tresca* in 1864 - 1872. He proposed the maximum shear stress yield criterion based on a series of metal experiments, then *Saint Venant* (1870) published the stress - strain rate equation (plastic flow equation), *Levy* (1871) proposed the stress - strain increment relations of material plastic deformation. Subsequently, *Hube*r and *Mises* (1904-1913) reported a yield criterion based on the greatest deformation energy. Around in 1945, a more rigorous and uniform classical plasticity theory was proposed from the *Drucker*, *Prager,etc.* After that, classical plasticity theories go into a comprehensive development period, and also obtain a wide range of applications in practice [31-33].

### 3.2.1 Plastic total strain theory

Elastic-plastic small deformation theory also call the deformation theory or total strain theory. It is mainly used for small elastic, plastic deformation, the stress-strain state is determined by the total amount of plastic strain components, mainly studied by Hencky, Nadai and Ilyushin (А. Илъющин), etc [34]. Total strain plasticity theory is relatively simple in the plastic mechanics physical relationship. The analysis for this theory is consistent with elastic problem. Based on the total amount of deformation, it needs the following assumptions to establish the equation by total strain theory [35].

1) *The direction of principle stress and strain must coincide, i.e. stress and strain Mohr circle are similar, the stress Lode parameter* $\mu_\sigma$ *and strain Lode parameter* $\mu_\varepsilon$ *are equal, and principle direction maintain in the whole loading process.*
2) *The equivalent stress and strain should be proportional.*
3) *The stress deviatoric component and strain deviatoric component should be proportional.*
4) *The stress intensity is a function of strain intensity. And this function for each specific material should be determined through experiments. The equation is following.*

$$\sigma_i = E' \varepsilon_i \tag{2.54}$$

Where, the parameter $E'$ is relative not only with material property, but also with the plastic deformation. The classical total strain theory are still widely used so far.

**1) Hencky theory**

In 1924, Hencky [36] proposed the complete description of total strain theory according the stress-strain relationship in elastic range [36]. He assumed that the stress deviatoric component is proportional with the plastic strain deviatoric component. The expression is following:

$$\varepsilon_{ij}^p = \frac{3\varepsilon_i^p}{2\sigma_i} S_{ij} = \frac{\phi}{2G} \tag{2.55}$$

$$\phi = \frac{3G\varepsilon_i^p}{\sigma_i} \tag{2.56}$$

In above expressions, $\varepsilon_{ij}^p$ is plastic strain component, $\varepsilon_i^p$ is equivalent plastic strain, $\sigma_i$ is equivalent plastic stress, $S_{ij}$ is the deviatoric stress component. Hencky equation considers an ideal elastic-plastic material, without the hardening phenomenon. So it just only used for

small deformation, and completely ignores the loading history in plastic stress-strain relationship. Nadai and Ilyushin studied the equation and proved that the total strain theory and increment theory are exactly same results in certain strain path and loading conditions.

**2) Nadai Theory**

Nadai theory [37] is used for the hardening material and large deformation case. it is proposed that octahedral shear stress can be used in hardening criterion when material is in plastic state, and the normal stress on octahedral has no influence for yield. The basic equation is following:

$$\varepsilon_{ij} = \frac{1}{2}\frac{\bar{\gamma}_8}{\tau_8} s_{ij} \tag{2.57}$$

Where, $\varepsilon_{ij}$ is strain component, $s_{ij}$ is deviatoric stress component, $\bar{\gamma}_8$ is octahedral shear strain and $\tau_8$ is octahedral shear stress. And the determination of hardening conditions is following:

$$\tau_8 = \varphi(\bar{\gamma}_8) \tag{2.58}$$

Nadai theory ignores the elastic strain in the total strain, and considering the case of large deformation and strengthening materials. The principal strain direction and the proportion always remain same during forming process, the loading condition is simple and the expression is following:

$$\frac{\mathrm{d}\varepsilon_1}{\varepsilon_1} = \frac{\mathrm{d}\varepsilon_2}{\varepsilon_2} = \frac{\mathrm{d}\varepsilon_3}{\varepsilon_3} \tag{2.59}$$

**3) Ilyushin Theory**

In 1945, Ilyushin studied Hencky theory, and extended the application range to the hardening materials [38]. It is based on following theoretical assumptions.

1) *Plastic strain is small and with the same order magnitude of the elastic deformation.*
2) *External loading increase proportionally for each component.*
3) *Stress-strain curves must match with the single curve hypothesis, and the equation form is exponential, that is,* $\sigma = A\varepsilon^n$.

With the above assumption, the theoretical expression of Ilyushin theory is following.

$$\varepsilon'_{ij} = \frac{3\mathrm{d}\bar{\varepsilon}}{2\bar{\sigma}} \sigma'_{ij} \tag{2.60}$$

Where, $\varepsilon_{ij}^{'}$ is the strain divergence component, $\sigma_{ij}^{'}$ is the stress divergence component, $d\bar{\varepsilon}$ is equivalent strain increment and $\bar{\sigma}$ is equivalent stress. Ilyushin theory use widely to solve the small elastic-plastic problem. Considering the volume is constant in the plastic deformation, the above equation can be written as follows:

$$\left.\begin{aligned}
\varepsilon_x &= \frac{\bar{\varepsilon}}{\bar{\sigma}}[\sigma_x - \frac{1}{2}(\sigma_y + \sigma_z)] \\
\varepsilon_y &= \frac{\bar{\varepsilon}}{\bar{\sigma}}[\sigma_y - \frac{1}{2}(\sigma_z + \sigma_x)] \\
\varepsilon_z &= \frac{\bar{\varepsilon}}{\bar{\sigma}}[\sigma_z - \frac{1}{2}(\sigma_y + \sigma_x)] \\
\gamma_{xy} &= \frac{3\bar{\varepsilon}}{2\bar{\sigma}}\tau_{xy}, \gamma_{yz} = \frac{3\bar{\varepsilon}}{2\bar{\sigma}}\tau_{yz}, \gamma_{zx} = \frac{3\bar{\varepsilon}}{2\bar{\sigma}}\tau_{zx}
\end{aligned}\right\} \tag{2.61}$$

Total strain theory is simple and easy to use, Nadai theory even can be used in large deformation materials. But all of them need loading condition is simple, and the solution is complex if nonlinear physical equation is included. It is often necessary to make some simplification in order to briefly express the constitutive equation, e.g., ignoring the elastic deformation.

### 3.2.2 Plastic increment theory

The plastic incremental theory is also known as the flow theory. This theory focus on each loading moment in all loading history, and the stress state is not determined by the amount of plastic strain components but its instantaneous increments without the effects of loading history [39].

First incremental theory proposed by Saint Venant in 1870 [31]. And then M. Levy (1871) and von Mises (1913) established the general relationship between strain increment and stress deviator respectively, which is named as Levy-Mises theory or S. Venant-Mises theory. On this basis, L. Prandtl (1924) and A. Reuss (1930) proposed that the total deformation should also include the elastic part in addition to plastic deformation, established the Prandtl-Reuss incremental theory which considers elastic strain increment in plastic deformation. When the elastic strain and plastic strain are the same order of magnitude in dealing with small deformation problem, the application of Prandtl-Reuss theory is more reasonable but more complicated [40].

#### 1) Saint Venant flow equation

In 1870, S. Venant proposed a stress-strain rate equation based on the strain increment principle axis coincide with stress principal axis [41]. The expression is following:

$$\dot{\varepsilon}_{ij} = \dot{\lambda}\sigma'_{ij} \tag{2.62}$$

Where, the parameter $\dot{\lambda} = \frac{3}{2}\frac{\dot{\bar{\varepsilon}}}{\bar{\sigma}}$, and $\dot{\bar{\varepsilon}}$ is equivalent strain rate, $\bar{\sigma}$ is equivalent stress. $\sigma'_{ij}$ is the stress divergence component. The parameter $\dot{\lambda}$ equals zero in unloading condition.

**2) Levy-Mises flow equation**

In 1871, M. Levy reported a stress-strain rate relationship equation, and von Mises proposed respectively a similar equation in 1913 [42]. The equation called Levy-Mises equation. It includes following assumptions.

1) *Material is ideal rigid plastic material.*
2) *Material meets Mises yield criterion.*
3) *Stress principal axis overlap with strain increment principal axis in each loading moment.*
4) *The strain increment is positive proportional with stress deviator.*

The expression is following:

$$\mathrm{d}\varepsilon_{ij} = \sigma'_{ij}\mathrm{d}\lambda \tag{2.63}$$

Where, $d\lambda$ is the instantaneous positive scale coefficient which is dependent on material properties and deformation. The expression is following.

$$\mathrm{d}\lambda = \frac{3}{2}\frac{\mathrm{d}\bar{\varepsilon}}{\bar{\sigma}} \tag{2.64}$$

Where, $d\bar{\varepsilon}$ is equivalent strain increment, $\bar{\sigma}$ is equivalent stress. The parameter $d\lambda$ is various in different forming process, it equals zero in unloading condition.

**3) Prandtl-Reuss flow equation**

Prandtl-Reuss theory is developed from von Mises theory [43]. It includes the elastic strain in large deformation problem. Generally, the elastic strain can be ignored when the deformation is small, but if the deformation is large, for instance, when the elastic strain and plastic strain part is same order of magnitude, it should be considered elastic deformation part. That is the total deviatoric strain increment consist of two parts, the expression is following.

$$\mathrm{d}\varepsilon_{ij} = \mathrm{d}\varepsilon_{ij}^{\mathrm{p}} + \mathrm{d}\varepsilon_{ij}^{\mathrm{e}} \tag{2.65}$$

Where, total strain increment $d\varepsilon_{ij}$ is sum of plastic strain increment $d\varepsilon_{ij}^{p}$ and elastic strain increment $d\varepsilon_{ij}^{e}$. The relationship of parameter $d\varepsilon_{ij}^{p}$ between stresses is same with the Levy-Mises theory, the equation expressed as follow:

$$\mathrm{d}\varepsilon_{ij}^{\mathrm{p}} = \mathrm{d}\lambda \cdot \sigma'_{ij} = \frac{3}{2}\frac{\mathrm{d}\bar{\varepsilon}^{\mathrm{p}}}{\bar{\sigma}}\sigma'_{ij} \tag{2.66}$$

The elastic strain increment can be expressed as follow:

$$\mathrm{d}\varepsilon_{ij}^{\mathrm{e}} = \frac{1}{2G}\mathrm{d}\sigma'_{ij} + \frac{1-2\nu}{E}\mathrm{d}\sigma_m\delta_{ij} \tag{2.67}$$

Where, the $G$ is shear modulus, $E$ is young's modulus, $\nu$ is Poisson's ratio, $\sigma_m$ is the hydrostatic stress and $\delta_{ij}$ is deformation component. In the above three flow theories, S. Venant equations and Levy-Mises flow equation are essentially the same, the latter equation is the incremental form of the former one, both equation is without considering the influence of strain rate on material. The Prandtl-Reuss equation can be used for ideal elastic-plastic material, and it is also widely used so far.

Flow theory is more realistic for material deformation, and it can be used for reverse yield situation, while the deformation theory can not be. The deformation theory gives the same result with flow theory in the case of proportional loading condition. In short, the deformation theory can be used for proportional loading path, or approximately used for the path which is not far from the proportional loading path.

# 4. Theoretical prediction model for forming limits

In sheet forming process, the basic forming experiment are conducted to study forming limits of material, but it just can supply qualitative and comprehensive assessment for material formability, the result is difficult to make exact formability determination for complex industrial part. In 1965, Keeler and Goodwin proposed the forming limit diagram (FLD) and strain analysis method based on grid technology [47]. In a long time, it was the key research method to determine sheet metal formability. The forming limit diagram attempts to provide a graphical description of material failure tests, e.g., stamping test. Originally, the mechanical test is performed by circular grid measurement method. Firstly, a circular grid is placed on the test blank prior to deformation, and then measure the post-deformation ellipse that is generated from the forming deformation. By repeating the mechanical test to generate a range of stress states, the forming limit diagram can be finally obtained as a line at which necking or failure happen (Fig.3) [48-50].

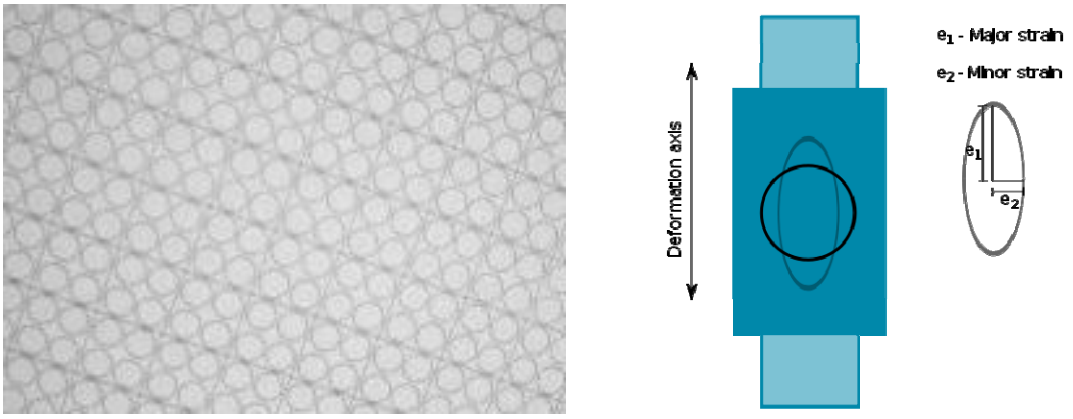


Fig.3. Definition of the deformation axes in forming limit diagram measurement [48-50].

The forming limit curves have been used as the criterion for the necking or failure prediction in sheet forming processes. It is well known that quite different strain limits can be achieved along different deformation paths [50]. The standard FLCs (forming limit curves), either obtained from experiments or calculated using a mathematical model, are under the assumption of simple loading states. However, in actual production, due to geometry and boundary friction conditions, the forming path often deviate from the linear strain paths, especially in the case of complex shapes and multi-step forming parts. In this way, the path created by the simple loading states can not match for limit strain prediction in FLD, and the FLD based on the complex strain path must be established according actual shape. Therefore, the study of complex loading paths on the influence of the FLD has been developed as a major research area in sheet metal forming study [51].

Meanwhile, the strain limits theoretical calculations on FLD have also been studied widely to predict the material forming limit based on mathematical model. Generally, various yield criteria and plastic constitutive relationships are used to describe necking and fracture by tensile instability conditions. Common yield criterion used for theoretical model include the Von Mises yield criterion, Hill series yield criterion, Hosford yield criterion and the Barlat series yield criterion, etc. And common instability criteria include diffuse instability criterion, Hill localized instability criteria, groove instability theory, etc [52].

## 4.1 Swift's maximum force criterion for diffuse necking

Swift's maximum force criterion was proposed by H. W. Swift in 1952 [53]. It is based on the fact that strength exhibits a uniform stress and strain distribution until the maximum force is reached in material ductility deformation. In uniaxial tension case, this can be expressed mathematically as follow:

$$dF_1 = 0 \tag{2.77}$$

Where, $F_1$ is material strength. If the material hardening curves obey power law, the plastic constitutive equation can be expressed as follow:

$$\sigma = K(\bar{\varepsilon}^p)^n \tag{2.78}$$

Where, $\sigma$ is equivalent stress, $K$ is stress coefficient, $\bar{\varepsilon}^p$ is plastic equivalent stain, $n$ is strain hardening exponent. Based on the incompressibility material property, it is easy to induce that the value of strain exponent $n$ equals the value of equivalent strain $\varepsilon^*$ when the force is reached maximum [7].

$$\varepsilon^* = n \tag{2.79}$$

For ductility material, the diffuse necking starts to form when the maximum force is reached. Then strains and stresses do no longer grow proportionally, and the stress and strain states are no longer homogeneous. Finally, all additional strains concentrate in a narrow band with respect to a certain angle to the loading direction. This phenomenon is called localized necking, and it is immediately followed by fracture.

Swift maximum force criterion also can be described as general form. Assuming the material is rigid-plasticity and volume constancy, it can be easily derived the following condition for stable plastic strain.

$$\frac{d\sigma_1}{d\varepsilon_1} \geq \sigma_1 \tag{2.80}$$

The yield condition is assumed to be given in the following form:

$$\bar{\sigma} - H(\bar{\varepsilon}^p) = 0 \tag{2.81}$$

Where, $H$ is a plastic hardening function. And the stress and strain rate ratios $\alpha$ and $\beta$ are introduced as follows:

$$\alpha = \frac{\sigma_2}{\sigma_1} \tag{2.82}$$

$$\beta = \frac{\dot{\varepsilon}_2^p}{\dot{\varepsilon}_1^p} \tag{2.83}$$

Where, $\sigma_1$ and $\sigma_2$ are the first and second principle stress, $\dot{\varepsilon}_1^p$ and $\dot{\varepsilon}_2^p$ are the first and second plastic strain rate respectively. The effective stress and effective strain can be expressed as follows:

$$\bar{\sigma} = F(\alpha)\sigma_1 = \bar{\sigma}(\sigma_1 = 1, \sigma_2 = \alpha)\sigma_1 \tag{2.84}$$

$$\dot{\bar{\varepsilon}}^p = G(\beta)\dot{\varepsilon}_1^p \tag{2.85}$$

Where, the function $F$ and $G$ are according stress and strain rate ratio function respectively. Using the above definitions, and assuming that $\alpha$ and $\beta$ are constant, the express of increment stress and strain can be expressed as follow:

$$\frac{d\sigma_1}{d\varepsilon_1} = \frac{\partial\sigma_1}{\partial\overline{\sigma}}\frac{\partial\overline{\sigma}}{\partial\overline{\varepsilon}^p}\frac{\partial\overline{\varepsilon}^p}{\partial\varepsilon_1} = \frac{1}{F}H'G' \tag{2.86}$$

Where, the notation $H' = \partial H / \partial\overline{\varepsilon}^p$ .

Accordingly, the condition for stable plastic strain can be expressed as follow:

$$G - \frac{H}{H'} \geq 0 \tag{2.87}$$

Specifically, when the hardening function can be approximated by a power law, it is easy to induce that the maximum force criterion can be expressed in simple form as follow:

$$\varepsilon_1 \leq n \tag{2.88}$$

## 4.2 Hill's criterion for localized necking

Hill's criterion for localized necking prediction proposed by R.Hill in 1952 [54]. It is based on the assumption that a localized necking is formed along a line with zero elongation. This assumption limits Hill's theory to strain states with negative second principal strain, *i.e.* to the left side of the Forming Limit Diagram (FLD). The assumptions are as follows [54, 55].

*1) The strain ratio is constant up to the point of localized necking.*

*2) The inclination of the line with zero elongation is constant in the all loading history.*

*3) The material is rigid-plastic.*

The derivation of Hill's criterion can be found in the literature of Hosford and Caddell [56]. The condition for localized necking can be expressed as follow:

$$\frac{d\sigma_1}{d\varepsilon_1} = (1+\beta_0)\sigma_1 \tag{2.89}$$

Where, $\sigma_1$ and $\varepsilon_1$ are the first principle stress and strain respectively, $\beta_0$ is the ratio of second principle strain and first principle strain. Hill's criterion is obviously similar with the swift's maximum force criterion for diffuse necking in certain condition. In the plane strain case, i.e., $\beta_0 = 0$ , the two criteria are identical, diffuse and localized necking appear simultaneously in this case. if hardening curve is described as power law, the condition for necking can be expressed as follows:

$$\varepsilon_1^* = \frac{n}{G(1+\beta_0)} \tag{2.90}$$

Like swift criterion, $G$ is the strain rate ratio function. It can be concluded that the limit curve is mainly dependent on the hardening curve according to Hill's theory. It can also be induced that the above equation represents an almost straight line in the principal strain plane.

## 4.3 The Marciniak-Kuczinski model for forming limits prediction

The Marciniak-Kuczynski (M-K) method is probably the most well known and widely used analytical FLC prediction method. This method proposed by Marciniak and Kuczynski by introducing imperfections into sheets to describe necking condition [57, 58]. This theory based on the material inhomogeneity assumption, i.e., there is groove which is perpendicular to the axial of maximum principal stress on the material surface (Fig.4). This initial inhomogeneity grows continuously and eventually forming a localized necking. From the figure, the region b is groove region, it is assumed the region a is homogeneous region and obey uniform proportional loading states. The *x, y, z* axes correspond to rolling, transverse and normal directions of the sheet, whereas 1 and 2 represent the principal stress and strain directions in the homogeneous region. Meanwhile, the set of axis aligned to the groove is represented by *n, t, z* axes, where *t* is the longitudinal one. In the sheet metal forming process, the material is firstly under plastic deformation with constant incremental stretching until maximum force happen. The M-K model assumes the flow localization occurs in the groove when a critical strain is reached in the homogeneous region. Then, the values of strain increments in two regions are compared with specific criterion (e.g., $\mathrm{d}\varepsilon_{1b} > 10\mathrm{d}\varepsilon_{1a}$ ) and finally the material major and minor strain limits are obtained on the forming limit diagrams. In sum, this model is based on the following hypothesis.

*1) Incompressibility material. The volume is constant with deformation:*

$$\mathrm{d}\varepsilon_1 + \mathrm{d}\varepsilon_2 + \mathrm{d}\varepsilon_3 = 0 \tag{2.91}$$

*2) Proportional loading state. a zone is in simple load state, the principal stress increased proportionally in a zone:*

$$\frac{\mathrm{d}\sigma_{1a}}{\sigma_{1a}} = \frac{\mathrm{d}\sigma_{2a}}{\sigma_{2a}} = \frac{\mathrm{d}\sigma_{ia}}{\sigma_{ia}} \tag{2.92}$$

*Moreover, strain is also proportional, and keeps constant in forming processes:*

$$\frac{\mathrm{d}\varepsilon_{3a}}{\mathrm{d}\varepsilon_{2a}} = \frac{\varepsilon_{3a}}{\varepsilon_{2a}} \tag{2.93}$$

*3) Second principal strain consistency. The increment of second principal strain is equal in a zone and b zone:*

$$d\varepsilon_{2a} = d\varepsilon_{2b} = d\varepsilon_2 \tag{2.94}$$

*4) Force equilibrium. Force equilibrium obeys at every moment in forming process:*

$$\sigma_{1a} e^a = \sigma_{1b} e^b \tag{2.95}$$

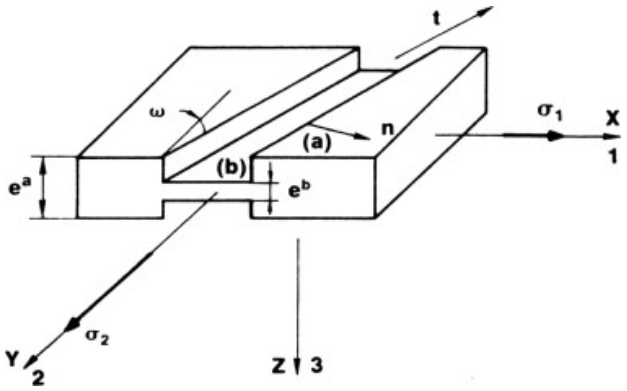


Fig.4. The M-K imperfection model [58]

An appropriate hardening law and yield function should be considered with the main equations of force equilibrium and compatibility equations in M-K model. Generally, the hardening law which represents the relationship between the equivalent stress and the equivalent strain can be expressed as follows:

$$\bar{\sigma}_{HR} = f_{HR}(\bar{\varepsilon}) \tag{2.96}$$

Where, $f_{HR}$ is a function of the equivalent strain $\bar{\varepsilon}$.

The yield function describes the yield surface and represents the yield relationship between the equivalent stress and the stress. It can be simply expressed by following function.

$$\bar{\sigma}_{YF} = f_{YF}(\sigma_{xx}, \sigma_{xy}, \sigma_{yy}) \tag{2.97}$$

Where, $f_{YF}$ is a function of the stress for both homogenous and groove regions. The associated flow rule which describes the relationship of strain increments is expressed as follows:

$$d\varepsilon_{ij} = d\bar{\varepsilon} \frac{\partial \bar{\sigma}_{YF}}{\partial \sigma_{ij}} \tag{2.98}$$

Where, $d\bar{\varepsilon}$ and $d\varepsilon_{ij}$ are the effective strain increment and related strain increment component with respect to the direction of $\sigma_{ij}$ respectively. And the rotation of the necking band during plastic deformation is calculated as follows:

$$tg(\omega + d\omega) = tg(\omega) \frac{1 + d\varepsilon_x^a}{1 + d\varepsilon_y^a} \tag{2.99}$$

The procedure of limit strains calculation by M-K analysis is following. Firstly, it is calculation of stress and strain in the homogenous region (zone a), in which small increments of major principal strain are imposed. Meanwhile, the strain ratio $\rho$ and stress ratio $\alpha$ are introduced as follows:

$$\rho^a = \frac{d\varepsilon_2^a}{d\varepsilon_1^a} \tag{2.100}$$

$$\alpha^a = \frac{\sigma_2^a}{\sigma_1^a} \tag{2.101}$$

The stress in homogenous region can be expressed as matrix format. And the strain increment can be described as matrix through flow rule. The expressions of stress and strain increment are defined as follows:

$$[\sigma]_{xyz}^a = \begin{bmatrix} \sigma_1^a & 0 \\ 0 & \sigma_2^a \end{bmatrix} \qquad [d\varepsilon]_{xyz}^a = \begin{bmatrix} d\varepsilon_1^a & 0 \\ 0 & d\varepsilon_2^a \end{bmatrix} \tag{2.102}$$

As for forming limits prediction, different strain paths are calculated for all conditions from uniaxial tension to biaxial expansion states. The stress and strain states in the groove reference frame can be calculated by following axes converting.

$$\begin{aligned} [\sigma]_{ntz}^a &= T' \cdot [\sigma]_{xyz}^a \cdot T \\ [d\varepsilon]_{ntz}^a &= T' \cdot [d\varepsilon]_{xyz}^a \cdot T \end{aligned} \tag{2.103}$$

Where, $T$ is the transformation matrixes which convert the stress and strain matrixes from the *x, y, z* direction to *n, t, z* direction.

Secondly, it is the calculation of stress and strain increments in groove region (zone b). The relevant values of the stress and strain increments in the imperfect region (zone b) are computed based on the equilibrium and compatibility equations.

Generally, in order to find the stress and strain increments in zone b, six equations is necessary to be calculated for six unknowns. However, the number of needed equations can be reduced to four based on previous hypothesis. And three of them can be calculated by two force equilibrium conditions and one geometrical compatibility equation. The equilibrium condition leads the following equations.

$$\begin{aligned} \sigma_{nn}^b e^b &= \sigma_{nn}^a e^a \\ \sigma_{nt}^b e^b &= \sigma_{nt}^a e^a \end{aligned} \tag{2.104}$$

And the compatibility law expresses as follows:

$$d\varepsilon_{tt}^{b} = d\varepsilon_{tt}^{a} \tag{2.105}$$

The equilibrium equations can be reduced as follows:

$$f\sigma_{nn}^{b} = \sigma_{nn}^{a} \qquad\qquad f\sigma_{nt}^{b} = \sigma_{nt}^{a} \tag{2.106}$$

Where, $f = e^{b}/e^{a}$ is named as the imperfect factor and can be described as following:

$$f = f_0 \exp(\varepsilon_{zz}^{b} - \varepsilon_{zz}^{a}) \tag{2.107}$$

Where, $f_0 = e_0^{b}/e_0^{a}$ is the initial ratio of imperfect factor, which is described the initial imperfect states of material.

Another equation is based on the energy constancy which expresses the incremental work per unit volume as follows:

$$d\varepsilon_{nn}^{b}\sigma_{nn}^{b} + d\varepsilon_{nt}^{b}\sigma_{nt}^{b} + d\varepsilon_{tt}^{b}\sigma_{tt}^{b} = d\bar{\varepsilon}^{b}\bar{\sigma}_{HR} \tag{2.108}$$

Finally, the four equations are following:

$$\begin{cases} F_1 = d\varepsilon_{nn}^{b}\sigma_{nn}^{b} + d\varepsilon_{nt}^{b}\sigma_{nt}^{b} + d\varepsilon_{tt}^{b}\sigma_{tt}^{b} - d\bar{\varepsilon}^{b}\bar{\sigma}_{HR} = 0 \\ F_2 = d\varepsilon_{tt}^{b} - d\varepsilon_{tt}^{a} = 0 \\ F_3 = f\sigma_{nn}^{b} - f\sigma_{nn}^{a} = 0 \\ F_4 = f\sigma_{nt}^{b} - f\sigma_{nt}^{a} = 0 \end{cases} \tag{2.109}$$

If the equation matrix is denoted as $[F] = [F_1 F_2 F_3 F_4]^{T}$ and the variable matrix is $[X] = [\sigma_{tt}^{b}\sigma_{nn}^{b}\sigma_{nt}^{b}d\bar{\varepsilon}^{b}]^{T}$, the Newton-Raphson method is often applied to compute this matrix.

$$[X]_{i+1} = [X]_i + [dX]_i \tag{2.110}$$

$$[dX]_i = -[J]_{ij}^{-1}[F]_j \tag{2.111}$$

Where, $[J]_{ij}$ is the Jacobean matrix defined as follows:

$$[J]_{ij} = \left[\frac{\partial F_i}{\partial X_j}\right] \tag{2.112}$$

In conclusion, the M-K criterion assumes that the plastic flow localization occurs when the equivalent strain increment in the imperfect region ($d\bar{\varepsilon}_b$) is ten times greater than in the homogeneous zone ($d\bar{\varepsilon}_a$). The computation is running until reaching the necking phenomenon. The corresponding strains accumulated at that moment in the homogeneous zone ($\varepsilon_1^{a}, \varepsilon_2^{a}$) are the forming limit strains.

## 4.4 The Modified Maximum Force Criterion for forming limits prediction

Another method for necking prediction is the so-called Modified Maximum Force Criterion (MMFC) by Hora *et al* [59]. This approach is widely used at present. It is based on the concept that the stress states transform to plane strain rate state if necking occurs. This transformation improve the material strengthens and postpones the fracture (Fig. 5).

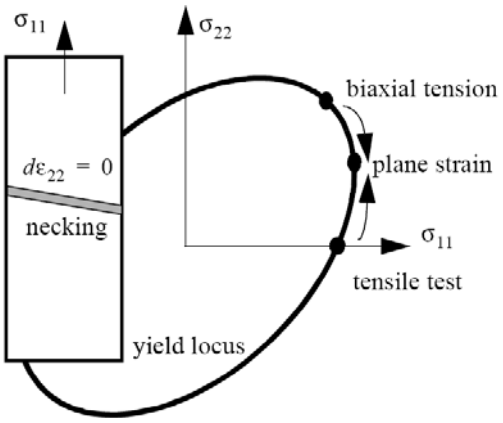


Fig.5. stress transform when necking happened in sheet forming [59]

The brief form of MMFC criterion can be expressed mathematically as follows:

$$\frac{\partial \sigma_{11}}{\partial \varepsilon_{11}} + \frac{\partial \sigma_{11}}{\partial \beta} \cdot \frac{\partial \beta}{\partial \varepsilon_{11}} \le \sigma_{11} \tag{2.113}$$

Where, $\sigma_{11}$ and $\varepsilon_{11}$ are respectively the stress and strain in the first principal axis direction. $\beta$ is the strain increment ratio, the expression is following.

$$\beta = \frac{\Delta \varepsilon_{22}}{\Delta \varepsilon_{11}} \tag{2.114}$$

Similarly, the stress ratio $\alpha$ is defined as follows:

$$\alpha = \frac{\Delta \sigma_{22}}{\Delta \sigma_{11}} \tag{2.115}$$

Meanwhile, the following relationship can be generally established with function.

$$\sigma_{11} = f(\alpha)\overline{\sigma} \qquad\qquad \Delta\overline{\varepsilon} = g(\beta)\Delta\varepsilon_{11} \tag{2.116}$$

Where, $\overline{\sigma}$ and $\Delta\overline{\varepsilon}$ are the equivalent stress and the equivalent strain increment respectively. The description of the modified maximum force criterion takes the general form as follows:

$$H' = \frac{\left( f(\alpha) + \dfrac{f'(\alpha)g(\beta)\beta}{\beta'(\alpha)\bar{\varepsilon}} \right)}{f(\alpha)g(\beta)} H \tag{2.117}$$

Where, $H = H(\bar{\varepsilon})$ is the hardening curve.

Specifically, if material hardening property is described by power law, a limit strain can be directly expressed as follows:

$$\varepsilon_1^* = n + \frac{f'}{f}\frac{\beta}{\beta'} \tag{2.118}$$

Where, $n$ is strain hardening exponent in constitutive equation. One advantage of the MMFC is that the critical strains for a given strain path can be directly calculated, without performing an incremental analysis in other model, e.g., M-K method. Thus, the MMFC criterion can be used as a failure criterion in finite element analysis. And it is widely used in the commercial FE code nowadays.

# 5. Conclusion

In this chapter, the fundamental theories of sheet metal forming have been discussed. The material forming theory have developed for long history and been improved to describe various new material property nowadays, especially for material plastic forming theory, which mainly include such as yield function, constitutive equation, forming limit prediction, etc.

Firstly, yielding is an important property of material, which is the threshold of plasticity. Isotropic and anisotropic material yield functions have been widely discussed by many researchers and engineer. In this project, the Hill's thickness anisotropic yield theory is used in study.

Secondly, material plastic constitutive relationships include total strain theory and increment theory. Total strain theory describes stress and strain relationship without considering deformation history, while increment theory describes material flow with strain increment in whole deformation history. In this project, the constitutive relationship of AZ31 Magnesium alloy is study based on tensile test. The details will be presented in the next chapter.

Thirdly, material forming limit is a focused issue in sheet forming field. Lots of forming limit prediction models have proposed based on material necking and instability study. The difficulty of forming limit theoretical prediction is deformation mechanism. The M-K model and modified maximum force criterion (MMFC) are two mainly used prediction models. The

M-K model introduce imperfect factor, and assume that localized necking occur at initial surface defect area, while MMFC is based on the plain strain state for necking. In this project, the theoretical prediction of AZ31 magnesium alloy forming limit have been studied by M-K model as first trials, the analysis details will be presented in chapter 4.

# 6. References


[1] G. Dieter, Mechanical Metallurgy, McGraw-Hill, 1986.

[2] R. A. Flinn, P. K. Trojan. Engineering Materials and their Applications. Boston: Houghton Mifflin Company, 1975.

[3] E. P. Degarmo, J. T. Black, R. A. Kohser. Materials and Processes in Manufacturing (9th ED). Wiley, 2003.

[4] F. P. Beer, E. R. Johnston, J. T. Dewolf. Mechanics of Materials (3rd ED.). McGraw-Hill, 2001.

[5] C. Ross. Mechanics of Solids. Albion Horwood Pub, 1999.

[6] J. Callister, D. William. Materials Science and Engineering - An Introduction (5th ED.). John Wiley and Sons, 2000.

[7] W. F. Hosford, R. Caddell. Metal Forming: Mechanics and Metallurgy. 3rd Edition. Cambridge University, 2007.

[8] J. Chakrabarty. Theory of Plasticity. Third edition, Elsevier, Amsterdam, 2006.

[9] J. C. Simo, J. R. Hughes. Computational Plasticity. Spinger, 1998.

[10] J. Cao, H. Yao, A. Karafillis, M. C. Boyce. Prediction of localized thinning in sheet metal using a general anisotropic yield criterion. International Journal of Plasticity, Vol.16, Iss: 9 (2000), pp. 1105-1129.

[11] H. Tresca. Mémoire sur l'écoulement des corps solides soumis à de fortes pressions. C.R. Acad. Sci. Paris, Vol.59 (1864), pp. 754.

[12] R. Von Mises. Mechanik der festen Körper im plastisch deformablen Zustand. Göttin. Nachr. Math. Phys., Vol.1 (1913), pp. 582–592.

[13] Ford. Advanced Mechanics of Materials, Longmans, London, 1963.

[14] W. M. Huang, X. Y. Gao. Tresca and von Mises yield criteria: a view from strain space. Philosophical Magazine Letters, Vol.84, Iss: 10 (2004), pp. 625-629.

[15] R. Hill. The Mathematical Theory of Plasticity. Oxford, Clarendon Press. 1950.

[16] W. A. Backofen, W. F. Hosford, J. J. Burke. Texture hardening, Trans., ASM55, (1962), pp. 264-267.

[17] W. F. Hosford. Comments on Anisotropic Yield Criteria, International Journal of Mechanical Sciences, Vol. 27, No. 7/8 (1985), pp. 423-427.

[18] F. Barlat. Crystallographic textures, anisotropic yield surfaces and forming limits of sheet metals. Materials Science and Engineering, 91 (1987), pp.55-72.

[19] A. Graf, W. F. Hosford. Calculations of forming limit diagrams. Metall. Trans. Vol.

21A (1990), pp. 87-96.

[20] F. Barlat, J. Lian. Plastic Behavior and Stretchability of Sheet Metals. Part I: A Yield Function for Orthotropic Sheets under Plane Stress Conditions. International Journal of Plasticity, Vol. 5 (1989), pp. 51-66.

[21] F. Barlat, D. J. Lege, J. C. Brem. A six-component yield functions for anisotropic materials. International Journal of Plasticity, Vol.7 (1991), pp. 693-712.

[22] F. Barlat, R. C. Becker. Yielding description for solution strengthened aluminum alloys. International Journal of Plasticity, Vol.13 (1997), pp. 385-401.

[23] F. Barlat, Y. Maeda, K. Chung. Yield function development for aluminum alloy sheets. Journal of the Mechanics and Physics of Solids, Vol.45, Iss: 11/12 (1997), pp. 1727-1763.

[24] F. Barlat, J. C. Brem. Plane stress yield function for aluminum alloy sheets-part 1: theory. International Journal of Plasticity, Vol.19 (2003), pp.1297-1319.

[25] F. Barlat, H. Aretz, J. W. Yoon. Linear transformation-based anisotropic yield functions. International Journal of Plasticity, Vol. 21 (2005), pp. 1009-1039.

[26] J. W. Yoon, F. Barlat, J. J. Gracio. Anisotropic strain hardening behavior in simple shear for cube textured aluminum alloy sheets. International Journal of Plasticity, Vol. 21 (2005), pp. 2426-2447.

[27] K. J. Van Vliet. Mechanical Behavior of Materials. MIT open resource, 2006.

[28] F. Beer, E. R. Johnston, J. Dewolf, D. Mazurek. Mechanics of Materials. McGraw Hill, 2009.

[29] W. Lewin. Hook's Law, Simple Harmonic Oscillator. MIT open Course 8.01: Classical Mechanics, Lecture 10, 1999.

[30] J. Lubliner. Plasticity Theory. Macmillan Publishing, New York, 1990.

[31] S. P. Timoshenko. History of strength of materials. McGraw-Hill, 1953.

[32] L. M. Kachanov. Fundamentals of the Theory of Plasticity. Dover Books.

[33] A. S. Khan, S. Huang. Continuum Theory of Plasticity. Wiley, 1995.

[34] J. Vernon. Introduction to Engineering Materials, 3rd ED. New York, Industrial Press, 1992.

[35] S. H. Crandall, T. J. Lardner. An Introduction to the Mechanics of Solids. McGraw-Hill, 1999.

[36] J. Chakrabarty. Theory of Plasticity (Third edition). Elsevier, Amsterdam, 2006.

[37] A. Nadai. Theory of Flow and Fracture of Solids. Vol. 2, McGraw-Hill, 1963.

[38] V.S. Lensky, E.V. Lensky. Constitutive equations and physical reliability in the modern

theory of plasticity. International Journal of Engineering Science, Vol. 32, Iss: 5 (1994), pp. 743-753.

[39] E. Onate, S. Oller, J. Oliver, J. Lubliner. A constitutive model for cracking of concrete based on the incremental theory of plasticity. Engineering Computations, Vol. 5 Iss: 4 (1988), pp. 309-319.

[40] J. D. Anderson. A history of Aerodynamics. Cambridge, 1997.

[41] S. Chirita. Saint-Venant's Principle in Linear Thermoelasticity. Journal of Thermal Stresses, Vol. 18 (1995), pp. 485.

[42] D. Banabic, E. Dannenmann. Prediction of the influence of yield locus on the limit strains in sheet metals. Journal of Materials Processing Technology, Vol.109, Iss: 1-2 (2001), pp. 9-12.

[43] C. Miehe. On the representation of Prandtl-Reuss tensors within the framework of multiplicative elastoplasticity. International Journal of Plasticity, Vol.10, Iss: 6 (1994), pp. 609-621.

[44] F. A Nichols. Plastic instabilities and uniaxial tensile ductilities. Acta Metallurgica, Vol. 28, Iss: 6 (1980), pp. 663-673.

[45] R. P. Skelton, H. J. Maier, H. J. Christ. The Bauschinger effect, Masing model and the Ramberg-Osgood relation for cyclic deformation in metals. Materials Science and Engineering: A, Vol. 238, Iss: 2 (1997), pp. 377-390.

[46] H. J. Kleemola, M. A. Nieminen. On the strain-hardening parameters of metals. Metallurgical and Materials Transactions B, Vol. 5, Num: 8 (1974), pp. 1863-1866.

[47] S. P. Keeler. Determination of Forming Limits in Automotive Stampings. Society of Automitive Engineers, Technical paper No. 650535. 1965.

[48] S. S. Hecker. Formability of Aluminum Alloy Sheets. Journal of Engineering Materials and Technology, Transactions of the ASME, (1975), pp. 66-73.

[49] S. S. Hecker. Simple Technique for Determining Forming Limit Curves. Sheet Metal Industries, (1975), pp. 671-676.

[50] S. S. Hecker. Experimental Studies of Yield Phenomena in Biaxially Loaded Metals, in Constitutive Equations in Viscoplasticity: Computational and Engineering Aspects. ASME, Yew York, (1976), pp. 1-33.

[51] A. Barata Da Rocha, J. M. Jalinier. Plastic Instability of Sheet Metals under Simple and Complex Strain Paths, Trans Iron Steel Inst Jpn, Vol. 24, no. 2 (1984), pp. 132-140.

[52] A. Barata Da Rocha, F. Barlat, J. M. Jalinier. Prediction of the Forming Limit Diagrams of Anisotropic Sheets in Linear and Non-linear Loading. Materials Science and

Engineering, Vol. 68 (1985), pp. 151-164.

[53] H. W. Swift. Plastic Instability under Plane Stress, Journal of the Mechanics and Physics of Solids, vol. 1 (1952), pp. 1-18.

[54] R. Hill. On Discontinuous Plastic States, With Special Reference to Localized Necking in thin sheets, Journal of the Mechanics and Physics of Solids, Vol. 1 (1952), pp. 19-30.

[55] R. Hill. Theoretical Plasticity of Textured Aggregates, Math. Proc. Camb. Phil. Soc., Vol. 55 (1979), pp. 179-191.

[56] W. F. Hosford, R. Caddell. Metal Forming: Mechanics and Metallurgy. 3rd Edition, Cambridge University, 2007.

[57] Z. Marciniak, K. Kuczynski. Limits Strains in The Processes of Stretch-Forming Sheet Metal, International Journal of Mechanical Sciences, Vol. 9 (1967), pp. 609-620.

[58] Z. Marciniak, K. Kuczynski, T. Pokra. Influence of The Plastic Properties of A Material On The Forming Limit Diagram For Sheet Metal In Tension, International Journal of Mechanical Sciences, Vol. 15 (1973), pp. 789-805.

[59] P. Hora. A prediction method for ductile sheet metal failure using FE-simulation, NUMISHEET, Dearborn, MI, USA, (1996), pp. 252-256.

# Chapter 3 Thermal Ductility of AZ31 magnesium alloy

## Contents

# 1. Introduction

The warm tensile tests of AZ31-O magnesium alloy are performed for the determination of hardening and mechanical behaviors. The original obtained data from tensile test is load and stroke, and then the stress and strain can be derived by relevant theoretical equations [1]. In addition, three different angle (0°, 45° and 90°) according rolling direction test specimens are used to study the material anisotropy properties. In order to determine the critical strains at failure point, a strain measurement system working by correlation of digital images is used. This system is ARAMIS© and will briefly present in the following section [2]. Finally, the constitutive equation is identified according stress-strain curves, and it is analyzed by power law type model and Gavrus law model which include an item to describe the softening behavior of material. The genetic algorithm has been used to fit the global optimal parameters. Then the comparison between the fitted and experimental data proves the effectiveness of the models.

The material used in this study is commercial AZ31-O magnesium alloy sheet which includes 3% aluminum and 1% zinc with a thickness of 1.2mm. Table.1 shows the main composition of material. The microstructure of the as-received alloy sheet is shown as follows (Fig.1). It is found that the sheet has non-uniform coarse grains and the average grain size is about 15μm measured from microscope in both rolling direction (RD) and transverse direction (TD).

Table.1. The composition of as-received AZ31-O sheet (wt. %)

| Al | Zn | Mn | Ca | Si | Cu | Ni | Fe | Other |
|---|---|---|---|---|---|---|---|---|
| 3.0 | 1.0 | <0.2 | <0.04 | <0.1 | <0.05 | <0.005 | <0.005 | <0.3 |

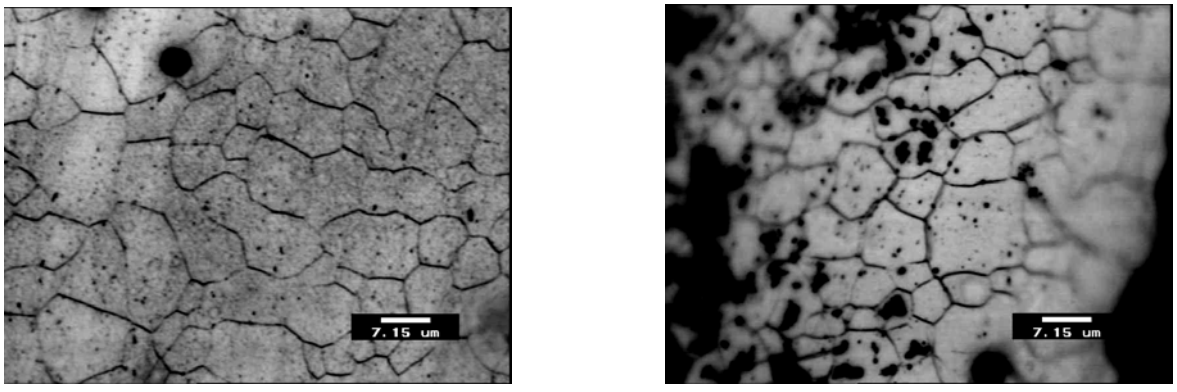


(a) Rolling direction (b) Transverse direction

Fig.1. Microstructure of as-received AZ31-O sheets

# 2. Warm uniaxial tensile test

Tensile test is probably the most fundamental mechanical test performed in material, which are simple, relatively inexpensive and fully standardized. The results from experiment are commonly used to select a material for quality control and to predict how a material will react under other types of forces. Properties that are directly measured from tensile test are ultimate tensile strength, maximum elongation and reduction in area, etc. From these measurements, the other properties, e.g. Young's modulus, Poisson's ratio, yield strength, and strain-hardening characteristics can also be determined. Generally, tensile test are used for the determination of following parameters [3, 4].

1) The initial yield stress and the hardening characteristic of the material.
2) The anisotropy of the material characterized by the evolution of the yield stress or the Lankford coefficient with the orientation of the specimen. This orientation is measured with respect to the rolling direction.
3) The strain rate sensitivity of the material by varying the imposed velocity at the ends of the specimen.

## 2.1 Experimental setup

Since magnesium alloy exhibits poor ductility in lower temperature, the forming processes are performed at high temperature in industry. So, the tensile tests are warm forming experiment. In this project, tensile tests are carried out in an Instron 1341H® tensile testing machine at various temperatures between room temperature and $300^0$C (Fig.2). In warm uniaxial tensile test, the furnace play an important role in controlling the deformed temperature, the in-situ furnace using in this test adjust temperature by special temperature compensation mechanism to gain precise temperature controlling. The operating temperature range from $-60^0$C to $250^0$C, temperature control accuracy is up to $\pm 2^0$C with a temperature compensation system to satisfy the precision requirement [5]. At $300^0$C, another furnace has been used and temperature is also controlled precisely. Before testing, each specimen has been tempered at the test temperature for 30 minutes.

(a) Test machine (b) In-Situ furnace

Fig.2. Instron high temperature tensile machine and In-Situ furnace

The specimen geometries are designed by standard ISO 6892-2 which specifies a method of tensile testing of metallic materials at temperatures higher than room temperature [6]. The specimens cut with the dimensions 150mm × 60mm, and the fillet radius is 32mm, the gauge length is 40mm. The gauge length area has been marked with arbitrary electro-etched pattern by ARAMIS measuring requirement. Meanwhile, in order to study material anisotropy property, the specimens have been cut along several orientations with respect to the rolling direction. Three values for the angle are used ($0^0$, $45^0$, $90^0$ degrees respectively). The Fig.3 shows the specimen dimensions and orientation of the tensile test specimens.

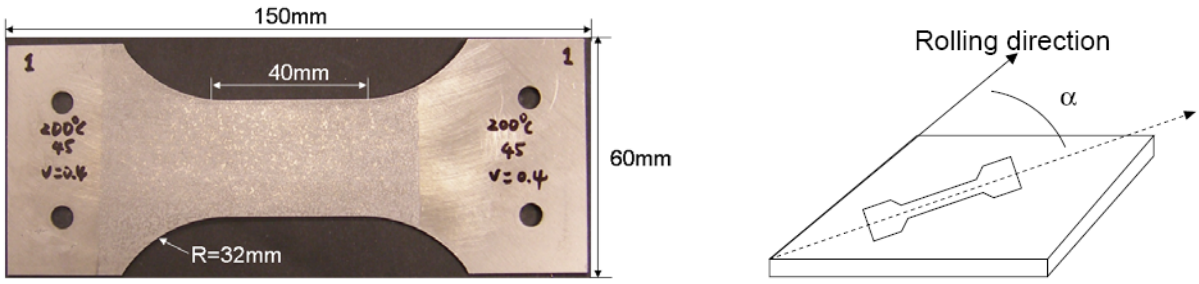


Fig.3. Tensile test specimens and the orientation with respect to the rolling direction

The Instron 1341H® machine is a hydraulic tensile test machine with the maximum load of 300KN. The specimens are clamped at both ends and a constant velocity is applied at one of these ends. The tests are carried out with three constant velocities for the determination of sensitivity, i.e., 0.04mm/s, 0.4mm/s and 4mm/s respectively. Then according the dimension of specimens, the strain rate can be derived approximately with relevant equation as $0.001s^{-1}$, $0.01s^{-1}$ and $0.1s^{-1}$ respectively. Meanwhile, all specimens are polished prior to test using diamond pastes to remove major scratches in order to avoid fracture occurring at undesired location of the specimen. The variations of load and stroke are recorded continuously by a computer equipped with an automatic data acquisition system. The true stress and true strain

are derived from the measurement of the nominal stress-strain relationship according to the transformation equation [7]. The stress and strain express as follows:

$$\sigma_N = \frac{F}{S_0} \qquad \varepsilon_N = \frac{\Delta l}{l_0}$$

$$\sigma_T = \sigma_N e^{\varepsilon_N} \quad (e^{\varepsilon_N} \approx 1+\varepsilon_N, \text{when } \varepsilon_N \ll 1)$$

$$\varepsilon_T = \ln(1+\varepsilon_N) \tag{3.1}$$

Where, $\sigma_T$, $\sigma_N$, $\varepsilon_T$ and $\varepsilon_N$ are true stress, nominal stress, true strain and nominal strain respectively.

## 2.2 Result analysis

### 2.2.1 Experimental result

Fig.4 shows the deformed tensile test specimens of AZ31 magnesium alloy sheet at various temperature and velocities. It is found that the elongation increase remarkably with increasing temperature and decreasing test velocity. It is evident that the ductility is substantially enhanced with higher temperature and lower test velocity.

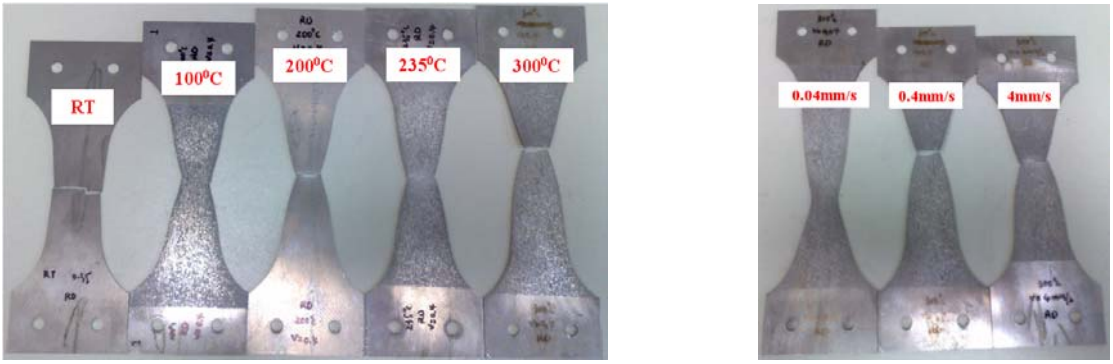


(a) Specimens at various temperatures (v=0.4mm/s, RD) (b) Specimens at various velocity (T=300$^0$C, RD)

Fig.4. Deformed specimens at different temperatures and velocities

The same phenomenon happened in both test specimens with rolling direction and transverse direction (Fig.5). It is shown that the elongation increase with the decreasing velocity at 200$^0$C temperature in both direction. The fracture always happened close the center of specimen, and the necking phenomenon is obvious for each specimen, especially at high temperature.

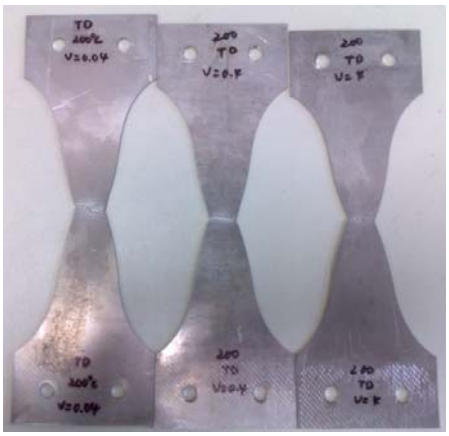

(a) Specimens at transverse direction (TD)

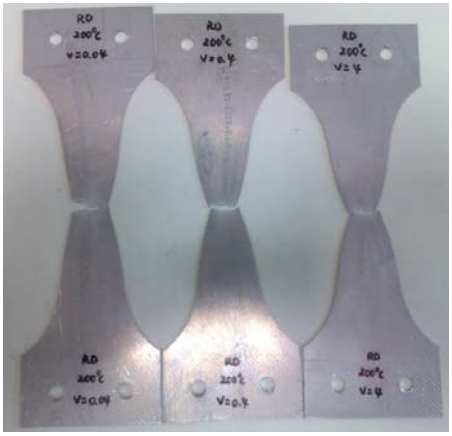

(b) Specimens at rolling direction (RD)

Fig.5. Deformed specimens at different forming direction (T=200$^0$C)

As for instance, the mechanical properties of AZ31magnesium alloy at various temperatures under a strain rate of 0.01s$^{-1}$ are shown in Table.2. The elongation to fracture, yield stress and tensile strength are basic material data to describe the material mechanical behavior. From the table, it is intuitively shown that the elongation increases but the yield stress and tensile strength decrease with temperature increasing.

Table.2. Mechanical properties of AZ31 magnesium alloy at various temperatures ( $\dot{\varepsilon}$ =0.01s$^{-1}$)

| Temperature ($^0$C) | Elongation (%) | Yield stress (MPa) | Tensile strength (MPa) |
|---|---|---|---|
| RT | 28.5 | 171.1 | 262.0 |
| 100 | 58.5 | 148.4 | 209.7 |
| 200 | 80.9 | 87.3 | 113.2 |
| 235 | 85.0 | 75.8 | 85.9 |
| 300 | 90.1 | 43.2 | 49.1 |

The experimental tensile strength and yield stress at various temperatures and strain rates are shown in Fig.6. In Fig.6 (a), tensile strength decreases significantly with temperatures at each constant strain rate, indicating obvious softening of the alloy at warm temperatures. The differences in tensile strength under various strain rates become more distinct with increasing temperatures, showing clear strain rate sensitivity. In Fig.6 (b), the yield stress decreases dramatically with temperature at each constant strain rate, and the discrepancy is higher between lower strain rates. The yield stress is closed when strain rate are the 0.01s$^{-1}$ and 0.1s$^{-1}$ at 200$^0$C. The deformations are more sensitive at lower strain rate, consequently the yield stress decreases at lower strain rate. In addition, the experiment reliability has been validated by repeating each test with three times.

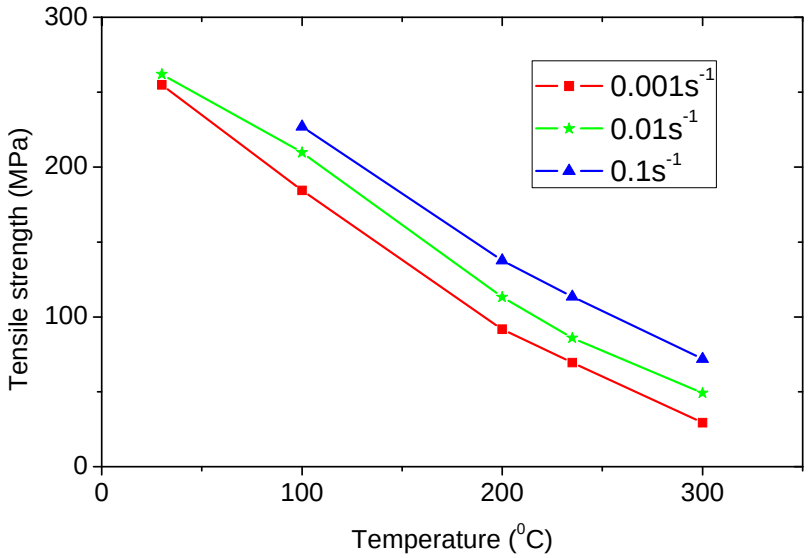


(a) Tensile strength vs. temperature

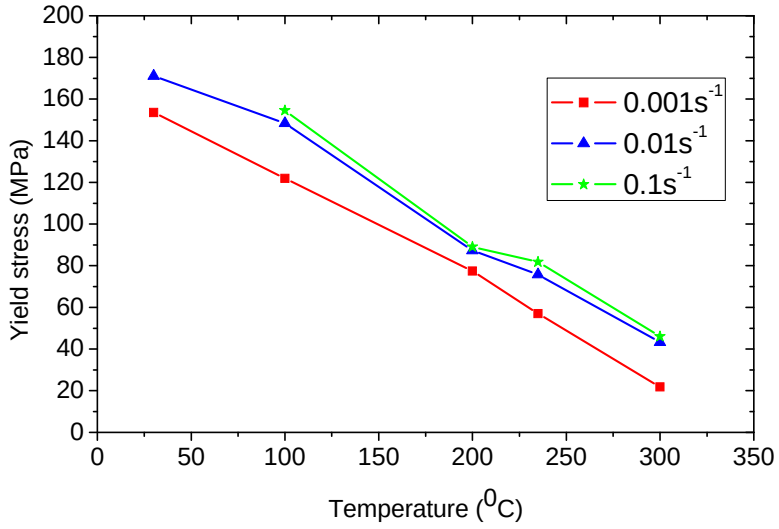


(b) Yield stress vs. temperature

Fig.6. Influence of strain rate and temperature on tensile strength and yield stress of AZ31 alloy (RD)

The load-stroke curves are shown at various temperature and velocity in Fig.7. Firstly, there is distinct strain hardening for the stress strain curves at room temperature. The softening exists at high temperature, and this phenomenon is more visible with temperature increasing. Secondly, the elongation to fracture is low at room temperature and high strain rate, but it is higher with higher temperature and lower strain rate. As for more intuitive comparison, the load-stroke curves at various temperatures when strain rate equal $0.01s^{-1}$ have been shown in Fig.7 (b). The hardening is extremely apparent at lower temperature, but softening phenomenon is more obvious with temperature increasing. In addition, there are

some “jumps” on the load-stroke curves, especially at the lower strain rate. This phenomenon is visible at $100^0$C when the strain rate equal $0.001s^{-1}$, it is still exist after repeating several times in same test condition. It is probably because the microstructures of AZ31 are suffered critical evolution in this specific test condition. This phenomenon is necessary to investigate deeply in future work. Finally, the true stress and strain are obtained by the previous mentioned transformation equation. In the application, true stress strain curves are derived after optimizing calculation from initial load stroke data.

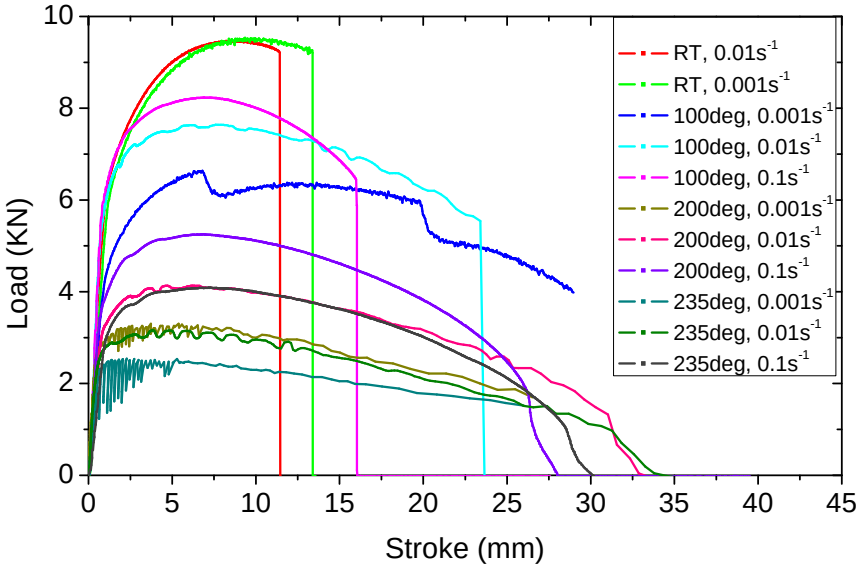


(a) Load - stroke curves at various temperature and strain rate

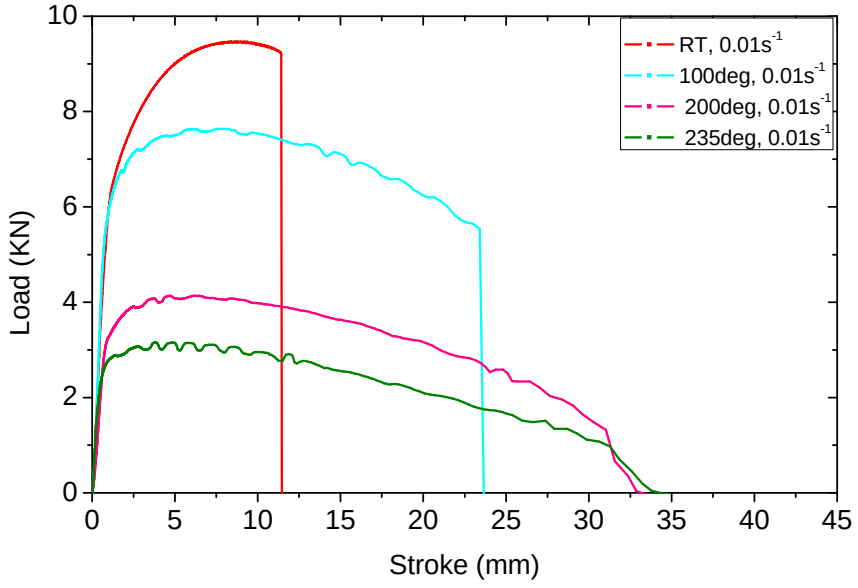


(b) Load - stroke curves at various temperature when $\dot{\varepsilon}$ =0.01$s^{-1}$

Fig.7. Load - stroke curves for the AZ31 alloy sheet at the various temperatures and strain rate (RD)

The true stress-true strain curves derived under various temperatures and strain rates are shown in Fig.8. These curves are plotted up to appearance of fracture phenomenon. It is well known the derivation equations are available at uniform deformation stage, the focus are fixed before necking and fracture phenomenon. It can be seen that the flow stress decreases with increasing temperature while the strain to fracture increases with increasing temperature, and the yield stress is higher at the higher strain rate. At room temperature, the strain hardening phenomenon is clear for each strain rate. But at higher temperatures, the flow stress is practically independent of strain, no significant strain hardening is observed for any specimens, especially at $300^0$C.

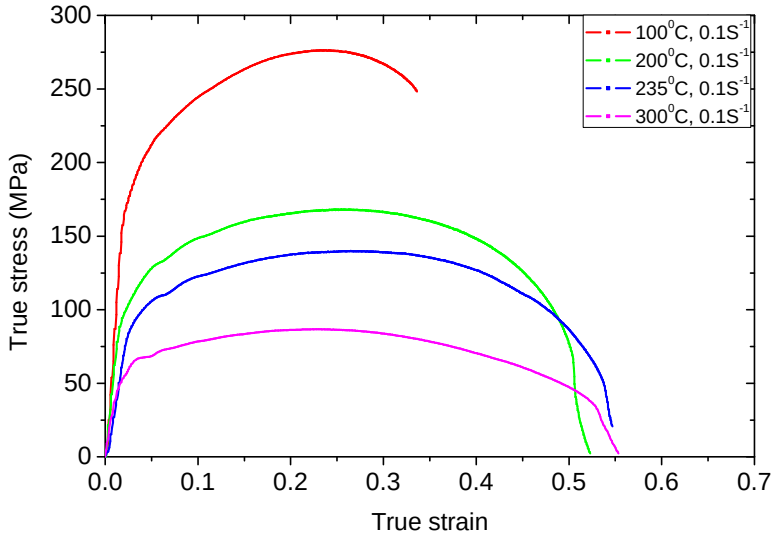


(a) Stress-strain curves at $\dot{\varepsilon}$ =0.1s$^{-1}$

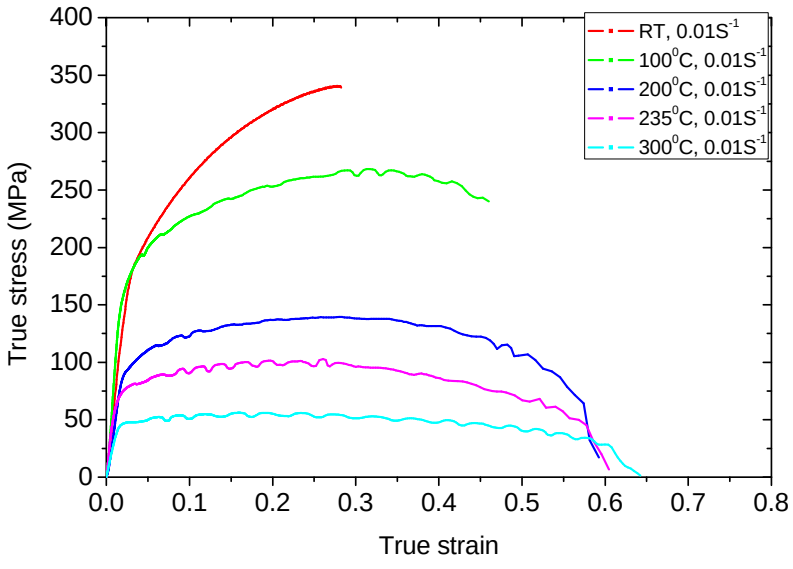


(b) Stress-strain curves at $\dot{\varepsilon}$ =0.01s$^{-1}$

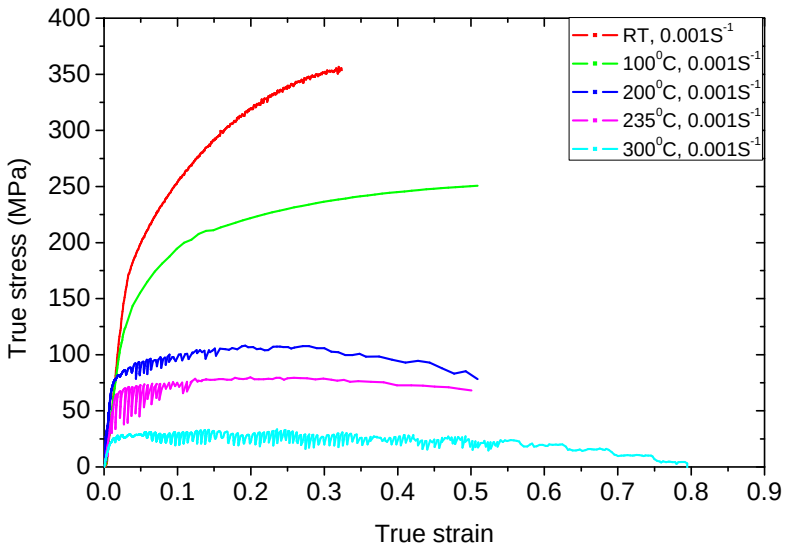


(c) Stress-strain curves at $\dot{\varepsilon}$ =0.001s$^{-1}$

Fig.8. True stress-true strain curves under various temperatures and strain rates

### 2.2.2 ARAMIS strain measurement

As presented previously, the ARAMIS© system is available in CEMEF. Its operation procedures are briefly shown in Fig.9.

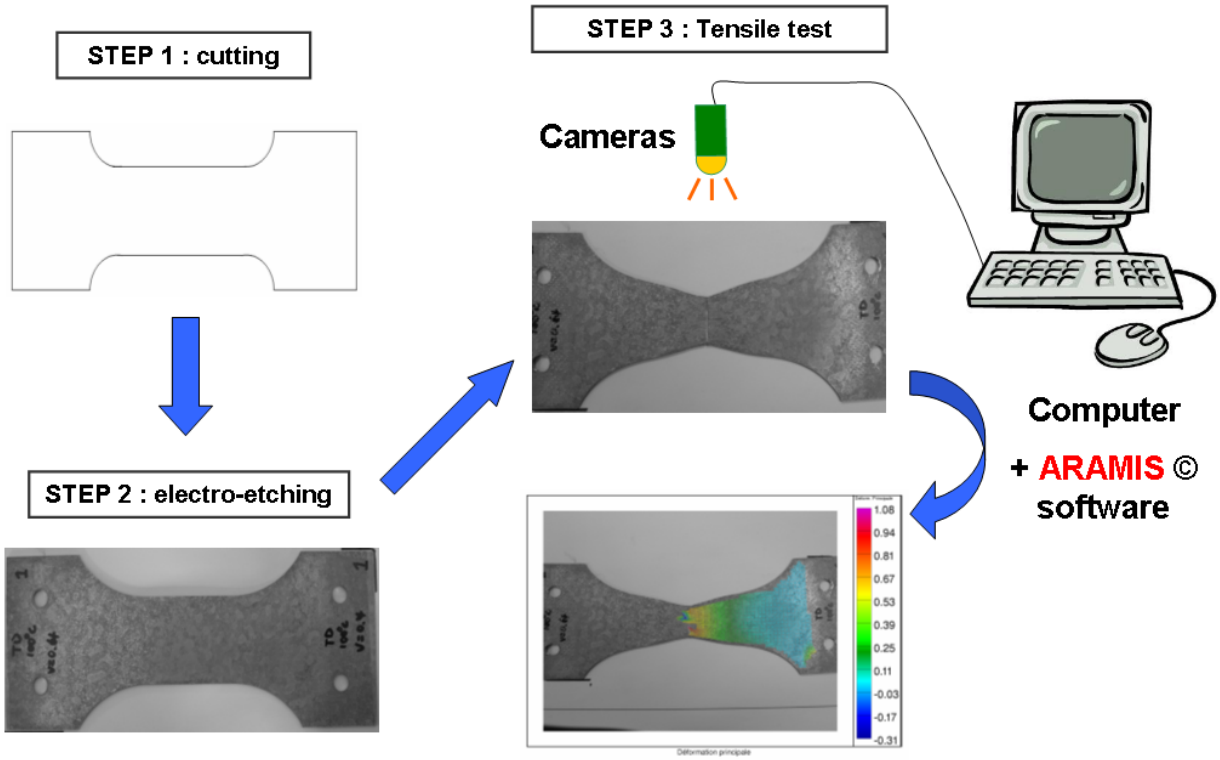


Fig.9. The ARAMIS system operation procedure in tensile test

Firstly, the specimens are prepared and polished to remove major scratches on the surface. Then the step 2 is important, and the quality of pattern plays an important role in the correlation of the strain measurement. The pattern should exhibit a high contrast to the surface. Otherwise, the computation can not be carried out. In this project, the arbitrary pattern is used by electro-etching method. The black and white particle distribute clearly and matching the ARAMIS computation. Finally, the measured strains are obtained after test by ARAMIS, and the 2D images are gotten by one camera.

Generally, two methods have been used to get pattern in the ARAMIS system which is painting method and electro-etching method. The electro-etching pattern has been used in this project because the painting disappears at high temperature for AZ31 magnesium alloy warm forming. As for example, the strain measurement at $100^0$C has been shown in Fig.10. The strain contour overlay the deformed specimens, and the necking phenomenon is clearly shown on the graph. Even the precise necking location can be tracked on the overlaid deformation graph.

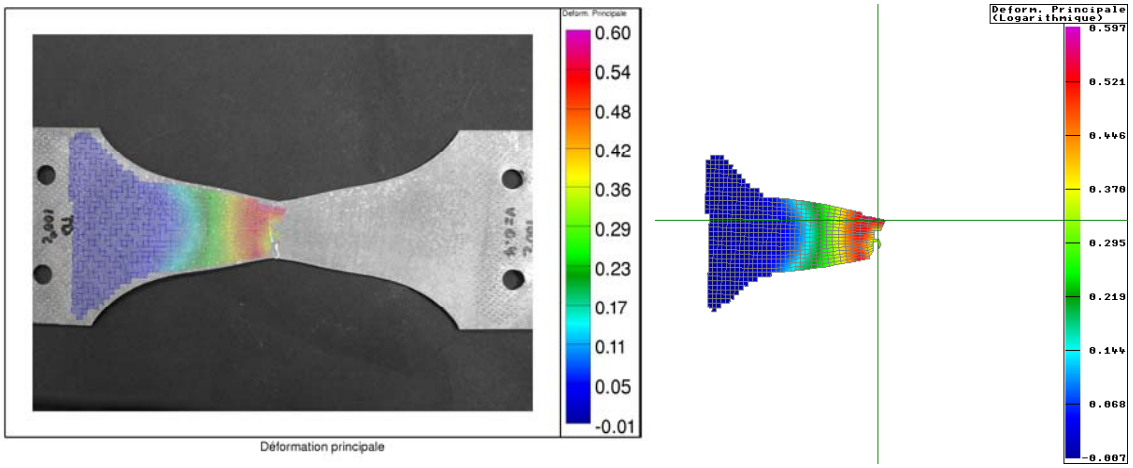


Fig.10. ARAMIS measurement at $100^0$C in transverse direction ( $\dot{\varepsilon}$ =0.01$s^{-1}$)

Meanwhile, in order to check the reliability of experiments, the comparison is made between the results from ARAMIS© system and extensometer record from tensile test. The result should be very close as long as the strain field remains homogeneous on the specimen. Fig.11 shows the evolution of the longitudinal strain measured from the tensile setup and ARAMIS system. And the measurements obtained by correlation are in good agreement with the measurements carried out on the tensile setup.

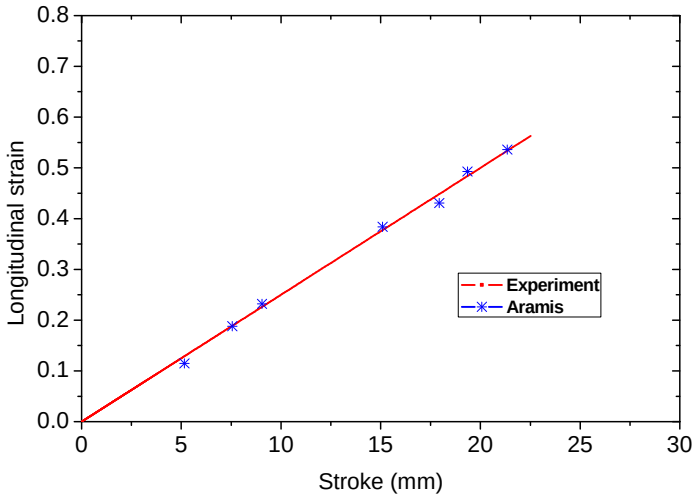


Fig.11 Comparison between the strains measured from the tensile set-up and ARAMIS system ($200^0$C, $0.01s^{-1}$)

### 2.2.3 Anisotropy property

For the measurement of Lankford coefficients, three type specimens which have been cut along three orientations based on the rolling direction are used in order to measure the anisotropy property of AZ31. Lankford coefficient, denoted *r*, is given by the ratio between the lateral and thickness plastic strains during a tensile test (Fig.12) [8].

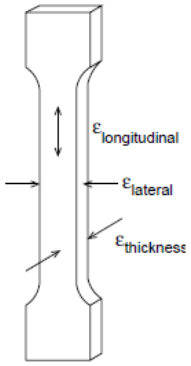


$$r = \frac{\varepsilon^{p}_{lateral}}{\varepsilon^{p}_{thickness}}$$

Fig.12. Definition of Lankford coefficients in the test [8]

In this project, all the tensile tests for a given temperature, orientation and strain rate are carried out two or three times in order to check the test reliability. The initial load-elongation curves of three directions at $100^0$C and $200^0$C are shown in Fig.13. It is found that the Magnesium alloys AZ31 exhibit anisotropy at lower temperature, but the three direction curves are close at higher temperature. It means that the anisotropy of the AZ31 decreases at higher temperature.

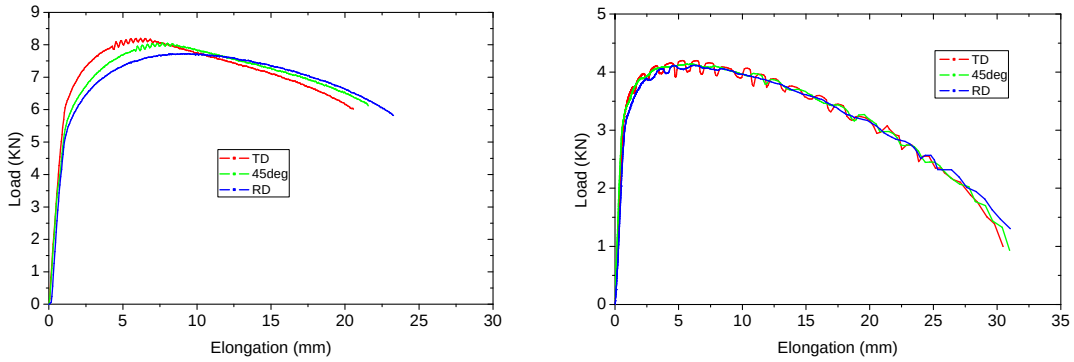


(a) T=100$^0$C, $\dot{\varepsilon}$ =0.01s$^{-1}$ (b) T=200$^0$C, $\dot{\varepsilon}$ =0.01s$^{-1}$

Fig.13. Load-elongation curves of different directions at different temperature

Actually, other researchers also make the same study. For instance, Kaiser *et al.* [9] studied intensively the anisotropic properties of magnesium sheet AZ31 and investigated the texture evolution at various temperatures. It is concluded that AZ31 sheet shows vertical and planar anisotropy at room temperature, while it shows a declining yielding anisotropy with increasing temperature, and anisotropy is not observed anymore at 250$^0$C. In the benchmark of 8th international NUMISHEET conference [10], it gives the same conclusion from the benchmark description. The *R*-value data from uniaxial tensile test are shown in the following table (Table.3). It is obviously shown that the anisotropy decreases with increasing temperature. As explanation in the micro aspect, more slip planes are activated at higher temperature that makes the material easier to deform and perform less anisotropy.

Table.3. R-value data from Uniaxial tensile test [10]

| Test direction | Temperature ($^0$C) | | | | | |
|---|---|---|---|---|---|---|
| | RT | 100 | 150 | 200 | 250 | 300 |
| 0 | 1.347 | 2.006 | 1.291 | 1.621 | 1.344 | 1.374 |
| 45 | 2.793 | 2.412 | 1.976 | 2.118 | 1.532 | 1.477 |
| 90 | 4.109 | 4.406 | 3.189 | 2.672 | 1.799 | 1.881 |
| Mean | 2.76 | 2.809 | 2.018 | 2.132 | 1.552 | 1.552 |

Since the material forming performed mainly in the higher temperature, the anisotropy of AZ31 magnesium alloy sheet could be neglected, although it still existed, especially at elevated temperature. So, the anisotropic property is not considered in this project.

# 3. Constitutive equation identification

The constitutive equation can be described by stress strain data from tensile experiment. In this project, two constitutive equations are analyzed by power law and Gavrus law model.

The related parameters are obtained by fitting the equation with the experimental data. The genetic algorithm has been used to obtain the global optimal fitting parameters. And the comparisons are performed between fitting curves and experimental curves.

## 3.1 Power law model

Firstly, the flow stress curves are analyzed by power law equation, which is the common formula for most metal materials [11]. At first approximation, as to analyze the relationship between process parameters with temperature, we can consider the constitutive equation which just includes strain hardening and strain rate to describe the AZ31 magnesium alloy stress and strain relationship at warm forming. The equation can be written as the function of temperature as follow:

$$\sigma = K(T)\varepsilon^{n(T)}\dot{\varepsilon}^{m(T)} \tag{3.2}$$

Where, $K$ is the strength coefficient, $n$ is the strain hardening exponent, and $m$ is the strain rate sensitivity exponent. This equation is widely used to describe the stress-strain relationship and it can well express the work hardening phenomenon by the strain hardening exponent ($n$-value) and the strain rate sensitivity exponent ($m$-value), which are the two important parameters to describe the deformation behavior of metal sheet.

From the experimental true stress- true strain curves, it can be shown that the values of stress under the uniform deformation stage are almost on a line, in which slope equal to the value of strain is hardening exponent. The $n$-value corresponding with the different temperatures and various strain rates can be obtained using following equation.

$$n = \frac{\partial \ln \sigma}{\partial \ln \varepsilon}\Big|_{\dot{\varepsilon},T} \tag{3.3}$$

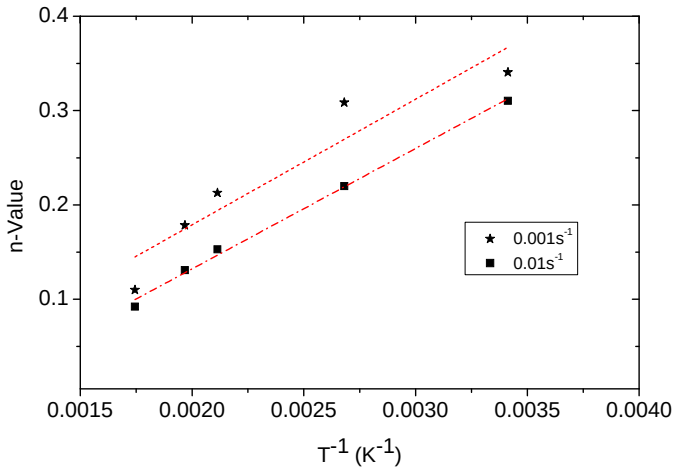


(a) n-value vs. reciprocal of temperature at various strain rates

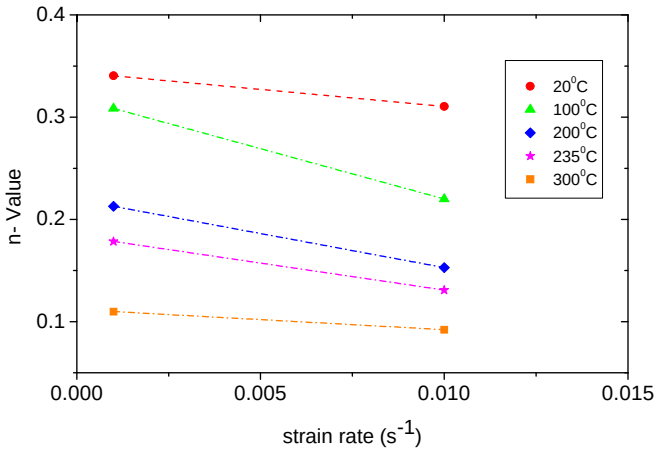


(b) n-value vs. strain rate at various temperatures

Fig.14. Relationship between n-value and reciprocal of temperature and strain rate

Fig.14 shows the relationships between the *n*-value and temperature at different strain rate. It can be seen that the slope of the polynomial fitting lines are nearly the same. So, the linear relationship is used between the n-value and the reciprocal of the temperature.

The same fitting method can be used to study *m*-value and *K*-value. The true stress-true strain shows the relationships between the stress and the strain rate for various strains. The linear relationship is also found between the *m*-value and the reciprocal of temperature. It can be obtained the *m*-value with temperature by computing the slope of the flow stress using following equation.

$$m = \frac{\partial \ln \sigma}{\partial \ln \dot{\varepsilon}}\Big|_{\varepsilon,T} \tag{3.4}$$

Similarly, the *K*-value is found that it is almost linear relationship with the reciprocal of temperature, and it is independent of the strain rate at each temperature. Fig.15 shows the relationship between process parameters with reciprocal of temperature.

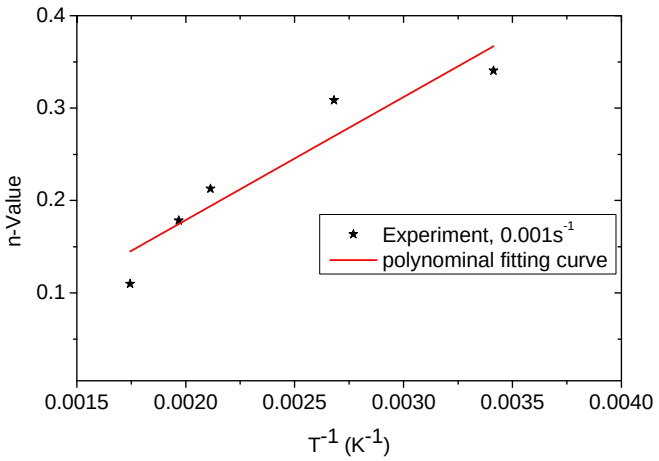


(a) *n*-value vs. reciprocal of temperature

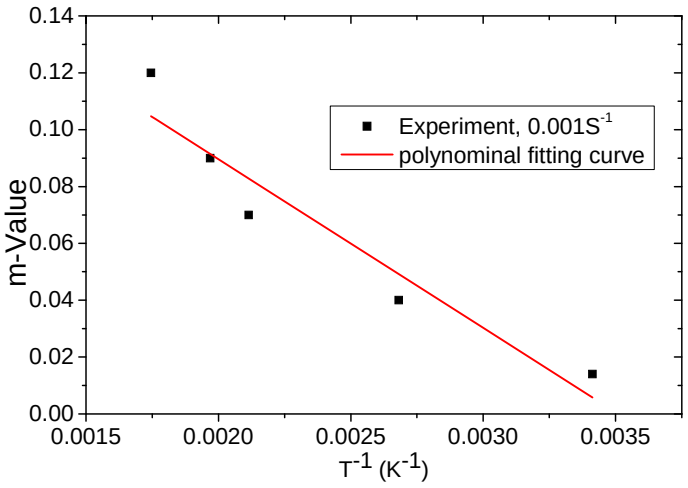


(b) *m*-value vs. reciprocal of temperature

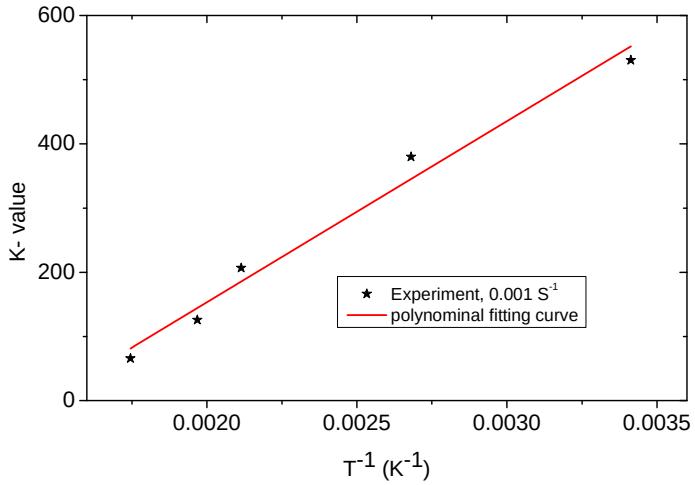


(c) *K*-value vs. reciprocal of temperature

Fig.15. Relationship between sensitivity parameters and reciprocal of temperatures

Using classical fitting procedure, the linear evolution of $n$, $m$ and $K$ value with the reciprocal of temperature have been obtained. For simplicity, the parameter fitting equation is expressed as follows:

$$K = k_1 / T + k_2 \tag{3.5}$$

$$n = n_1 / T + n_2 \tag{3.6}$$

$$m = m_1 / T + m_2 \tag{3.7}$$

Finally, the optimal fitting parameters for power law type constitutive equation have been obtained and shown in Table.4.

Table.4. Fitting parameters for power law constitutive equation

| $k_1$ (MPa * K*s) | $k_2$ (MPa*s) | $n_1$ (K) | $n_2$ | $m_1$ (K) | $m_2$ |
|---|---|---|---|---|---|
| 2.820E10$^5$ | -411 | 130.400 | -0.105 | -59.304 | 0.208 |

Fig.16 shows the curves of strain-stress obtained from the experiment and the calculation according to the present formula. It is seen that the calculated results can fit well with the experimental result during the strain hardening stage. But AZ31 magnesium alloy sheet exhibits softening property, especially at high temperature. The power law type equation is not sufficient to describe the material behavior. This deviation is mainly due to the lack of softening item in the constitutive equation.

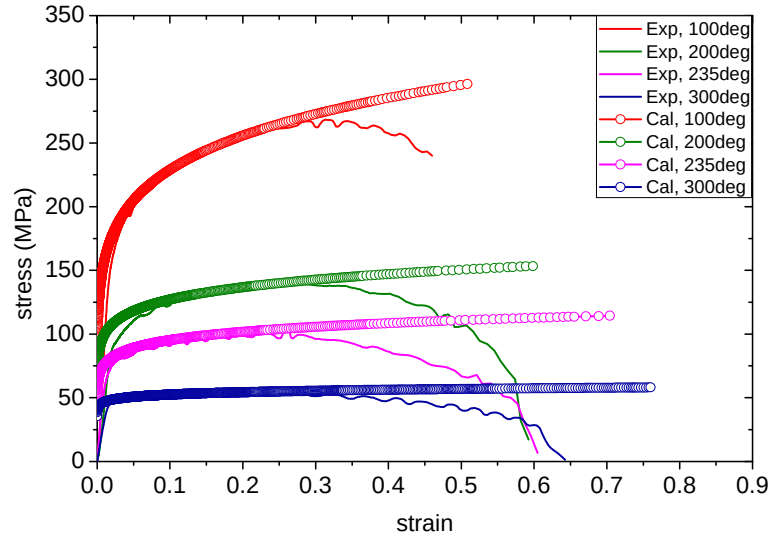


(a) $\dot{\varepsilon}$ =0.01s$^{-1}$

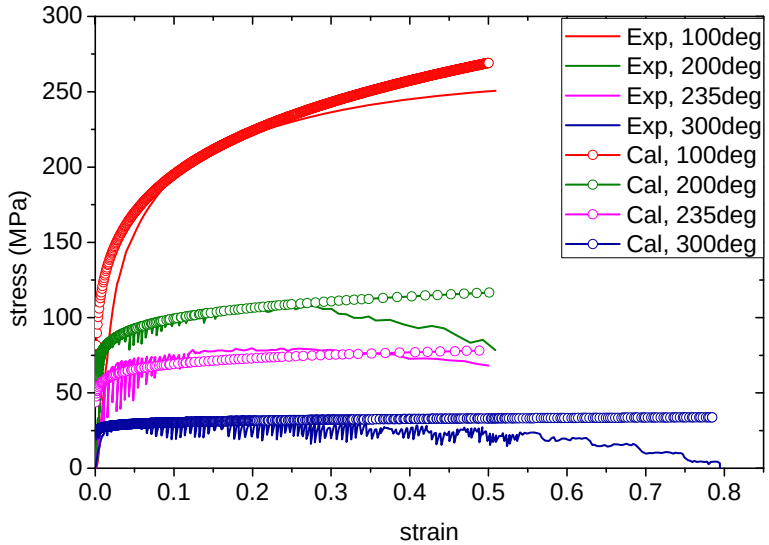


(b) $\dot{\varepsilon}$ =0.001s$^{-1}$

Fig.16. Comparison between calculated and measured flow curves

## 3.2 Gavrus law model

It can be seen that the power law model can only describe the flow stress curves of AZ31 magnesium alloy sheet at strain hardening stage. The Gavrus Law includes a softening item, and it is an available method to describe the softening phenomenon in AZ31 sheet metal forming [12]. The equation is expressed as follows:

$$\overline{\sigma} = K\dot{\overline{\varepsilon}}^{m} \tag{3.8}$$

$$K = (1-W)K_{ecr} + W \cdot K_{sat} \tag{3.9}$$

Where, $K_{ecr}$ is strain hardening function, $K_{sat}$ is saturation function, $W$ is softening function.

For the AZ31 magnesium alloy sheet, it has been shown clear softening characteristic, but the saturation stage is not evident. So, the saturation function $K_{sat}$ has not been considered. The power law has been used to describe the strain hardening. The softening phenomenon is different at various temperatures, so the polynomial expressions which depend on temperature have been used in softening function. The strain hardening and softening equation are expressed as follows:

$$K_{ecr} = k(\varepsilon + \varepsilon_0)^n \cdot \exp(\beta / T) \tag{3.10}$$

$$W = 1 - \exp(-r \times \overline{\varepsilon}) \tag{3.11}$$

$$r = r_0 + r_1 \times T \tag{3.12}$$

Finally, the Gavrus law is explicitly expressed as follow:

$$\overline{\sigma} = k(\overline{\varepsilon} + \varepsilon_0)^n \cdot \exp(\beta / T) \cdot \exp\left[-(r_0 + r_1 \times T) \times \overline{\varepsilon}\right] \cdot \dot{\overline{\varepsilon}}^{(m_0 + m_1 \times T)} \tag{3.13}$$

In order to get a proper global constitutive equation to describe the flow behavior of AZ31 magnesium alloy sheet at various temperatures and strain rate, the genetic algorithm (GA) in Matlab toolbox® has been used. The objective function is following.

$$O(f) = \frac{\sum_{i}^{n} (\sigma_i^{\exp} - \sigma_i^{cal})^2}{\sum_{i}^{n} (\sigma_i^{\exp})^2} \tag{3.14}$$

Where, $n$ is the number of data point, $\sigma_i$ is the stress at the data point "$i$". The genetic algorithm is sensitive to the initial value of parameters, the parameter value ranges have been

set by fitting the individual stress-strain curves, and then getting the maximum and minimum value of parameters. Finally, according the Gavrus law and the setting objective function, the global optimal fitting parameters have been obtained (Table 5).

Table 5. Optimal fitting parameters for Gavrus constitutive equation

| Parameters | $k$ (MPa*s) | $n$ | $\beta$ (K) | $r_0$ | $r_1$ ($K^{-1}$) | $m_0$ | $m_1$ ($K^{-1}$) | $\varepsilon_0$ |
|---|---|---|---|---|---|---|---|---|
| Optimal evaluation | 235.150 | 0.138 | 86.343 | -0.999 | 0.011 | 0.062 | 0.00043 | 1.00E-06 |

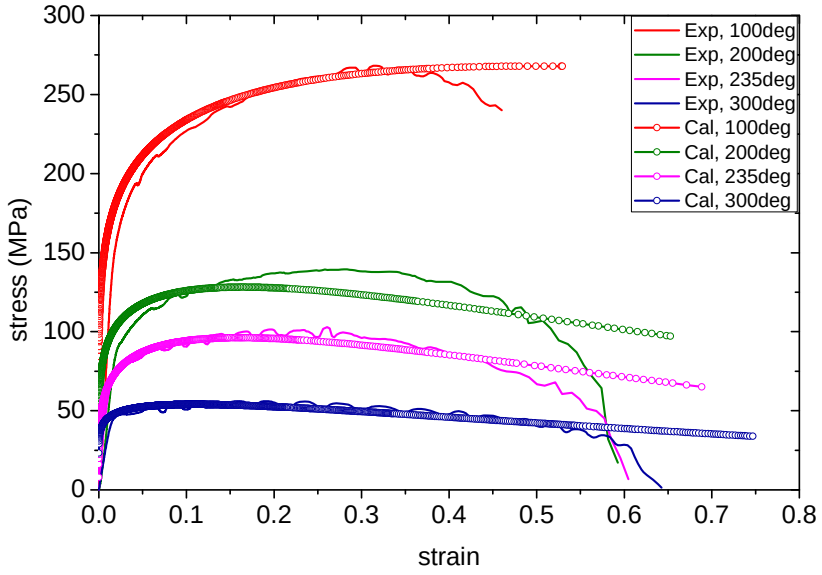


(a) $\dot{\varepsilon}$ =0.01$s^{-1}$

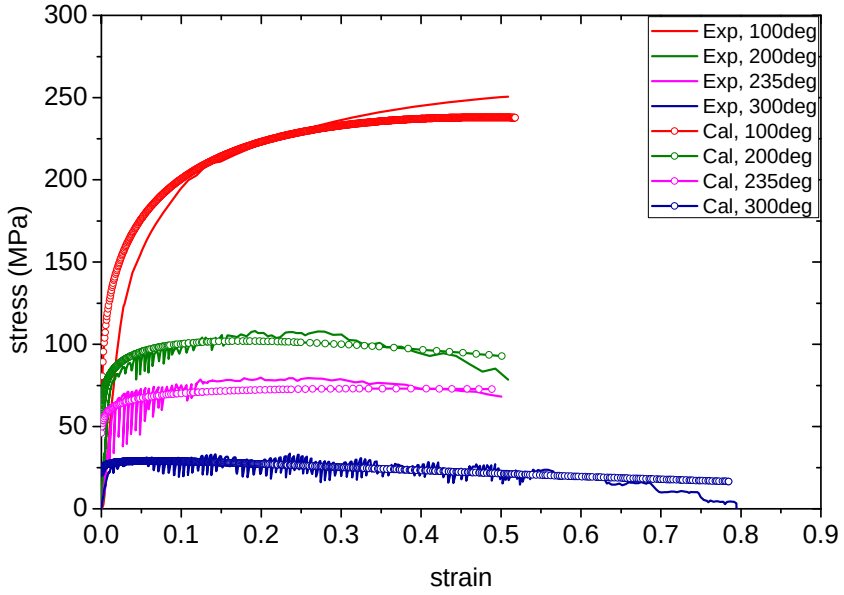


(b) $\dot{\varepsilon}$ =0.001$s^{-1}$

Fig.17. Comparison between calculated and experimental flow curves at various temperatures.

The comparison between calculated and experimental flow curves at various temperatures has been shown in Fig.17. It can be seen that the constitutive equation can describe correctly the flow properties of AZ31, especially the softening behaviors. From the optimal fitting equation, the sensitivity of process parameters can be analyzed. The choice of this law has undoubtedly improved the modeling of AZ31 magnesium alloy, but it is clear that there is still some dissatisfaction, especially during low strain rate. It is necessary to improve constitutive equation in the future work. One possible way is a finer coupling model taking into account the evolution of microstructure.

# 4. Conclusion

In this chapter, the thermal ductility of AZ31 magnesium alloy has been deeply studied by warm tensile test in various temperature and strain rate. The analysis results show that the ductility of AZ31 magnesium alloy has been improved dramatically with temperature increasing and strain rate decreasing, the hardening phenomenon is visible at lower temperature, the softening become more and more obvious with temperature increasing. Meanwhile, three kinds of specimens with respect to rolling direction are used to study material anisotropy, but the experiments indicate that anisotropy apparently decrease with temperature increasing, especially over $200^0$C. This conclusion has also been proved in publications. So, the anisotropy is not considered in this project.

In addition, the constitutive equations have also been identified with stress and strain data from warm tensile test. Two kinds of constitutive model are used in this project, i.e., power law and Gavrus law. These two models are identified with mathematical fitting and compared with experiment stress strain curves. The comparisons demonstrate that power law can just fit well with experimental curves at the strain hardening stage. Gavrus law include strain hardening and softening item, the fitting have been performed by Matlab genetic algorithm (GA) toolbox, the details of identification program will be presented in annex. Finally, the global optimal fitting parameters have been identified, and the comparisons indicate the Gavrus law can fit well with experimental curves in softening stage but there are still discrepancies. Nevertheless, it is difficult to propose a global constitutive equation completely describing material property. Presently, the focused study is using coupling model which include the evolution of microstructure and macro parameters in constitutive equation.

# 5. References


[1] Z. Marciniak, J. L. Duncan, J. Hu. Mechanics of sheet metal forming. Butterworth-Heinemann, 2002.

[2] ARAMIS tutorials introduction. GOM mbH, Braunschweig, Germany, 2001.

[3] W. M. Lai, D. Rubin, E. Krempl. Introduction to Continuum Mechanics. Butterworth-Heinemann, 2009.

[4] R. Knockaert. Etude expérimentale et numérique de la localisation de la deformation lors de la mise en forme de produits minces, PhD thesis, Ecole des mines de paris, 2001.

[5] Web: www.instron.com. Instron 1341H tensile testing tutorials. Instron Tool Works Inc. 2001.

[6] ISO 6892-2. Metallic materials - Tensile testing - Part 2: Method of test at elevated temperature. ICS: 77.040.10, TC/SC: TC 164/SC 1, International Organization for Standardization, 2011.

[7] W. F. Hosford, R. Caddell. Metal Forming: Mechanics and Metallurgy. 3rd Edition, Cambridge University, 2007.

[8] M. A. Meyers, K. K. Chawla. Mechanical Behavior of Materials. Cambridge University, 2009.

[9] K. Kaiser, D. Letzig, J. Bohlen, A.Styczynski, C. Hartig, K. U. Kainer. Anisotropic Properties of Magnesium Sheet AZ31. Material Science Forum, Vols. 419-422 (2003), pp.315-320.

[10] Benchmark 2: Simulation of the Cross-shaped Cup Deep-drawing Process. The 8th Internatinal Conference and Workshop on Numerical Simulation of 3D Sheet Metal Forming Processes. Seoul, Korea. 21-26 August, 2011.

[11] Z. Gronostajski. The constitutive equations for FEM analysis. Journal of Materials Processing Technology, 106 (2000), pp. 40-44.

[12] A. Gavrus, E. Massoni, J. L. Chenot. An inverse analysis using a finite element model for identification of rheological parameters. Journal of Materials Processing Technology, 60 (1996), pp.447-454.

# Chapter 4 Thermal formability of AZ31 magnesium alloy

## Contents

# 1. Introduction

Formability is the ability of material to undergo plastic deformation without damage. The plastic deformation capacity of metallic materials is limited to a certain extent in industrial application [1, 2]. Magnesium alloy as the lightest structural material is widely used in industry. However, because of its Hexagonal Closed-Packed (HCP) crystal structure, magnesium alloy shows low ductility at room temperature and require thermal activation to increase their formability. For this reason, magnesium alloy sheets are usually formed at temperatures ranging from 150 to 300°C [3]. Compared with several others industrial solutions, warm stamping of magnesium alloy comes out as a quite challenging process which is increasingly used for industrial applications and intensive research conducted to support this growth [4].

The warm stamping is a complex process because it relies on high number of parameters. Hora *et al*. [5] shows a list of parameters which play an important role in the stamping process. Most of the analysis study rheology, tribology, metallurgy and thermal aspects, etc [6, 7]. While the ductility and formability for the warm stamping process has not yet been investigated intensively so far. This task is challenging due to the high number of process variables, the thermo-mechanical and metallurgical interactions and their influence on the sheet formability [8, 9].

Actually, the formability investigation can be divided into 3 steps, i.e., experimental set-up development, critical strain determination, and experimental FLC validation. It requires both experimental tests and advanced numerical simulation tools. In order to determine the formability and the FLC (forming limit curves) in test configuration, several experimental tests have been developed and standardized. Nowadays, two main tests are largely used to analyse the formability of material, i.e., the Nakazima test and the Marciniak test. Nakazima *et al*. [10] developed a test based on the deformation of the blank by a hemispherical punch with a draw bead which is used to control the sliding motion of the blank. In 1973, Marciniak *et al*. [11] presented a relatively novel test. In this test, draw bead is also used but the punch has a hollowed cylindrical shape. Furthermore, a specific design is defined, where one additional drilled metal sheet called driving blank is used to support the punch load and force an expansion strain at the centre of the blank. The selected set-up has to allow varying strain paths in order to get fracture in different strain and strain history configuration, from the uniaxial tensile test to the pure bi-expansion. In most tests, the strain path change can be obtained for various specimen geometries. Nevertheless, the strain path depends on the blank

width and the friction coefficient between the blank and punch for the Nakazima tests. In addition, the author shows clearly how to construct a FLC from Nakazima tests in the literature [12]. This method is still used at present.

In this project, the formability of AZ31 magnesium alloy is studied comprehensively. The warm Nakazima experiments with hemisphere punch have been performed at various temperatures. The ARAMIS© strain measurement system has been used to obtain principal forming limit strains. The Forming Limit Diagram (FLD) is obtained by the critical point on the specimen surface at various temperatures. And the last, the influence parameters in experiments have been analyzed such as temperature, punch velocity, blank shape and lubricants, etc.

# 2. Nakazima warm stamping test

It is known that the Nakazima and the Marciniak tests are two common experimental tests which provide information on formability of sheet material. The main difference between these tests is the shape of the punch which is hemispherical and flat respectively. In this project, the Nakazima set-up has been initially selected because Nakazima test does not need any driving blank and it is much simpler to perform than Marciniak test.

## 2.1 Nakazima test set-up

The whole Nakazima set-up is made of four parts, i.e., a blank, a hemispherical punch, a die, a blank-holder with drawbead which prevent any sliding motion (Fig.1). In addition, a furnace has been installed close to the press to make sure that the sheet can be transferred easy into the stamping device. The pyrometer is used to measure each part temperature. The Fig.2 has specifically illustrated the procedure of Nakazima test forming. At the first, each part is in the waiting state, the blank is put on the die. And then, the blank holder goes down to maintain the blank on the die when the blank contact with the die. Meanwhile, pneumatic cylinders control and command the motion of the blank-holder. The last step is the stamping. The punch moves down with the motion of setup, and the blank is simultaneously deformed by the punch. This is the brief procedure of the warm Nakazima tests.

The selected set-up has to allow varying strain paths in order to get fracture in different strain states and strain history configurations from uniaxial tensile mode to pure bi-expansion. This fact will allow to obtain critical strain points for various strain paths and for given stamping conditions. In most tests, the strain path change can be obtained by varying the

specimen geometry. However, the strain path can sometimes depend not only on the blank width but also on the friction coefficient between the blank and the punch in Nakazima tests. Generally, varying the blank width and using lubricant allow to get fracture in tensile and expansion modes.

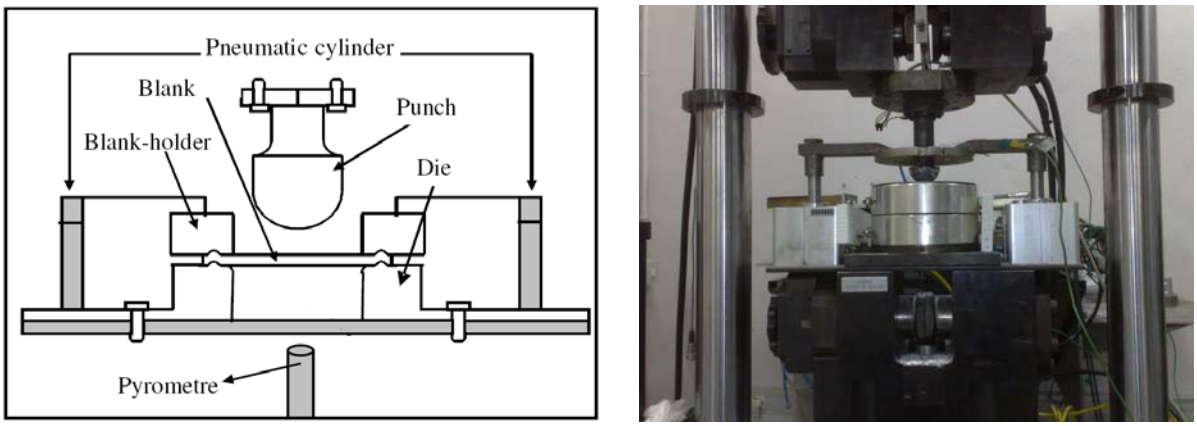


(a) Experimental Set-up

(b) Temperature controller

Fig.1. set-up for Nakazima tests (a) and the temperature controller (b)

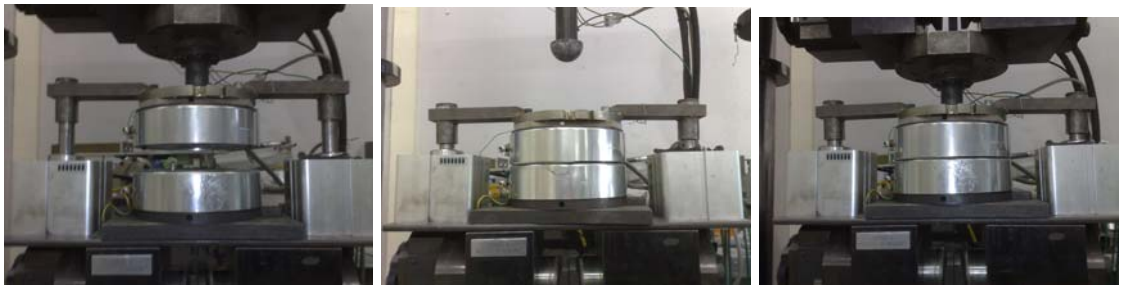

Step 0: waiting Step 1: holding-blank Step 2: stamping

Fig.2. The procedure of the Nakazima stamping tests

In these Nakazima tests, the AZ31 magnesium alloy sheet with 1.2mm thickness is used for the experiment, which is same with the material used in tensile tests. The Nakazima warm

stamping test is developed with an isothermal process in which the tools are the same temperature. The test specimens are prepared at CEMEF laboratory and the experiment device is tension-compression hydraulic testing machine Dartec®, in which maximum punch velocity is 300mm/s and maximum punch load is 300kN. The main advantages of this set-up are to support very high temperature, and allow a rapid insertion of the warm blank into the press (between the die and the blank holder). Moreover, the temperature controller is verified for reliability and keep temperature controlling precisely

## 2.2 Strain path and optical measurement

This test technique requires the use of different specimen geometries and lubrication condition to generate all possible strain states and stresses. The specimen geometry is designed by standard NF EN ISO 12004 [13], and the dimension of specimen is summarized in Fig.3. Each sample represented one specific strain path on the FLD [13]. The test specimens are distributed from uniaxial tension to biaxial expansion approximately. Furthermore, two lubricants have been used in order to get better friction condition in this project, i.e., $MoS_2$ and Boron Nitride (BN). $MoS_2$ is a common dry lubricant using in industry. The sliding friction tests of $MoS_2$ at low loads give friction coefficient values less than 0.1 [8]. BN is also a good lubricant at both low and high temperatures. The advantage of BN over graphite is that its lubricity does not require water or gas molecules trapped between the layers. These two lubricants have test prior to start forming, and the comparison will be presented in the result analysis [8].

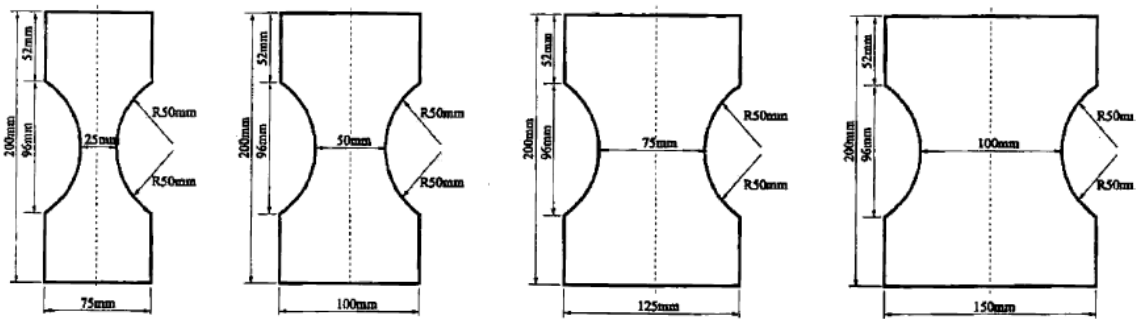


Fig.3. Various Nakazima test specimen geometries

The specific modeling layout of Nakazima test has been shown in Fig.4. One quarter of the blank is modeled due to symmetry boundary condition. A rectangular sheet specimen is clamped firmly, and stretched by a semi-spherical headed punch of 60mm diameter. In order to prevent wrinkle and keep the sheet surface smooth, the drawbead have been used in the

blank holder zone. The blank holder play an important role in stamping process, the blank holder force should keep the material flowing smoothly and make the blank and die contacting well [14]. In this project, the constant blank holder force has been used, and the proper specimens have been obtained after tests.

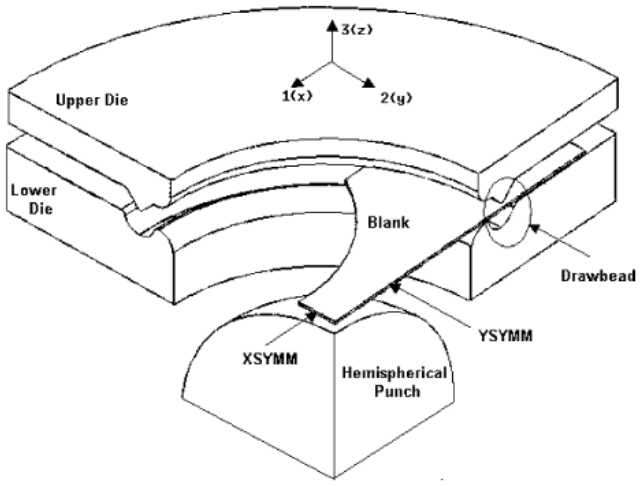


Fig.4. The modeling layout of Nakazima test [14]

The limit strains can be obtained from 3D deformation measurements system. With technology development, the optical measurement using an accurate and contactless method has demonstrated their ability to provide three dimensional strain measurement. Generally, two kinds of optical strain measurement system, i.e., ASAME® (automated strain analysis and measurement environment) and ARAMIS® are mainly used in industry. Both of software are used by production and research engineers to analyze formability issues for industrial applications. The measurement principle of ARAMIS has been presented in previous chapter. And these two kinds measurement method base on similar principle but the difference is the style of pattern which is the uniform and non-uniform pattern respectively. Generally, ASAME and ARAMIS can provided very quickly non-contact reliable strain measurement. These software also allow to determine the strain along a section and to sketch the strain distribution onto the forming limit diagram. It is then possible to compare the strain fields of a lot of specimens and to determine the forming limit curve. In the application, different grid shapes by these two systems can be selected based on the different measurement requirements (Fig.5). However, a straightforward contrast of the grids is required basically to carry out a relevant and accurate correlation [15].

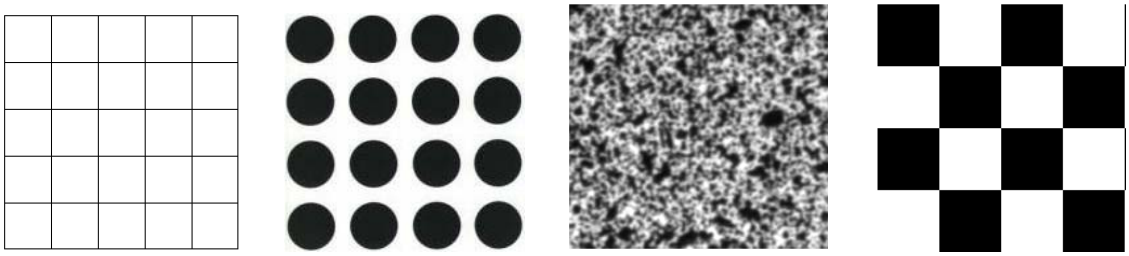

Square grid Circle grid Speckle grid Checkerboard grid

Fig.5. Different patterns used by optical measurement systems

As discussed in previous chapter, the grid quality is obviously crucial for an accurate limit strain measurement. Different grid marking methods are available such as painting or electro-etching methods. Unfortunately, the warm stamping test during high temperature can modify the grid. For high temperature tests, the painted pattern can show several speckle disappeared area and the electro-etched grid can evolve to an undistinguishable contrast. One challenge is to develop a technique allowing a relevant grid preservation to perform the strain distribution measurements. In this project, ARAMIS system has been used to measure the critical strains, the operate procedure is shown in Fig.6. And the patterns are made by electro-etching method which has better performance at high temperature. Several specimens for each test have been carried out to avoid strain measurement difficulty. Finally, the best test specimens are analyzed in ARAMIS system.

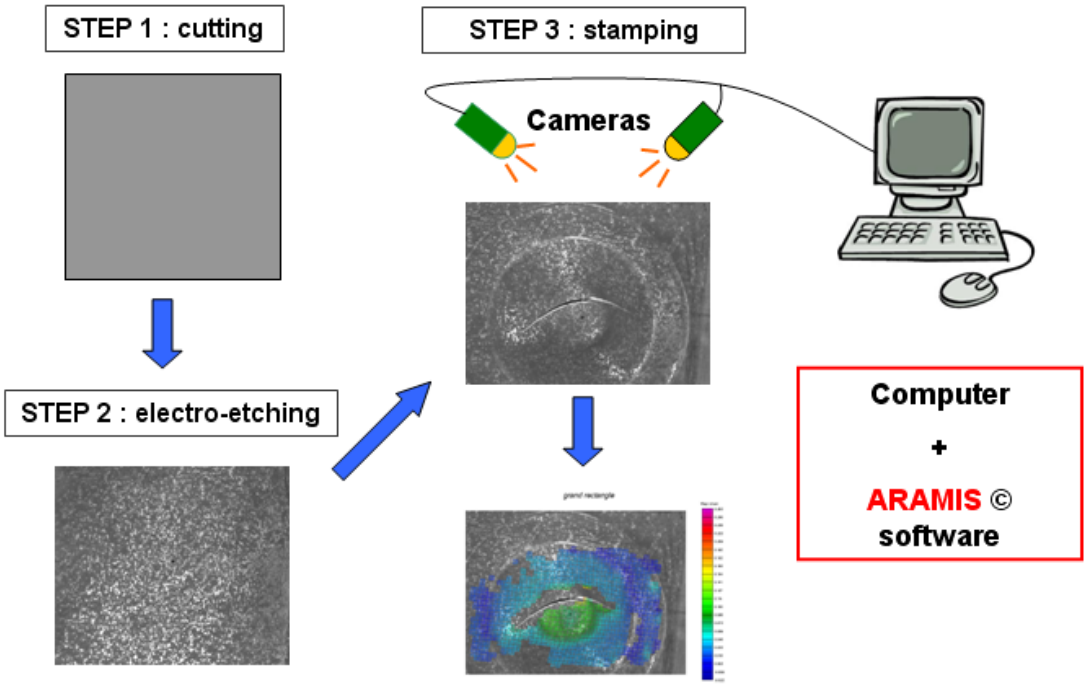


Fig.6. The ARAMIS system operate procedure

# 3. The result analysis

## 3.1 Limit strain measurements

The Nakazima experiments have been carried out and then investigated intensively in this project. Three types of stamped blanks can be obtained from tests: safe, with strain localization and fracture (Fig.7). Generally, for a low punch stroke, the blank shows no critical damage. For a higher punch stroke, strain localization may occur on the blank surface. Once the maximum punch stroke is reached, the necking grows until the creation of fracture which spreads over the punch radius area [16].

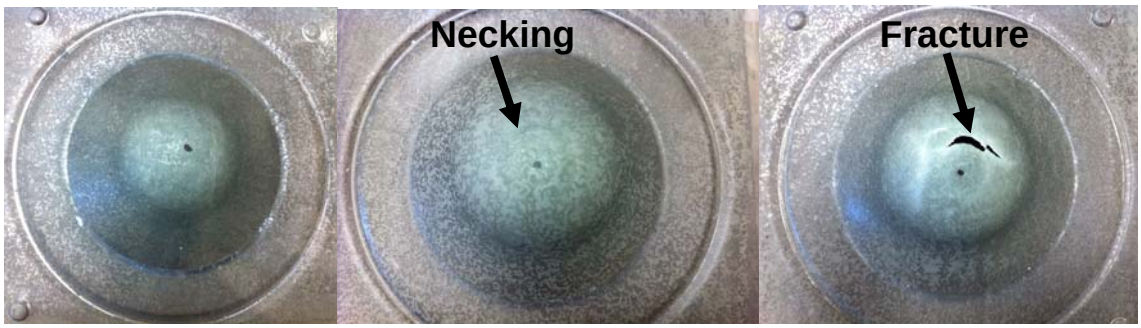


Fig.7. Nakazima hot stamped blanks in various conditions

Fig.8 shows the various deformed specimens after Nakazima tests. The factor $\beta$ which is the proportion of sheet width and length is introduced into experiment. These specimens represent various strain paths. Ultimately, the specimens were deformed at different degree for each specimen, in which appeared necking or fracture phenomenon. In addition, the fracture and necking phenomenon often happen in the punch radius zone.

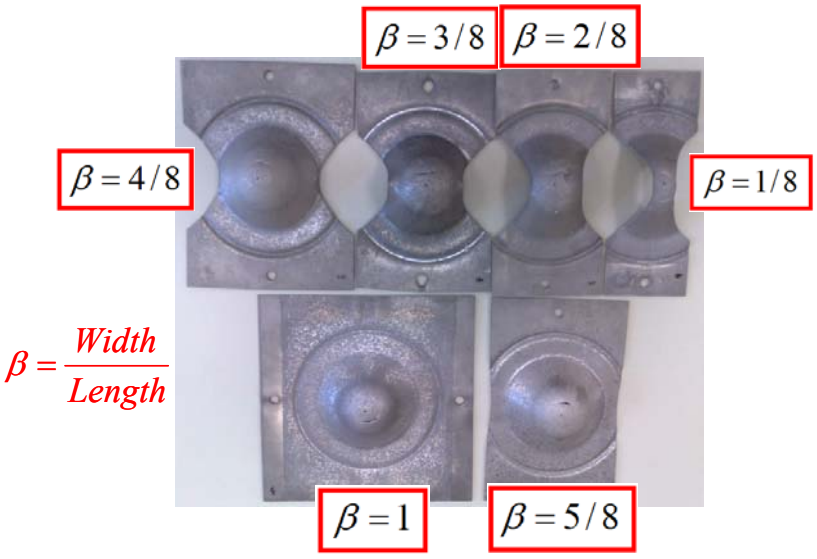


Fig.8. Specimens after Nakazima tests

The simple schematic diagram of ARAMIS measurement system set-up in laboratory is shown in Fig.9. The light compensation system is also often used in the process to adjust pattern recognition. Finally, the limit strain calculation results are shown in computer directly.

Fig.9. The ARAMIS measurement system set-up in laboratory

As for ARAMIS measurement systems, grid patterns are initially etched on the blank and allow determining the strain distribution by calculation using pattern recognition systems. The blank is cleaned firstly with an ethanol-based solution. Then an electro-etching device has been used to mark the blank. As it is known that the grids play an important role for strain measurement system. Unfortunately, for hot forming process, the grid pattern is often damaged during stamping tests due to heating and large deformation. It is necessary to prepare very high quality specimen for strain measurement system. It is shown the clear sheet image before and after stamping test in Fig.10. The calculation is performed better when the specimen pattern distribute clearly on sheet surface. For the bad pattern specimen, the calculation will be difficult and slow, because the interpolation is used for the point which the measurement system can not recognize. For some area where the pattern contrast is not clear enough, even it can not be calculated by ARAMIS (Fig.11). Nevertheless, the specimen with best calculation has been selected in this project.

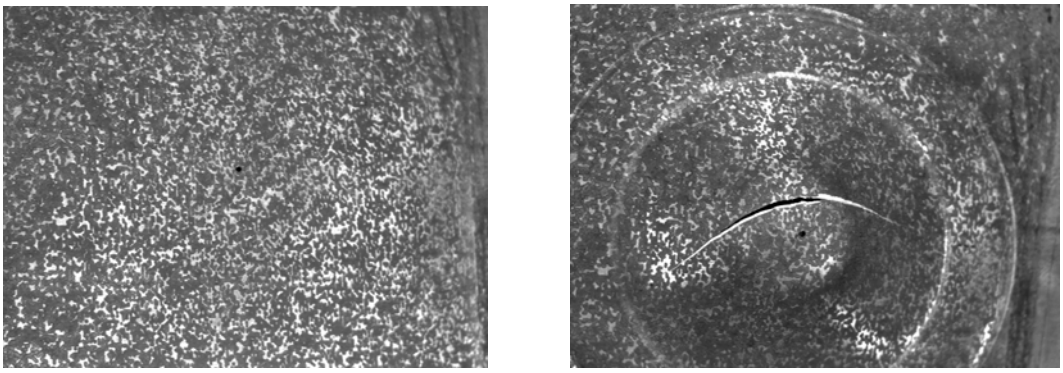

(a) Initial image (b) Deformed image

Fig.10. Test blank before and after deformation

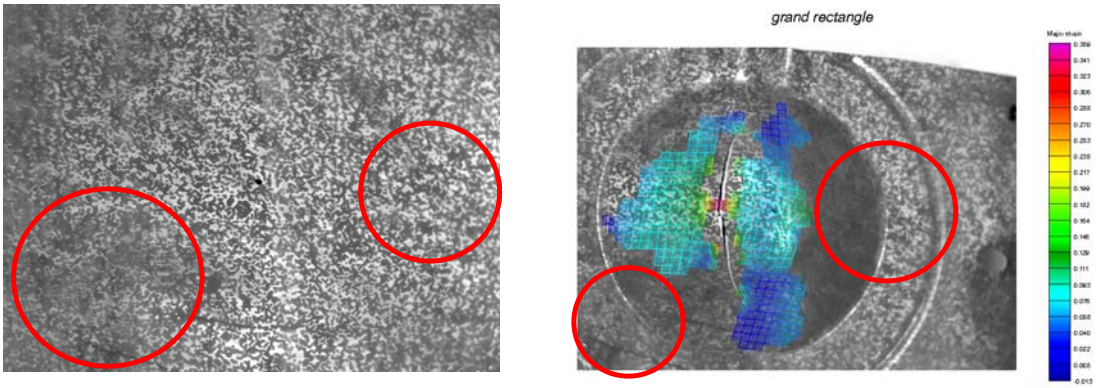


Fig.11. The calculation with bad grid pattern

From the warm Nakazima test, the limit strains distribution can be analyzed by the pattern recognition module in ARAMIS. The limit strains in length and width direction, i.e., major strain and minor strain ( $\varepsilon_1$ and $\varepsilon_2$ ) can be detected directly from ARAMIS system, and then the thinning value ( $\varepsilon_3$ ) can be determined considering volume conservation. Fig.12 shows an example of ARAMIS strain contour in $100^0$C, it is clear to show strain distribution on the sheet surface.

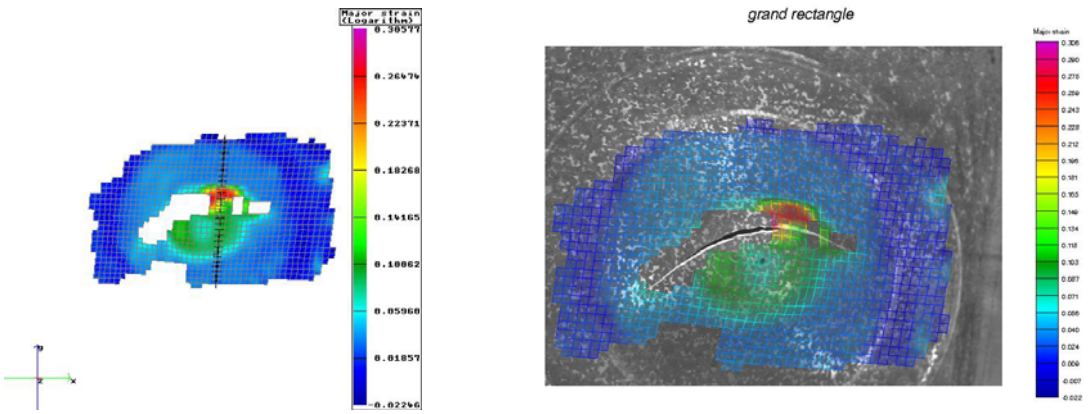


Fig.12. Strain distribution measured by ARAMIS ($100^0$C)

In addition, strains in a tangent plane or along a blank section can be plotted in ARAMIS by automatic calculation. Fig.13 shows an example of the strain measurement in sheet diagonal section with a safe specimen at $100^0$C. It is obvious to show that the major strain in the punch radius area is higher than others, so this is the most dangerous zone in the test.

The comparison of major strain (in-plane), minor strain and thickness strains along the section are analyzed in Fig.14. It is obvious to show strain localization in the punch radius area. This region belongs to the free blank zone where only heat exchange with the air by convection occurs. In the localized necking region, the major strain and minor strain are positive, it means that the punch radius region is indeed in an expansion state. This trend is also revealed in the forming limit diagram. It is distinct to show the strain distribution in FLD from ARAMIS. But in order to study the formability, it is necessary to analyze the forming limits for different process condition [17].

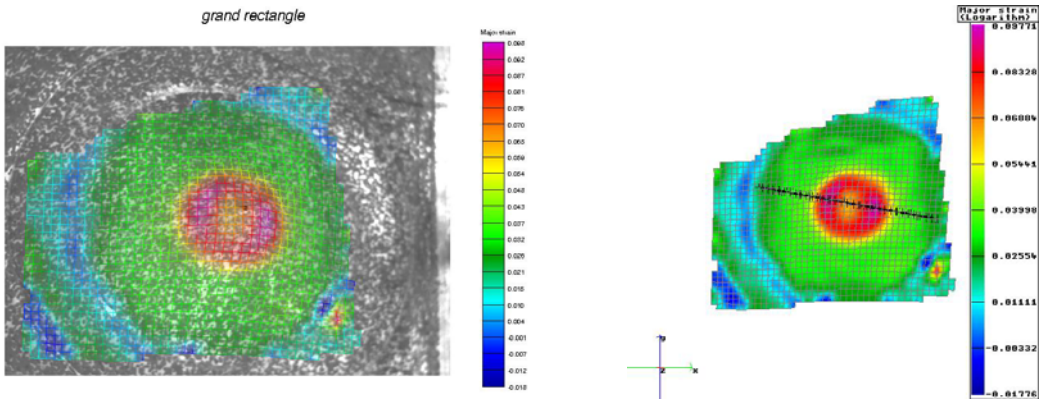


Fig.13. The strain measurements in blank diagonal section ($100^0$C, safe specimen)

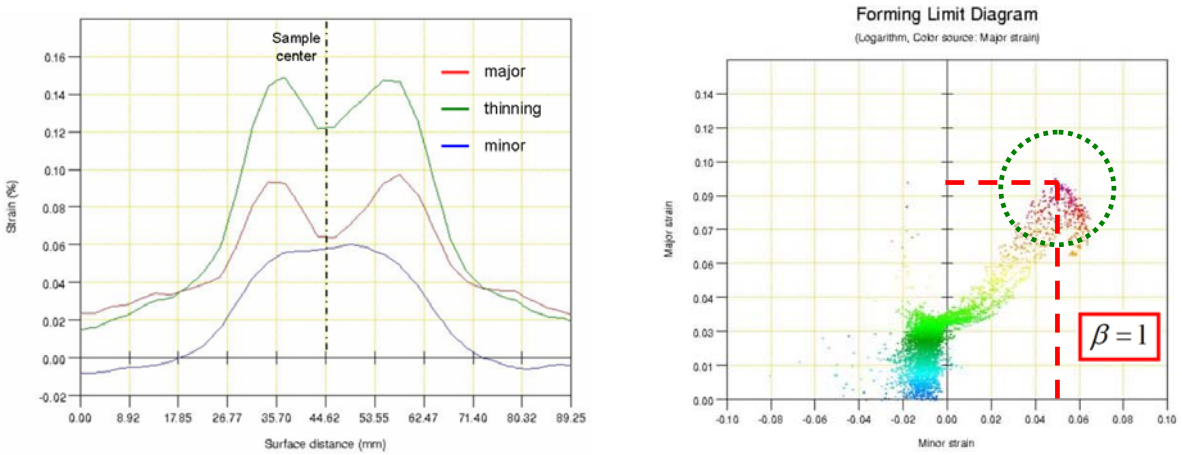


Fig.14. Major and thinning strains and Forming Limit Diagram (FLD) given by ARAMIS ($100^0$C, safe specimen)

## 3.2 The forming limit curve identification

It has been shown that the localized necking of AZ31 follows closely the diffused necking at room temperature from stress-strain curves. But the plasticity is improved obviously with temperature increasing, the plastic deformation can still occur after diffused necking at high temperature, and then up to localized necking. So, generally, the forming limits diagram has three types, i.e., the safe FLD, the necking FLD and the broken FLD [16].

Once the Nakazima tests have been carried out, the most difficulty is to determine the critical strain values to construct the forming limit diagram. There are some available techniques for the determination of FLD at room temperature at present. However, the reference technique and corresponding standards are still insufficient for hot forming experiment. For the hot stamping experiment, no testing procedure is available to refer in the literature. The most common used methods have been proposed by Veerman, Bragard and Hecker, and the Bragard's method is used particularly among these methods [16]. The traditional identification method is quiet objectives since it is quite dependant on the user's interpretation to measure the critical value of fracture point. In this project, the forming limit curve have identified base on ARAMIS strain measurement system and referred the above method. Firstly, the principal strain value evolution along a section normal to the fracture can be obtained from ARAMIS system. And then the zone where the strain distribution will not be considered has to be defined around the fracture. Thirdly, the principal strain values are calculated by extrapolation based on the strain derivative with corresponding position. The critical strain value ($FLC_0$) is calculated with the slope of strain equal zero.

Based on this method, the broken FLD of AZ31 obtained from warm Nakazima test has been shown in the Fig.15. Each strain path has been measured and the overlaid strain image has shown in the diagram. Unfortunately, as for the previous mention, some measured strain is limited for warm Nakazima experiment because the Aramis pattern is difficult to be recognized completely after test. However, the tendency is very clear that the higher forming limit curves with higher temperature from the images. It means the formability is better in higher temperature. The same conclusions have been made in other publications [18-20].

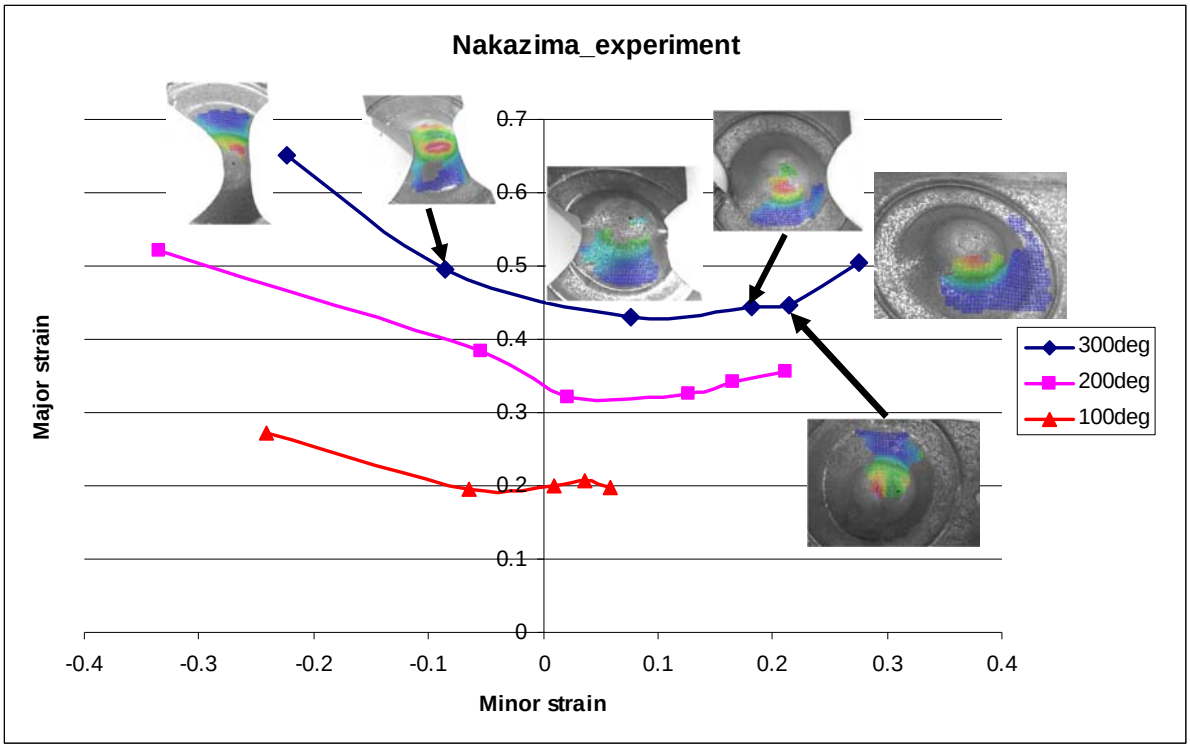


Fig.15. Broken FLD identified by Nakazima experiments

In the forming limit tests, there are different phenomena under various strain paths. The necking and fracture location is also varied from tension test state to bi-expansion test state. Fig.16 shows the comparison between isotropic strain path and real experimental strain path in uniaxial tension and biaxial expansion stress state. It is illustrated obviously that the strain paths of experimental FLC have discrepancies with theoretical FLC, because the strain measurement and lubricant is complicated in experiment. Another reason is that a sudden change of strain occurs after necking, this phenomenon is visible on the FLD images from ARAMIS. This changes led to result the experimental strain path is higher in the biaxial expansion state. It must be defined a certain safety margin if the broken FLD used in the actual application. The tensile tests have demonstrated that the AZ31 sheet still have some plasticity when necking occurs, especially at high temperature. Generally, the necking FLC is lower than the broken FLC in the forming limit diagram [18].

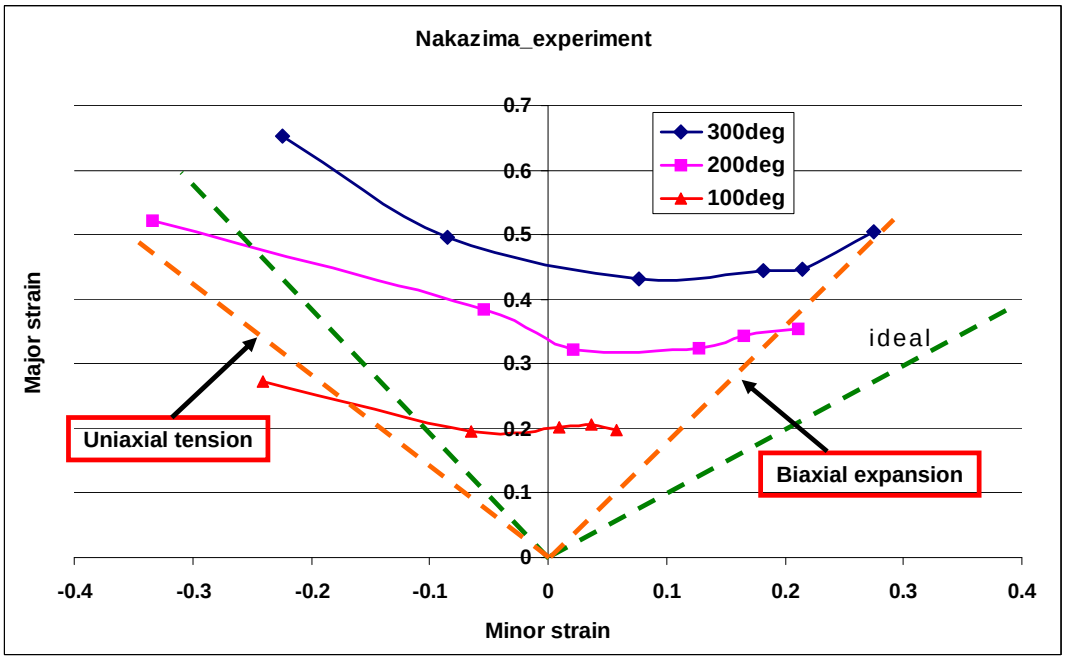


Fig.16. Comparison of isotropic strain path and real strain path

## 3.3 Sensitivity analysis of process parameters

It is known that sheet forming experiment is sensitive to the process parameters. The experimental determination of formability limits has to take into account several process characteristics in terms of temperature, visco-plastic behavior, heat transfer, strain path (blank shape) and friction, etc. These parameters can be changed by varying the initial temperature, punch velocity, lubricant and blank shape in order to analyze their respective influence on formability.

### 3.3.1 Temperature influence

It has been demonstrated that temperature plays an important role in the forming limits of magnesium sheet forming from FLD. Therefore, in order to investigate the temperature influence, warm stamping tests have been performed at various temperatures. Fig.17 shows the temperature influence with the load-stroke curves for two kind specimens which approximately represent the uniaxial tension and biaxial expansion state. In conclusion, the punch load decrease with the temperature increasing. This behavior has been shown clearly for both strain path, and the punch load is larger in the stretching state than the tension state. However, the decreased tendency of punch load with increased temperature is quite similar for both specimens.

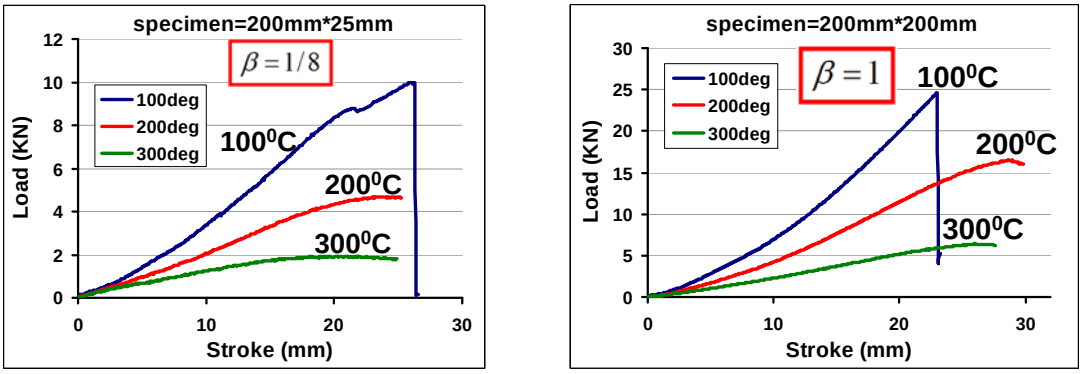


Fig.17. Load - stroke curve for two different specimens.

Fig.18 shows the temperature influence with the dome height for three kind specimens. The LDH (limit dome height)-temperature curves is shown differently and the LDH obtained with different specimens distribute disorderly at various temperatures. It is seen that the highest value of LDH is shown at 200$^0$C for the specimen in tension strain path, beyond which the LDH begins to decrease. This is probably because the resistance to flow localization of AZ31 alloy is considerably reduced by softening at temperature over 200$^0$C. For the stretching specimen, The LDH increase with temperature increasing, and the highest value of LDH obtained at 300$^0$C. This result is also concluded in the reference [19].

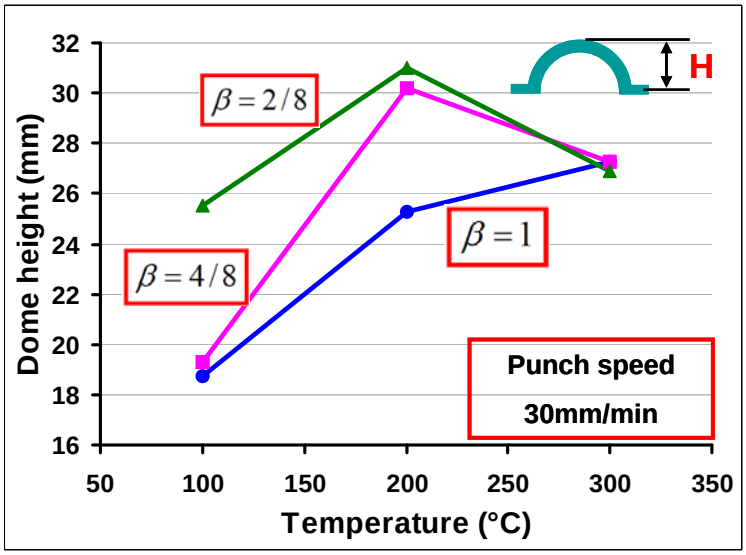


Fig.18. Test LDH of AZ31 sheet at various temperatures in three kind specimens.

### 3.3.2 Punch velocity influence

The influence of punch velocity is analyzed during warm stamping tests. Fig.19 shows the load-stroke curves at various punch velocity in 100$^0$C and 300$^0$C. As for the comparison, the punch load increase with the strain rate increasing for both temperature, but the

discrepancy is higher at 300$^0$C than 100$^0$C. It means the punch load is more sensitive for punch velocity at higher temperature. This conclusion is consistent with the tensile test result.

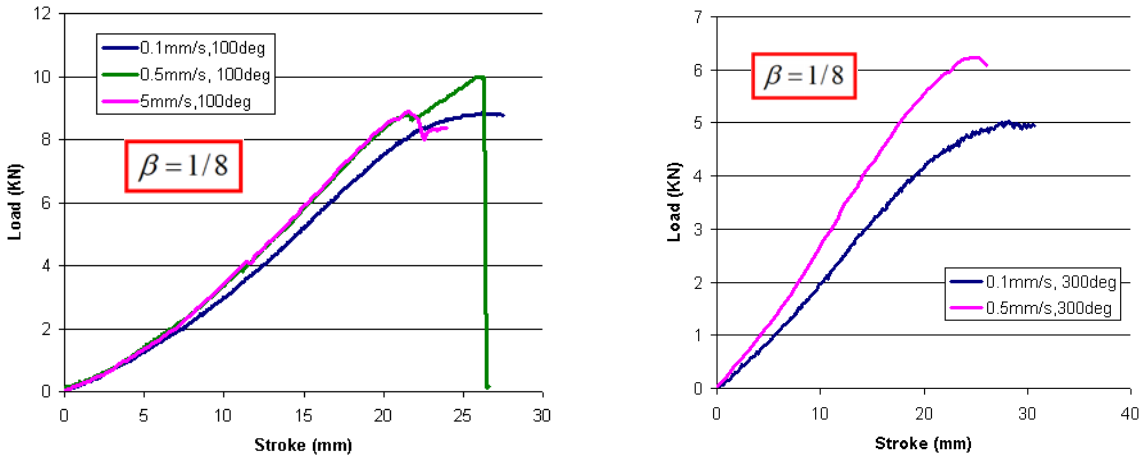


Fig.19. Load - stroke curves at various punch velocity.

In addition, the dome height is also compared in various punch velocity. Fig.20 shows the punch velocity influence with the velocity-dome height curves for tension state specimen. It is shown that the limit dome height decrease from 0.1mm/s to 0.5mm/s at 300$^0$C and 100$^0$C. But this trend is contrast at 200$^0$C, the limit dome height increase slightly from 0.1mm/s to 0.5mm/s. Overall, the formability of AZ31 is better at lower punch velocity. And the same conclusion have made in publication [20].

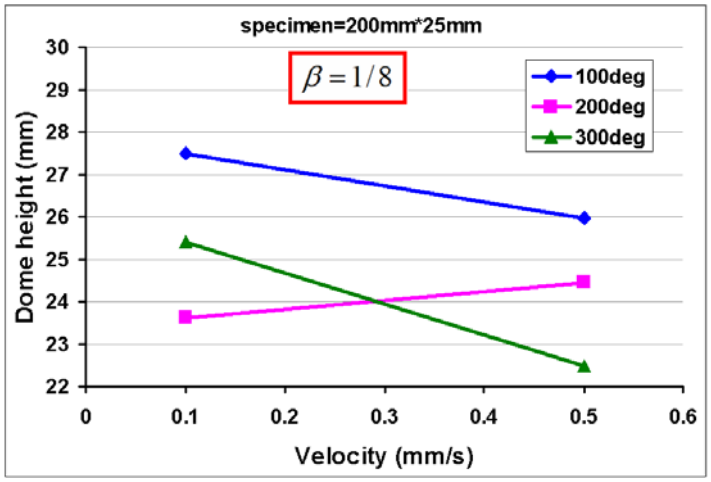


Fig.20. LDH of AZ31 sheet at various punch velocities.

### 3.3.3 Blank width and friction influence

Similarly, in order to investigate the blank width and friction influence, warm stamping tests have been performed for various blank widths. Fig.21 shows the load-stroke curves at 100$^0$C and 200$^0$C temperature in different blank width. It is clear that the punch load is higher

with higher blank width. And the punch load discrepancy is higher at 25mm than the other blank width for each stroke moment after 10mm in both temperature states. But this phenomenon does not happen at the small stroke moment, because the contact is fewer between blank and punch when the stroke is small. It is well known that the friction plays an important role in the stamping test, this is probably the reason to explain the discrepancy. The contact is fewest with the blank width of 25mm.

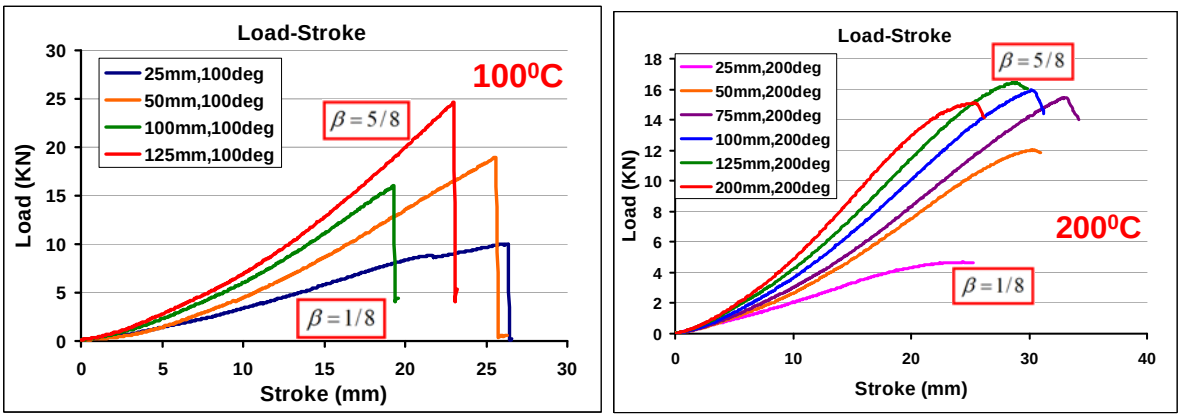


Fig.21. Load - stroke curve at various blank widths.

Furthermore, the dome height with different blank width have been compared at various temperature. The left side of Fig.22 shows the blank width influence on the specimen state by the blank width-limit dome height curves. The dome height distribute disorderly with blank width at various temperature. At $100^0$C, it decreased with the blank width increasing, but the limit dome height is lower when the blank width equal 100mm. At $200^0$C, the LDH increases and then decrease for various blank widths. At $300^0$C, the LDH increases slowly. However, it is also useful to compare the limit dome height with blank width at various deformation conditions.

At the last, the attempts have been performed to reduce friction between the blank and the punch, which is the most critical restricts for material flow during the stamping process. This is also the reason why several lubricants (BN and $MoS_2$) are then tested at various temperatures. And finally, it is found that the lubricant BN is better than $MoS_2$ by comparing the quality of stamping specimens (Fig.23). So, the Lubricant BN is selected in this project for all of specimens.

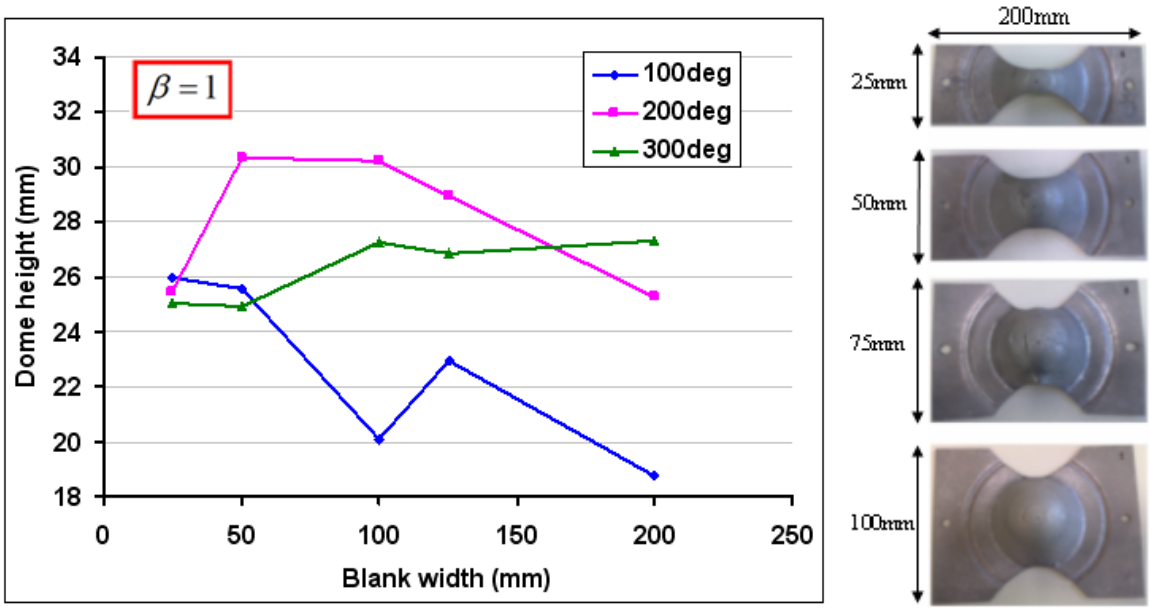


Fig.22. Nakazima tests blanks with different widths and dome height.

BN $MoS_2$

Fig.23. Warm stamped specimens with two different lubricants.

# 4. Forming limit theoretical prediction

## 4.1 The basic concept

M-K theory is proposed by Z. Marciniak and K. Kuczynski in 1967 [21]. The foundation of M-K model is groove and thickness non-uniform assumption. With this assumption, the sheet localized necking happened by the initial surface defect. The original theoretical details have been presented in the previous chapter 2. The specific implementation will be stated here. Fig.24 is the model of M-K analysis. a zone is uniform deformation part, b zone is non-uniform deformation part, i.e., the groove part.

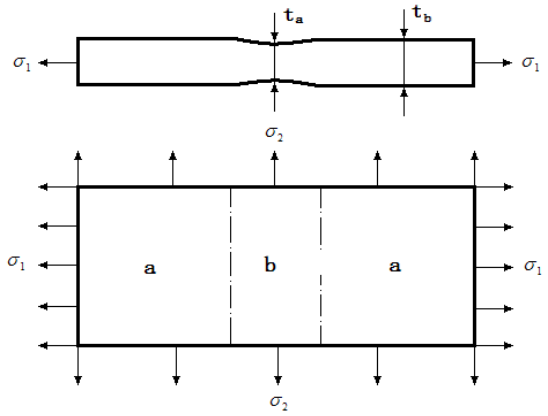


Fig. 24. Simple schematic diagram of M-K analysis.

The principle and assumption of M-K theory have presented in the chapter 2. However, the original theory is not convenient for application. In this project, the model is used with proper hypothesis. The theoretical description can be simplized as follows. Firstly, When plastic deformation happen, the stress state is different in a and b zone. If the load path is constant in a zone, the stress state keeps constant in forming process. Then the load path of b zone will change strength and stress state to meet the force equilibrium condition and geometrical coordination condition along the field surface of material, and get plane strain state, i.e., $d\varepsilon_{2b} = 0$. Finally, when the groove increases dramatically, e.g., $d\varepsilon_{1b} > 10 d\varepsilon_{1a}$, the sheet is considered broken at the groove area.

## 4.2 The fundamental of M-K theoretical prediction

There are many computation algorithms for M-K theoretical prediction. The most common used algorithm is proposed by Graf and Hosford [22]. This algorithm is simple and convenient to use. As discussed in the former chapter, the anisotropy of AZ31 magnesium alloy is not obvious at warm temperatures, and the behavior of AZ31 can be considered isotropy over $100^0$C. So, the Von Mises yield criterion is used in this project. As for simplification, the stress strain relationship is assumed in the ideal status, and the parameters are described in simple notations.

### 4.2.1 The initial parameters

The Von Mises yield criterion is expressed as follow:

$$\frac{1}{\sqrt{2}}\sqrt{(\sigma_1-\sigma_2)^2+(\sigma_2-\sigma_3)^2+(\sigma_3-\sigma_1)^2}=\sigma_i \tag{4.1}$$

Where, $\sigma_1$, $\sigma_2$, $\sigma_3$ are the three principal stress respectively, $\sigma_i$ is equivalent stress. As for convenience, the initial setting parameters are defined as follows:

$$\alpha = \frac{\sigma_2}{\sigma_1} \tag{4.2}$$

$$\beta = \frac{\mathrm{d}\varepsilon_i}{\mathrm{d}\varepsilon_1} \tag{4.3}$$

$$\rho = \frac{\mathrm{d}\varepsilon_2}{\mathrm{d}\varepsilon_1} \tag{4.4}$$

$$\varphi = \frac{\sigma_i}{\sigma_1} \tag{4.5}$$

Where, $\alpha$, $\beta$, $\rho$ and $\varphi$ are the stress ratio, equivalent strain increment ratio, strain increment ratio and equivalent stress ratio respectively.

The sheet is in the plane stress state, i.e., $\sigma_3 = 0$. Introducing the parameter $\alpha$ into yield criterion, the effective stress can be expressed as follow:

$$\sigma_i = |\sigma_1| \sqrt{1 - \alpha + \alpha^2} \tag{4.6}$$

The parameter $\varphi$ also can be introduced into the above expression.

$$\varphi = \sqrt{1 - \alpha + \alpha^2} \tag{4.7}$$

With Levy-Mesis increment theory, the proportion of stress increment can be expressed as follows:

$$\frac{\mathrm{d}\varepsilon_1}{\sigma_1 - \sigma_m} = \frac{\mathrm{d}\varepsilon_2}{\sigma_2 - \sigma_m} = \frac{\mathrm{d}\varepsilon_3}{\sigma_3 - \sigma_m} = \frac{3}{2}\frac{\mathrm{d}\varepsilon_i}{\sigma_i} \tag{4.8}$$

$$\sigma_m = \frac{1}{3}\left(\sigma_1 + \sigma_2 + \sigma_3\right) \tag{4.9}$$

In the expression, $\sigma_m$ is the hydrostatic stress. Under plane stress state, the expression can be simplified following.

$$\frac{\mathrm{d}\varepsilon_1}{2 - \alpha} = \frac{\mathrm{d}\varepsilon_2}{2\alpha - 1} = \frac{-\mathrm{d}\varepsilon_3}{1 + \alpha} = \frac{\mathrm{d}\varepsilon_i}{2\sqrt{1 - \alpha + \alpha^2}} \tag{4.10}$$

Introducing the parameter $\rho$ into the above expression, it can be converted as follow:

$$\rho = \frac{\mathrm{d}\varepsilon_2}{\mathrm{d}\varepsilon_1} = \frac{\dot{\varepsilon}_2}{\dot{\varepsilon}_1} = \frac{2\alpha - 1}{2 - \alpha} \tag{4.11}$$

Similarly, introducing the parameter $\beta$ into equation, the parameter can be expressed as follow:

$$\beta = \frac{\mathrm{d}\varepsilon_i}{\mathrm{d}\varepsilon_1} = \frac{\dot{\varepsilon}_i}{\dot{\varepsilon}_1} = \frac{2\sqrt{1-\alpha+\alpha^2}}{2-\alpha} = \frac{2\varphi}{2-\alpha} \tag{4.12}$$

And then, the proportion of these two parameters is expressed following.

$$\frac{\beta}{\rho} = \frac{2\varphi}{2\alpha-1} \tag{4.13}$$

The thickness strain rate $\dot{\varepsilon}_3 = \frac{\dot{t}}{t}$ can be also introduced into equation.

$$\dot{\varepsilon}_3 = -\frac{1+\alpha}{2-\alpha}\dot{\varepsilon}_1 = -\frac{1+\alpha}{2\alpha-1}\dot{\varepsilon}_2 \tag{4.14}$$

And it also can be expressed as follow:

$$\dot{\varepsilon}_3 = \frac{\dot{t}}{t} = -(1+\rho)\dot{\varepsilon}_1 = -\frac{1+\rho}{\rho}\dot{\varepsilon}_2 \tag{4.15}$$

### 4.2.2 The strain relationship in two zones

Assuming the relationship of stress just includes strain and strain rate in the constitutive equation. The expression is following.

$$\sigma_i = K\varepsilon_i^{\,n}\dot{\varepsilon}_i^{\,m} \tag{4.16}$$

In computation, the effective strain $\varepsilon_i$ is calculated from the summation of strain increment $\Delta\varepsilon_i$. So, the effective stress can be computed as follow:

$$\sigma_i = K(\varepsilon_i + \Delta\varepsilon_i)^n \dot{\varepsilon}_i^{\,m} \tag{4.17}$$

In groove assumption, it is considered that the groove is perpendicular with the major principal stress. So, the force which is perpendicular with groove direction can be expressed as follow:

$$F_1 = \sigma_1 \cdot t \cdot w \tag{4.18}$$

Where, the $t$ and $w$ are the thickness and width respectively. It is assumed the width of groove is unit, the force can be derived as follows:

$$\sigma_1 = \frac{F_1}{t} \tag{4.19}$$

$$\sigma_i = \varphi \cdot \frac{F_1}{t} \tag{4.20}$$

$$\dot{\varepsilon}_i = \frac{\beta}{\rho}\cdot\dot{\varepsilon}_2 = -\frac{\beta}{1+\rho}\cdot\dot{\varepsilon}_3 = -\frac{\beta}{1+\rho}\cdot\frac{\dot{t}}{t} \tag{4.21}$$

$$F_1 = \sigma_i \cdot \frac{t}{\varphi} = K(\varepsilon_i + \Delta\varepsilon_i)^n \left(\frac{\beta\dot{\varepsilon}_2}{\rho}\right)^m \cdot \frac{t}{\varphi} \tag{4.22}$$

Since the increment of second principal strain is equal in a and b zone, the second principal strain rate is equal. i.e., $\dot{\varepsilon}_{2a} = \dot{\varepsilon}_{2b}$, and the maximum load is also equal in this two zone, i.e., $F_{1a} = F_{1b}$, the expression is following.

$$(\varepsilon_{ia} + \Delta\varepsilon_{ia})^n \left(\frac{\beta_a}{\rho_a}\right)^m \cdot \frac{t_a}{\varphi_a} = (\varepsilon_{ib} + \Delta\varepsilon_{ib})^n \left(\frac{\beta_b}{\rho_b}\right)^m \cdot \frac{t_b}{\varphi_b} \tag{4.23}$$

The thickness strain, i.e., $\varepsilon_3 = \ln\left(\frac{t}{t_0}\right)$, is transferred as $t = t_0 \exp(\varepsilon_3)$, and the initial imperfect ratio, i.e., $f = \frac{t_{b0}}{t_{a0}}$, the expression can be converted as follow:

$$\frac{t_b}{t_a} = \frac{t_{b0}}{t_{a0}} \exp(\varepsilon_{3b} - \varepsilon_{3a}) = f \cdot \exp(\varepsilon_{3b} - \varepsilon_{3a}) \tag{4.24}$$

Finally, The strain relationship in a and b zones can be gotten, the expression is following.

$$(\varepsilon_{ia} + \Delta\varepsilon_{ia})^n \left(\frac{\beta_a}{\rho_a}\right)^m \cdot \frac{1}{\varphi_a} = (\varepsilon_{ib} + \Delta\varepsilon_{ib})^n \left(\frac{\beta_b}{\rho_b}\right)^m \cdot \frac{1}{\varphi_b} \cdot f \cdot \exp(\varepsilon_{3b} - \varepsilon_{3a}) \tag{4.25}$$

## 4.3 The execution procedure of M-K prediction

The specific execution procedure of prediction is as follows:

(1) Firstly, the method is based on the groove damage theory and compares the strain increment in two zones to identify forming limits. So, it is necessary to give an initial strain increment $\Delta\varepsilon_{1b}$ in b zone, and keep constant in computation processing. Meanwhile, setting a provisional initial value $\Delta\varepsilon_{1a}$ with the condition $\Delta\varepsilon_{1b} > \Delta\varepsilon_{1a}$. The global parameters imperfection ratio *f*, strain rate coefficient *m,* strain hardening exponent *n* are also defined at the beginning. In this programming, $\Delta\varepsilon_{1b} = 0.01$, the provisional $\Delta\varepsilon_{1a} = 0.01$, and the parameter *m* and *n* are defined from tensile test experiment.

(2) Secondly, set the a zone stress ratio $\alpha_a = \frac{\sigma_{2a}}{\sigma_{1a}}$ as a constant value because of simple load state at a zone, and then get $\beta_a$ and $\rho_a$ with the convert equation. Finally, the $\varepsilon_{ia}$, $\Delta\varepsilon_{2a}$ and $\varepsilon_{3a}$ can be calculated easily with relevant formulation.

(3) Thirdly, with the M-K theoretical assumption, $\Delta\varepsilon_{2b} = \Delta\varepsilon_{2a}$. So, the b zone parameters $\rho_b$, $\beta_b$, $\varphi_b$ and $\varepsilon_{ib}$ can be obtained with convert equation. Moreover, the thickness strain in b zone $\varepsilon_{3b}$ can be obtained using the volume invariable principle.

(4) Fourthly, introducing the initial parameters into the strain relationship expression, it is easy to get the equivalent strain increment $\Delta\varepsilon_{ia}$ in a zone. And then, the computational strain increment in a zone $\Delta\varepsilon_{1a}$ can be calculated with convert equation.

(5) Fifthly, comparing the computational value $\Delta\varepsilon_{1a}$ with the provisional initial value $\Delta\varepsilon_{1a}$. If the difference can be ignored, stop the computation. If the difference can not ignore, adjust the initial value $\Delta\varepsilon_{1a}$ and compute again.

(6) Finally, comparing the computational value $\Delta\varepsilon_{1a}$ with the constant setting value $\Delta\varepsilon_{1b}$, if $\Delta\varepsilon_{1a} < \Delta\varepsilon_{1b}/10$, print the $\varepsilon_{1a}$ and $\varepsilon_{2a}$. When the parameter $\alpha_a > 1$, stop the iteration and the programming is end.

The flow chart for the execution procedure of M-K prediction is shown in following (Fig.25). The programming is just to show the M-K prediction application in forming limits with ideal deformation states, the real deformation process will be more complicated and the application should take into account more parameters.

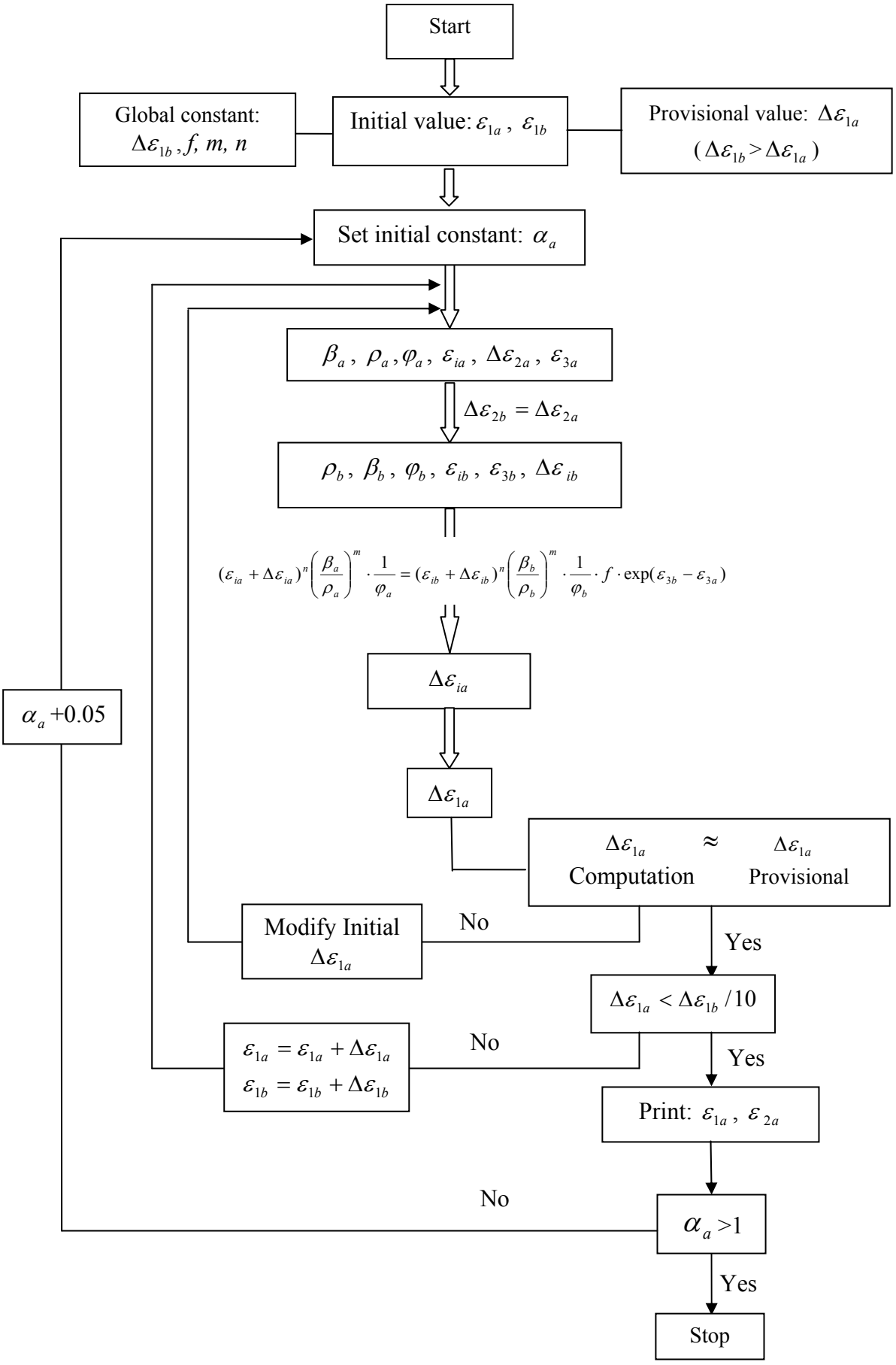


Fig.25. Flow chart for FLD theoretical prediction with the M-K Model

## 4.4 Result analysis

The prediction FLD and experiment FLD have been compared using the M-K model. Fig.26 shows the comparison result at various temperature and imperfection status. It is clearly shown that the curves which appear near the plane strain state fit much better than another area. And the curves fit better at $300^0$C, it is probably because M-K model calculate the localized necking limit strains when the specimens appear broken, and the localized necking strain is close the fracture strain at high temperature. In addition, the softening phenomenon is more obvious at high temperature that is why the prediction strains changed more softly. On the whole, the M-K prediction FLD does not fit very well with the experiment FLD. However, the tendency of both FLD is clear that the formability is better at higher temperature. Few theoretical FLC models can accurately delineate the magnesium formability at elevated temperatures, and the experimental method is still the most accurate way to evaluate the formability of HCP material [23].

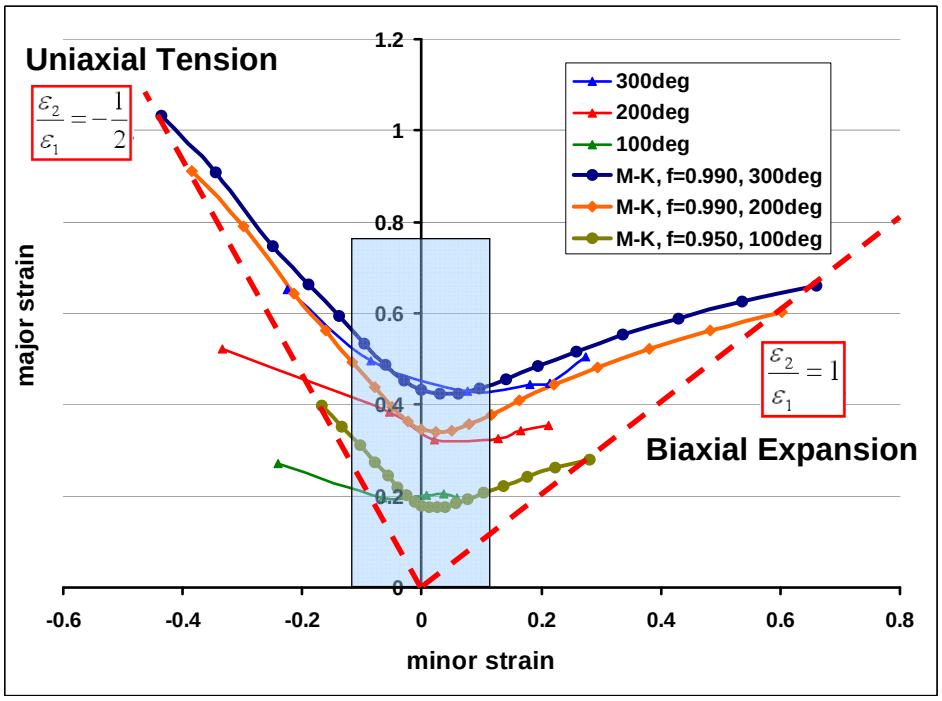


Fig.26. M-K prediction and experiment FLD comparison

# 5. Conclusion

In this chapter, the thermal formability of AZ31 magnesium alloy has been studied by Nakazima warm stamping test. Six kinds of specimens are designed by standard NF EN ISO 12004 and each specimen represents a strain path. The temperature and velocities influence are also considered. Meanwhile, the ARAMIS strain measurement system has been used to obtain the limited strains. Finally, the experimental forming limit diagram (FLD) has been obtained and it is obviously shown that the forming limit curve is higher at higher temperature. i.e., the formability is better at higher temperature.

Then, the experimental influence parameters have been studied, e.g., temperature, velocity, lubricant and strain path. the detailed analysis have been presented and lead to the conclusion that the formability is better at higher temperature and lower velocity.

In addition, the forming limit prediction has been studied by M-K model. The details of prediction program will be presented in annex. The comparison between prediction FLD and experimental FLD performed at various temperatures and based on various imperfection factors. The result is clearly shown that the tendency of both FLD is consistent although the curves just fit better near the plain strain states.

# 6. References


[1] Z. Marciniak, J. L. Duncan, J. Hu. Mechanics of sheet metal forming. Butterworth-Heinemann, 2002.

[2] D. T. Llewellyn, R. C. Hudd. Steels: metallurgy and applications. Butterworth-Heinemann, 1998.

[3] E. Doege, K. Droder. Sheet metal forming of magnesium wrought alloys - formability and process technology. Journal of Materials Processing Technology, 115 (2001), pp. 14-19.

[4] R. Neugebauer, T. Altan, M. Geiger, M. Kleiner, A. Sterzing. Sheet Metal Forming at Elevated Temperatures. Annals of the CIRP, 55 (2006), pp.793-816.

[5] P. Hora, T. Longchang, J. A. Reissner. Prediction Method for ductile sheet metal failure in FE-simulation. Numisheet conference, 1996, pp.252-256.

[6] J. Wilsius, P. Hein, R. Kefferstein. Status and Future Trends of Hot Stamping of USIBOR 1500 P. In: Geiger M, Merklein M. (Editor): Tagungsband zum 1. Erlanger Workshop Warmblechumformung, 2006, Erlangen (Germany), pp.83-101.

[7] A. Turetta, S. Bruschi, A. Ghiotti. Investigation of 22MnB5 Formability in Hot Stamping Operations. Journal of Material. Processing, Vol. 177 (2006), pp.396-400.

[8] T. Asai, J. Iwaya. Hot stamping drawability of steel. International Deep Drawing Research Group, Forming the Future: Global Trends in Sheet Metal Forming, Sindelfingen, Germany, 2004, pp.344-354.

[9] E. Lopez-Chipres, I. Mejia, C. Maldonado, A. Bedolla-Jacuinde, J. M. Cabrera. Hot ductility behaviour of boron micoalloyed steels. Materials Science and Engineering A, Vol 460-461 (2007), pp.464-470.

[10] K. Nakazima, T. Kiduma, K. Hasuka. Study on the formability of steel sheets, Yamata Technical Report, Vol. 264 (1968), pp.141-154.

[11] Z. Marciniak, K. Kuczynski, T. Pokora. Influence of the plastic properties of a material on the forming limit diagram for sheet metal in tension, International Journal of Mechanical Sciences, Vol 15 (1973), pp.789-805.

[12] H. Conrad. The role of deformation kinetics in the stretch formability of sheet metals. Journal of Mechanical Working Technology, Vol. 7 (1982-1983), pp.121-145.

[13] NF EN ISO 12004. Metallic materials: Sheet and strip - Determination of forming-limit curves. ICS: 77.040.10, 2008.

[14] F. Ozturk, D. Lee. Analysis of forming limits using ductile fracture criteria. Journal of

Mater Process Technology, 147 (2004), pp.397-404.

[15] R. Knockaert. Etude expérimentale et numérique de la localisation de la deformation lors de la mise en forme de produits minces, PhD thesis, Ecole des mines de paris, 2001.

[16] Y. Dahan. Warm formability of quenchable steel sheets, PhD thesis, Ecole des mines de paris, 2008.

[17] T. B. Huang, Y. A. Tsai, F. K. Chen. Finite element analysis and formability of non-isothermal deep drawing of AZ31B sheets. Journal of Materials Processing Technology, 177 (2006), pp.142-145.

[18] F. K. Chen, T. B. Huang. Formability of stamping magnesium-alloy AZ31 sheets. Journal of Materials Processing Technology, 142 (2003), pp.643-647.

[19] Y. S. Lee, Y. N. Kwon, S. H. Kang, S. W. Kim, J. H. Lee. Forming limit of AZ31 alloy sheet and strain rate on warm sheet metal forming. Journal of Materials Processing Technology, 201 (2008), pp.431-435.

[20] K. F. Zhang, D. L. Yin, D. Z. Wu. Formability of AZ31 magnesium alloy sheets at warm working conditions. International Journal of Machine Tools & Manufacture, 46 (2006), pp.1276-1280.

[21] Z. Marciniak, K. Kuczynski. Limit strain in the processes of stretch-forming sheet metal. International Journal of Mechanical Sciences, 9 (1967), pp.609-620.

[22] A. Graf, W. F. Hosford. Calculations of forming limit diagrams. Metallurgical Transactions A, 21A (1990), pp.87-93.

[23] L. Wang, L. C. Chan, T. C. Lee. Formability analysis of Magnesium alloy sheets at elevated temperatures with experimental and numerical Method. Journal of Manufacturing Science and Engineering, Vol. 130 (2008), pp.1-7.

# Chapter 5 Finite Element Simulation

## Contents

# 1. Introduction

The CAE (computer aided engineering) technology is an important technical improvement in sheet metal forming in the last 21century. And the key is finite element analysis (FEA) technology which is widely used in industry for processes and dies design today [1]. The main goal of finite element simulation in manufacturing process design is to reduce part development time and cost while increasing quality and productivity. In metal forming process study, simulation can not only be used to develop the die design and establish process parameters, but also very beneficial in improving grain flow and microstructure, optimizing product design, etc [2].

The history of finite element method can be traced back to the work by Alexander Hrennikoff (1941) and Richard Courant (1942), who used this method to solve complex elasticity and structural analysis problems [3]. The principle of finite element method is based either on completely eliminating the differential equation (steady state problems), or converting the partial differential equations into an approximate system of ordinary differential equations, which are then numerically integrated using standard solving techniques such as Euler method, Runge-Kutta method, etc [4]. With the development of finite element method, a variety of specializations such as aeronautical, mechanical, and automotive industries commonly use finite element method in design and development of their products. And the commercial FEM packages have developed rapidly in last two decades, e.g., ABAQUS, ANSYS, NASTRAN, etc. Recently, thanks to the advancements in computer technology, finite element simulation and optimization have been used widely in the most innovative way. Using finite element analysis, it is now possible to design and optimize metal forming process to a level that could not be reached by traditional theoretical and experimental methods. The development direction of FEA software focus on the more powerful meshing function, solving more complicated non-linear problem, more degrees of freedom in multi-physics field, more enhanced pre and post processing functions, etc [5].

In this project, in order to determine the feasibility of warm stamping process for AZ31 magnesium alloy, the numerical simulation is an essential tool. The processes of a hemisphere punch deep drawing test and a cross-shaped cup deep drawing test have been simulated intensively. The commercial finite element software FORGE® and ABAQUS® are used in this project. In the hemisphere punch deep drawing simulation, the purpose is to study the warm Nakazima test in numerical analysis method. The results have been analyzed comprehensively and the comparison between simulation and experiment has been made to

identify the reliability of simulation. Meanwhile, the simulation accuracy of two softwares (FORGE and ABAQUS) is compared to enhance simulation process. In the cross-shaped cup deep drawing simulation, the punch load, temperature distribution and thickness distribution have been studied completely, and the result compared with other software results.

# 2. Presentation of finite element theory

Finite element numerical simulation process is a comprehensive technology within multidiscipline analysis. In order to use in the industrial application, a lot of studies have been done in the last three decades such as element model, constitutive model, contact model and solving algorithm, etc [6, 7].

## 2.1 Basic finite element theory

### 2.1.1 Element technology overview

In the finite element analysis, the basic concept is element. Generally, an element is characterized in the following aspect, i.e., family, degrees of freedom, number of nodes, formulation and integration. The most commonly used element types in numerical analysis are shown in Fig.1. One of the major distinctions between different elements is the geometry type. In sheet metal forming simulation, the element technology development is grossly from membrane element, continuum elements to shell element [7].

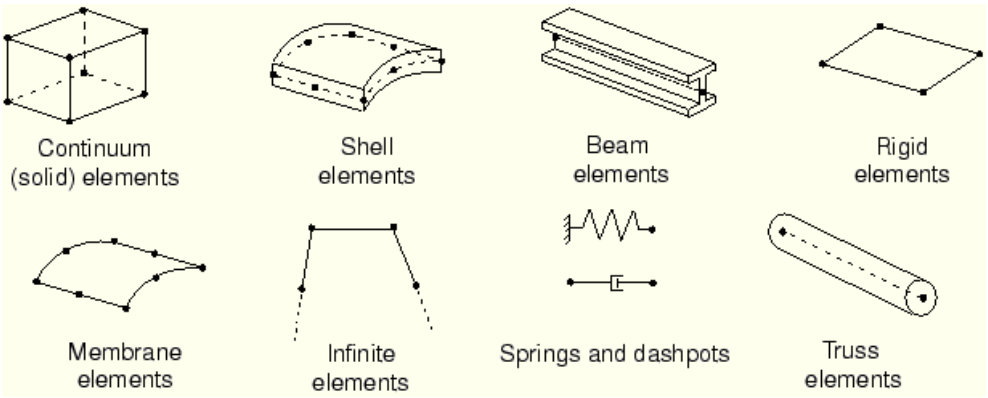


Fig.1. Finite element families used in analysis [6].

Firstly, the membrane element is $C_0$ type element (displacement continuous). It has simple structure and small memory requirement, and is the earliest used element in material forming simulation [8]. But it ignores the bending influence and considers the uniform

thickness strain distribution. So, it is just suitable to analyze the forming process in which the bending effect is not obvious.

The solid element is also $C_0$ type element. It considers the bending and shearing effects, and its format is even more concise than membrane elements. But when it is used to analyze in stamping forming process, finer meshes must be used because of small sheet thickness in order to avoid stiffness matrix singular [8]. However, the element efficiency is low, especially for dealing with complex forming parts, e.g., Automobile body panel simulation. So, it seldom uses this kind of element in sheet metal stamping application nowadays.

The shell element based on shell theory is widely studied at present because of its efficiency. It can be used in analyzing bending and shearing process, and the solving time and memory using are less than continuum elements. The shell element can be divided into two types. One is based on classical Kirchhoff shell theory, and another one is based on Mindlin shell theory. The former one need to construct $C_1$ continuous (first order continuous) interpolation function, this is very difficult in 3D analysis, so it seldom use in sheet stamping simulations now. The latter one use the displacement and rotation dependent method, and then transfer the constructing $C_1$ into $C_0$ continuous interpolation function. The problem can be simplified and the calculation accuracy can be satisfied [6-8]. Overall, the shell element is the most used element in sheet metal forming process simulation.

### 2.1.2 Finite element formulation solving algorithm

The finite element formulation solving method can be divided into static implicit, static explicit and dynamic explicit three types based on various time integrations [6-9]. The brief introduction of formulation solutions are presented here. Generally, the equilibrant equation established from finite element discretization can be expressed as follow:

$$M\ddot{u} + C\dot{u} + f_i = f_e \tag{5.1}$$

Where, $M$ and $C$ are the mass matrix and damping matrix, $u$ is the node displacement tensor, $f_i$ and $f_e$ are the equivalent internal force tensor and equivalent node force tensor respectively.

**1) Static explicit method**

If the velocity and acceleration influence can be ignored, the equilibrant equation can be simplified as follows [10, 11].

$$f_i^t = f_e^t \tag{5.2}$$

$$f_i^{t+\Delta t} = f_e^{t+\Delta t} \tag{5.3}$$

The increment equation can be expressed following.

$$f_i^{t+\Delta t} - f_i^t = f_e^{t+\Delta t} - f_e^t = \Delta f_e \tag{5.4}$$

If using Taylor expansion and just maintaining the linear part, the equation can be converted as follow:

$$f_i^{t+\Delta t} - f_i^t \approx \frac{\partial f_i}{\partial u}\Big|_{u^t} \left(u^{t+\Delta t} - u^t\right) = k(u^t)\Delta u_1 \tag{5.5}$$

And then, the equation solution can be calculated from above expression as follows:

$$\Delta u_1 = k^{-1}(u^t)\Delta f_e \tag{5.6}$$

$$u_1 = u^t + \Delta u_1 \tag{5.7}$$

When $\Delta f_e$ is small, it can be assumed $u^{t+\Delta t} = u_1$.

This is the format of static explicit method.

**2) Static implicit method**

When the external force increment step $\Delta f_e$ is large, the equilibrant equation can not obey the above assumption. In this case, the force equilibrant difference can be noted as additional increment $\Delta R$, the new equilibrant equation can be expressed as follow [11].

$$f_i(u^{t+\Delta t}) - f_i(u_1) = \Delta R \tag{5.8}$$

Similarly, using Taylor expansion and just maintaining the linear part, the equation is converted as follow:

$$f_i(u^{t+\Delta t}) - f_i(u_1) \approx \frac{\partial f_i}{\partial u}\Big|_{u_1} \left(u^{t+\Delta t} - u_1\right) = k(u_1)\Delta u_2 \tag{5.9}$$

Then the new equation solution can be expressed as follows:

$$\Delta u_2 = k^{-1}(u_1)\Delta R \tag{5.10}$$

$$u_2 = u_1 + \Delta u_2 \tag{5.11}$$

The solving can reach by repeating above procedure until the solution $u^{t+\Delta t}$.

This is the format of static implicit method.

**3) Dynamic explicit method**

If the velocity and acceleration influence can not be ignored, the matrix $M$ and $C$ can be converted to diagonal matrix using proper method. Considering the equilibrant equation in $t$ times, the node displacement $u^{t+\Delta t}$ at $t+\Delta t$ times can be expressed as follow:

$$u^{t+\Delta t} = (\frac{1}{\Delta t^2} M + \frac{1}{2\Delta t} C)^{-1} \left[ f_e - f_i + \frac{M}{\Delta t^2}(2u^t - u^{t-\Delta t}) + \frac{C}{2\Delta t} u^{t-\Delta t} \right] \quad (5.12)$$

This is the format of dynamic explicit method [12].

Metal forming process is normally as quasi-static process, the traditional numerical solution mainly use static implicit method, because the forming process and the model is simple, the static implicit method calculation efficiency is higher than dynamic explicit method for there simple model. And the contact condition is simple, so the convergence is easy to reach. With the development of application, more and more complex part used in simulation, the disadvantage of static implicit method occurs such as the iteration convergence difficulty, the long CPU time and lager bandwidth of the overall stiffness matrix, etc [6, 11, 12].

So, the dynamic explicit method is used widely without convergence problem so far, but the main disadvantage of solution is conditional stable. It means that each time increment must be less than the critical time step. For the metal forming quasi-static problem, the common application is using dynamic explicit method in loading process and static implicit method in unloading process [6, 8, 12].

### 2.1.3 Contact technology overview

In the metal forming process, the contact friction between blank and tools is an inevitable problem. The problem is a typical boundary condition non linear problem. A mount of research have been studied since 1970s [13], it mainly includes contact searching method, normal contact force and tangent friction force solving method, etc.

The contact technology includes two relevant aspects [6-8, 14]. One is the recognition of contact area, and another one is reaction force in the contact area. The most intuitive and widely used contact searching method is master-slave surface method. In this method, one of contact surface is defined as master surface (active surface), and another one is specified as slave surface (driven surface). The node in the active surface is called master node, correspondingly, the node in the driven surface is called slave node. The main difference between these two surfaces is that the master node can penetrate slave segment, but the slave node can not penetrate master segment (Fig.2).

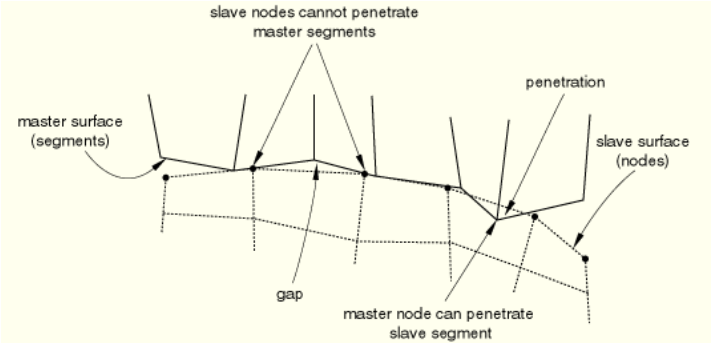


Fig.2. Master-slave surface and penetration of master nodes into slave surface [6].

The contact force solving methods are mainly included Lagrange multiplier method and penalty function method. In Lagrange multiplier method, the contact force is treated as additional freedom degree. So, it needs to solve the finite element equation by iteration and increases the system freedom degrees, and this method is generally used for implicit algorithm. The contact technology based on penalty function is widely used in explicit algorithm. Because this method has higher solving efficiency without increasing system freedom degree.

In forming process simulation, the contact condition between blank node and tools must be searched in each step. The contact node searching methods include global searching and local searching. The global searching aims to all of nodes in the model, it uses loop searching method to judge the corresponding position between blank node and tool surface. The contact element segment can be identified when the blank contact with tools. The local searching is used to identify the exact node position according the relationship between nodes and contact element segments.

The amount of penetration can be calculated after searching contact nodes. The expression can be expressed as follow [6].

$$L = n_i \cdot \left[ t - r(\xi_c, \eta_c) \right] \tag{5.13}$$

Where, $n_i$ is the unit outward normal vector of master segment $S_i$ in the contact node $(\xi_c, \eta_c)$. It is expressed as follow:

$$n_i = \frac{\dfrac{\partial r}{\partial \xi}(\xi_c, \eta_c) \times \dfrac{\partial r}{\partial \eta}(\xi_c, \eta_c)}{\left| \dfrac{\partial r}{\partial \xi}(\xi_c, \eta_c) \times \dfrac{\partial r}{\partial \eta}(\xi_c, \eta_c) \right|} \tag{5.14}$$

If the penetration $L \geq 0$, it means the node $n_s$ does not penetrate the master surface, there is no contact force to solve. If the penetration $L < 0$, the node $n_s$ penetrate the master surface segment $S_i$, the contact force can be calculated by normal force and tangent force.

#### 2.1.3.1 Normal contact force

The tangent contact force can be calculated by penalty function method. This method decreases the tangent displacement constraint and allows the objectives penetrating each other between contacts, so the potential energy will be changed in the contact node. The elastic media with high strength is introduced to simulate the interaction between two objectives in order to satisfy approximately the displacement boundary condition. The additional tangent contact force vector $f_n$ is added between $n_s$ and $S_i$. The expression is following [6].

$$f_n = -Lk_i n_i \tag{5.15}$$

Where, $k_i$ is penalty factor, means the stiffness factor of master segment $S_i$. It is defined by the volume modulus $K_i$, volume $V_i$ and master segment area $A_i$. The expression is following.

$$k_i = \frac{f_{si} K_i A_i^2}{V_i} \tag{5.16}$$

Where, $f_{si}$ is the stiffness proportional factor in the boundary.

#### 2.1.3.2 Tangent contact force

The tangent contact force (friction force) is generally calculated by the classical coulomb friction law [6]. But it will induce two numerical stability problems using this law. One is the determination of contact condition changment, another one is determination of contact friction force direction. The modified coulomb friction law can deal with this problem, and it can be expressed as follow [6].

$$f_t = -\mu \| f_n \| \left\{ \frac{2}{\pi} tg^{-1} \left( \frac{\| \Delta u_t \|}{C_r} \right) \right\} \frac{\Delta u_t}{\| \Delta u_t \|} \tag{5.17}$$

Where, $f_t$ and $f_n$ are the node tangent friction force and normal contact force respectively, $\Delta u_t$ is the relative tangent displacement increment between blanks nodes and tools. $\mu$ is the friction coefficient between nodes and contact surface. $C_r$ is the critical relative slipping velocity.

Considering the change from static to dynamic process, the friction coefficient can be expressed as follow:

$$\mu = \mu_d + (\mu_s - \mu_d)e^{-c|v|} \tag{5.18}$$

Where, $\mu_d$ and $\mu_s$ are the dynamic and static friction coefficient respectively. $c$ is the attenuation constant, $v$ is the relative velocity between nodes and master segment.

## 2.2 FORGE 3D

FORGE® software, based on the finite element method, is used to simulate hot, warm and cold forming of 3D parts. The software uses thermo-viscoplastic or thermo-elastic-viscoplastic laws for forming simulation. For warm and cold forming processes, a thermo-viscoplastic model enables the prediction of residual stresses and geometrical dimensions at the end of the forming. Anisotropic Hill model and kinematical hardening can be considered to represent the plastic material behavior. The stability of automatic meshing and remeshing procedure based on volume failure model and fourier thermal exchange model enable the simulation of geometrically complex parts. Meanwhile, the parallel or cluster version of FORGE decreases the computations time and thus enables the use of meshes consisting of many nodes [15].

### 2.2.1 Weak formulation

In FORGE software, a mixed velocity-pressure formulation is used based on hypothesis. The basic equations correspond to the mechanical equilibrium and the evolution of the pressure without considering bulk force, inertia and thermal effects. So, the equilibrium equation can be expressed simplify as follows [16].

$$div(\sigma) = 0 \qquad \Rightarrow \qquad div(s) - \nabla p = 0 \tag{5.19}$$

$$tr(\dot{\varepsilon}) + \frac{\dot{p}}{\chi} = 0 \tag{5.20}$$

Where, $\sigma$ and $s$ are the stress and deviatoric stress tensors, $p$ is the pressure and $\chi$ is the compressibility coefficient of material. The stress is written as a function of strain rate which is related to the velocity. So, the problem can be summarized to find the solution as follows:

$$div(s(\vec{v}) - \nabla p = 0 \tag{5.21}$$

$$tr(\dot{\varepsilon}(\vec{v})) + \frac{\dot{p}}{\chi} = 0 \tag{5.22}$$

Where, the domain $\Omega$, $V$ and $P$ are the spaces of corresponding function respectively.

Finally, the problem to be solved is transformed into a week form by multiplying the two equations by admissible function $\vec{v}^*$ and $p^*$. The problem is transferred as follows with Green's theorem [6].

$$\int_\Omega s(\vec{v}) : \dot{\varepsilon}(\vec{v}^*) d\Omega - \int_\Omega p \cdot tr(\dot{\varepsilon}(\vec{v}^*)) d\Omega - \int_{\partial\Omega} \vec{T} \cdot \vec{v}^* dS = 0 \qquad \forall \vec{v}^* \in V \tag{5.23}$$

$$\int_\Omega p^* [tr(\dot{\varepsilon}(\vec{v})) + \frac{\dot{p}}{\chi}] d\Omega = 0 \qquad \forall p^* \in P \tag{5.24}$$

Where, $\vec{T}$ corresponds to load boundary conditions on the boundary of $\Omega$.

### 2.2.2 Finite element discretization

The discritization is a critical step in the whole analysis procedure. Finite element discretization consists in dividing the domain $\Omega$ into subdomain $\Omega_e$. $\vec{v}_e$ and $p_e$ are the solution in a given element. In practice, the solutions $\vec{v}_e$ and $p_e$ are generated from a discrete number of base functions defined on $\Omega_e$. One problem is the choice of the interpolation for the pressure and the velocity in order to avoid locking. The finite element used in FORGE is called "mini-element" [16]. It is a four node tetrahedron with linear interpolation of velocity and pressure. Moreover, the interpolation of the velocity field is enriched with an additional component different to zero inside the tetrahedron. This component is called the bubble field and an additional node is added in the centre of the element. The bubble field is linear in each of the sub-tetrahedral formed by this central node and three of other nodes in the element. Fig.3 illustrates the mini-element in FORGE. The velocity field includes two components, the linear field and the bubble field [16].

$$\vec{v}_e = \vec{v}_e^l + \vec{b}_e \tag{5.25}$$

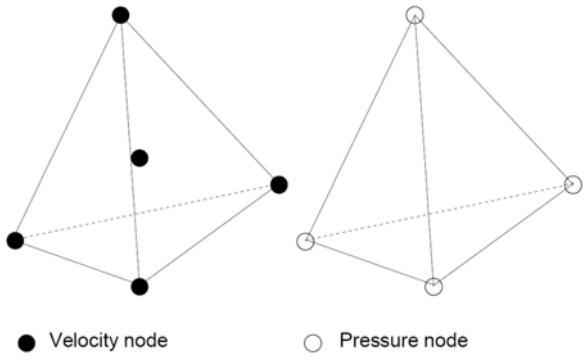


Fig.3. P1+P1 mini-element in FORGE [16].

Considering the test function is also given as the sum of a linear and a bubble field, and using a series of function decomposition, the system of weak formulation can be finally written as follows:

$$\int_{\Omega_e} s^l : \dot{\varepsilon}(\vec{v}^{l^*}) d\Omega_e - \int_{\Omega_e} p_e \cdot tr(\dot{\varepsilon}(\vec{v}^{l^*})) d\Omega_e - \int_{\partial\Omega_e} \vec{T} \cdot \vec{v}^{l^*} dS = 0 \quad \forall \vec{v}^{l^*} \in V_e^l \qquad (5.26)$$

$$\int_{\Omega_e} s^b : \dot{\varepsilon}(\vec{b}^*) d\Omega_e - \int_{\Omega_e} p_e \cdot tr(\dot{\varepsilon}(\vec{b}^*)) d\Omega_e - \int_{\partial\Omega_e} \vec{T} \cdot \vec{b}^* dS = 0 \quad \forall b^* \in V_e^b \qquad (5.27)$$

$$\int_{\Omega_e} p^* [tr(\dot{\varepsilon}(\vec{v}_e^l + \vec{b}_e)) + \frac{\dot{p}_e}{\chi}] d\Omega_e = 0 \qquad \forall p^* \in P_e \qquad (5.28)$$

The above equation can be solved by Newton-Raphson method, which leads to a linear system of equations whose unknows are the linear velocity, the bubble velocity and the pressure increments.

In FORGE, the purpose of bubble component is only to add stabilization terms in the linear system. Moreover, the bubble contribution can be neglected in certain case, e.g., computation of the stresses. And then the computation cost of the P1+P1 element can be reduced because the bubble unknows are not computed and only one single integration point is needed [16].

### 2.2.3 Meshing and remeshing techniques

Automatic remeshing is available in FORGE 3D. The algorithm is very efficient for massive parts calculation. However, for thin sheet, the part thickness is very small comparing with its other dimensions, so the remeshing can not always generate appropriate meshes. In this case, the following strategies are used to solve this problem [16]. Firstly, the mean surface of sheet is meshed with triangle elements. And then these triangle elements are extruded in the normal direction to the mean surface where prismatic elements are obtained. The position of the extruded nodes is computed from the sheet thickness which is stored in each of the nodes on the mean surface. Thirdly, the prisms are divided in three tetrahedral.

The corresponding 3D mesh structure can be seen as a pile-up of node layers. Each layer has the same number of nodes. The nodes in various layers are located, at least initially, along the normal direction to the mean surface. The node numbering allows to easily finding the upper and lower neighbours of a given node. Fig.4 shows the procedure to generate 3D tetrahedral element from a surface triangular mesh.

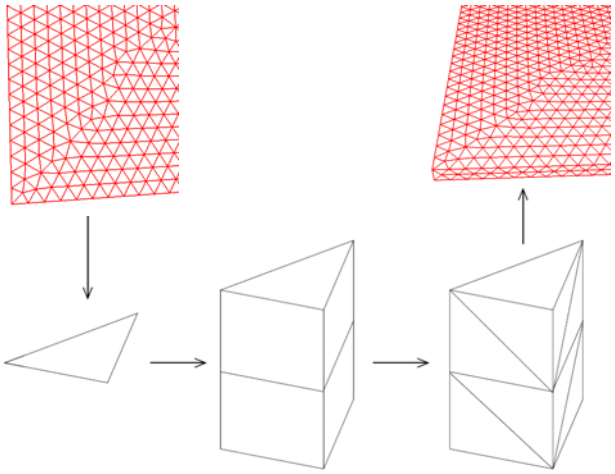

Fig.4. Generate 3D tetrahedral from a surface triangular mesh in FORGE.

When remeshing is triggered, the mean surface of the mesh is extracted and remeshed with triangles. The 3D reconstruction is carried out using the thickness stored at the mean surface nodes and transported after remeshing. The extrusion of the nodes is carried out in the normal direction of the mean surface, computed at the node level on the new 2D mesh. This nodal value in the normal direction is average among the normal triangular elements adjacent to the node weighted by the surface of these triangles. The nodal value of the thickness is simply computed as the distance between two corresponding nodes at the upper and lower surfaces of the 3D mesh. Meanwhile, the thickness shearing is neglected [16-17].

The example of deep drawing simulation is presented to illustrate the remeshing procedure. The meshes used in this test are made of three layers of nodes, corresponding to two tetrahedral through the sheet thickness. Fig.5 shows the initial and the final meshes after deep drawing process. Remeshing is triggered by the proximity to the most curved areas of the tools.

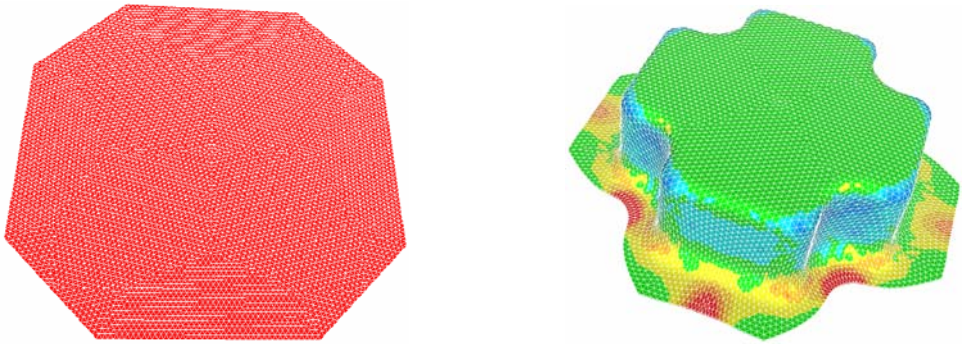

Fig.5. Initial mesh (left) and final mesh (right) after deep drawing process.

The mesh size reduction is not very obvious near the critical areas because the number of elements is too much when the size is small enough. This test also shows the possibility for

the remeshing to maintain good mesh quality during the whole simulation. However, one problem remains for tools with local small radii of curvature. Remeshing may then result in the additional nodes deeply inside the tool as sketched in Fig.6. Usually, this does not cause important problems since the position of the critical nodes is successively corrected during the next increments. However, very high penetrations may lead to convergence problem in certain case [15-17].

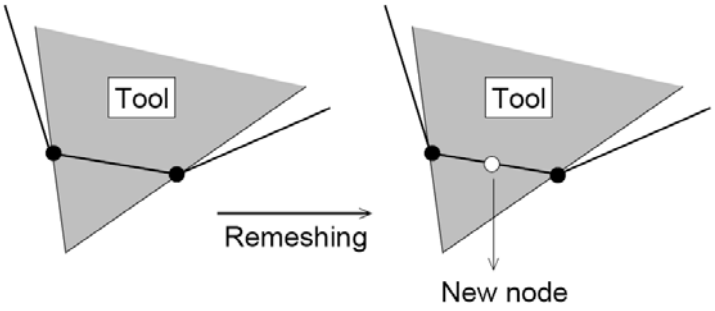


Fig.6. Additional nodes with a high tool penetration after remeshing [16].

# 3. Hemisphere punch deep drawing simulation

To determine the feasibility of warm stamping process for AZ31 material, the numerical simulation is an essential tool. In this project, the model of warm Nakazima tests with hemisphere punch has been created with FORGE and ABAQUS. As in the experiment set-up, the model gathers a blank, a punch, a die and a blank-holder. In forming process simulation, a large number of model parameters have to be identified in order to simulate precisely, such as blank holder force, the friction coefficient, the thermal exchange coefficient, etc. In this simulation, the sensitivity of process parameters have been analyzed for AZ31 formability and the comparison between simulation and experiment has been made to identify the reliability of simulation. Meanwhile, there are some researches for the parameters identification published in literatures [18-19].

## 3.1 The model

Firstly, the Nakazima stamping simulations are conducted for AZ31 at various temperatures using FORGE. In these simulations, the geometry is just constructed with quarter model about the Z-axis due to axisymmetric deformation. The blank is meshed with two elements along the thickness to obtain thickness distribution. Furthermore, simulations with various temperatures are performed in order to determine the temperature influence. Smaller meshes are created in forming zone, and the coarse meshes are used in flange area in

order to improve calculation efficiency. The drawbead is also used in simulation as real Nakazima stamping test.

Secondly, the simulation model is created in ABAQUS using ABAQUS/Standard analysis. The tool geometries are same with the experimental Nakazima stamping specimen geometries. The FE model is modeled over a unit radian about the Z-axis due to the axisymmetric deformation. The free meshing method is used with precise node controlling in the preprocessor, a 4-node reduced integration shell element (S4R) is selected in mesh type, and with four integration points along the thickness. These elements have both temperature and displacement as their freedom degrees to predict both deformation and temperature variation during the process. The static general step is used for stamping process (ABAQUS/Standard). The die, blank-holder and punch are considered as analytical rigid. The schematic diagrams of FE model are shown in Fig.7.

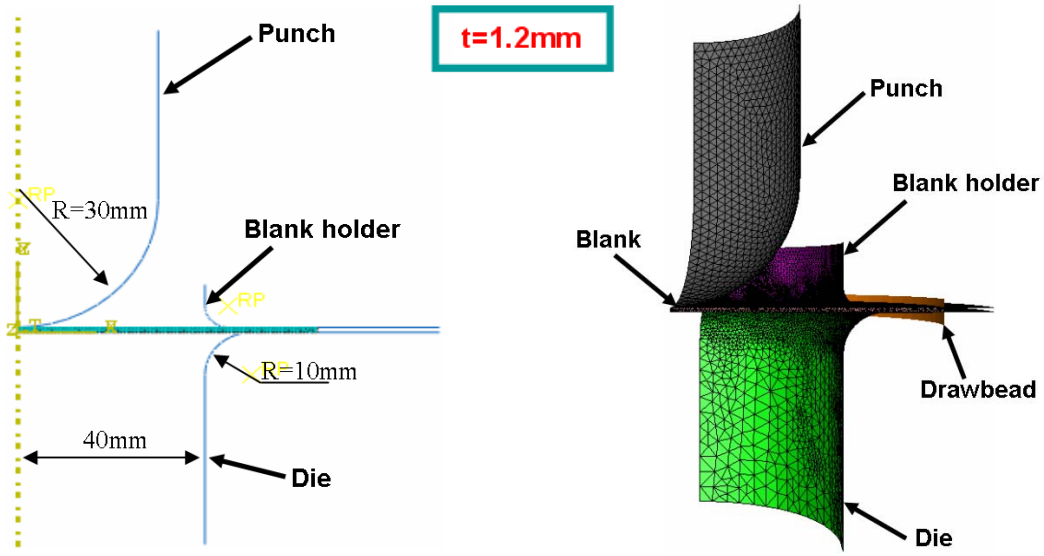


(a) ABAQUS model (b) FORGE model

Fig.7. FE model (1/4 model) in the hemispherical punch sheet forming process.

The flow stress of AZ31 magnesium alloy obtained from tensile test is used in the simulation. The flow stress for the calculated strains, temperature and strain rate are logarithmically interpolated and extrapolated using the available input data. The friction coefficient used in the simulations is referred from literature [18] and it is assumed not to vary locally with interface temperature and pressure. The interface heat transfer coefficient is assumed to be uniform for the entire surface and the value is selected based on the results published in the literature [19]. The blank holder force also plays an important role in

simulation. In this project, constant blank holder force is used. Meanwhile, the anisotropy is not considered. The inputs to the FE simulation are shown in table.1.

Table.1. Process parameters used in simulation

| **Tools setup:** | **Mechanical properties:** |
|---|---|
| Punch diameter (mm): 60 | Density (kg/dm$^3$): 1.78 |
| Blank-holder and die corner radius (mm): 10 | Young's modulus, *E* (GPa): 45 |
| Thickness (mm): 1.2 | Poisson's ratio, *v:* 0.3 |
| Friction coefficient, μ: 0.10 | |
| Blank holder force (KN): 10 | |

## 3.2 Result comparison

The simulation results are analyzed by comparing with experimental results. The temperature, punch load and thickness distribution are the general comparison objectives in stamping process simulation. Meanwhile, the parameter influence is different in various strain path, temperature and process velocity. The comparisons have conducted in order to validate simulation effectiveness in complex stamping process.

### 3.2.1 Thermo-mechanical analysis

Fig.8 shows an example of the equivalent strain and stress distribution at 200$^0$C in ABAQUS. The plastic equivalent strain (PEEQ) decreases at the clearance zone between punch and die. The Von Mises stress increases with displacement increasing, and the higher value is usually located at the punch radius zone where punch contact well with the blank.

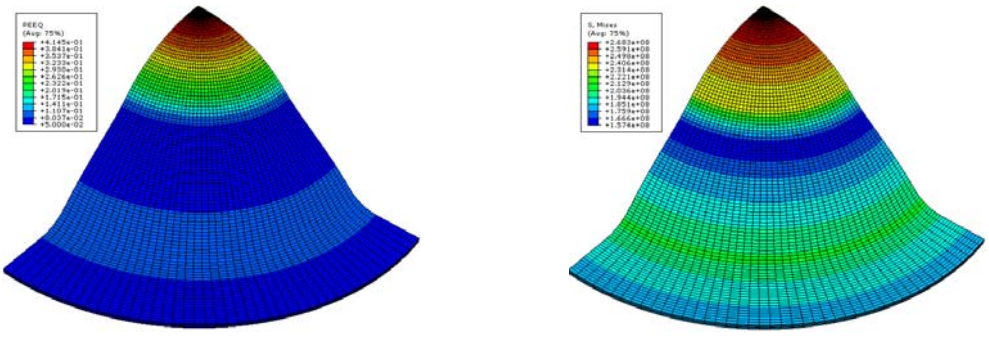

(a) Equivalent strain (PEEQ) (b) Von Mises stress

Fig.8. Distributions of equivalent strain and Von Mises stress in ABAQUS (200$^0$C).

The temperature and strain rate distribution at different steps in FORGE are shown in Fig.9. The temperature in the center area of blank is various, where the solid contact occurs

between blank and punch. And the temperatures located at the punch radius zone are higher than another zone during the process. It is probably because the real experiment set-up is sealed and the heat exchange proceeds in furnace, the heat produced in stamping process increases the temperature at punch radius zone. The distribution of strain rate indicates a clear strain localization in the zone called punch radius exit. The higher strain is usually located in the higher temperature regions, and especially at the punch radius exit zone. In this simulation, the constant punch velocity has been set, and the strain rate change slightly during process.

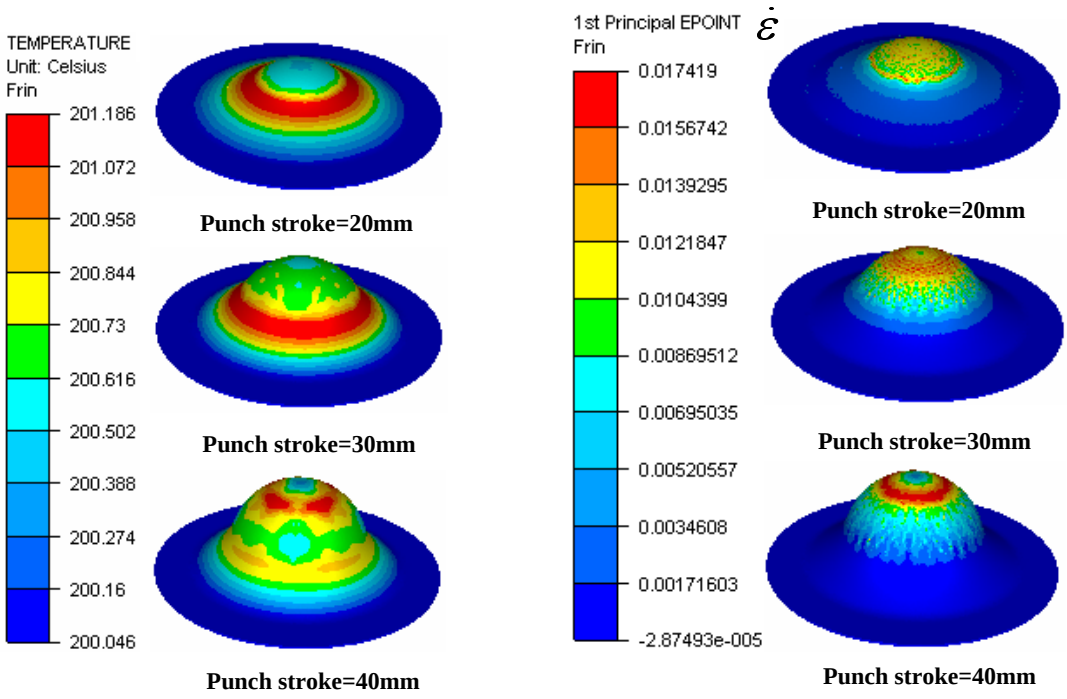


Fig.9. Result of numerical simulation for different punch strokes (FORGE).

### 3.2.2 Punch load analysis

The punch loads obtained from the simulation at various temperatures are compared with experiments in Fig.10. The maximum punch load obtained at all the simulated temperature is higher than the load in experiment. However, the tendency is obvious, when the temperature increase, the punch load decrease. And the results match well at small displacement. Nevertheless, the discrepancies appear especially at large displacement. For the test at $300^0$C, even the maximum error is up to 16%. Many reasons could explain these deviations. Firstly, the friction coefficient is probably overestimated especially at low temperature. Secondly, the real behavior model identified from tensile test well describes the hardening behavior at small displacement in each temperature, but there is deviation when displacement increases because of softening, especially at higher temperature. Thirdly, in the simulation, the material is considered isotropic. However, magnesium alloy sheets exhibit some normal anisotropy.

Probably, appropriate anisotropic yield criterion that represents yielding in magnesium alloy should be considered in simulation.

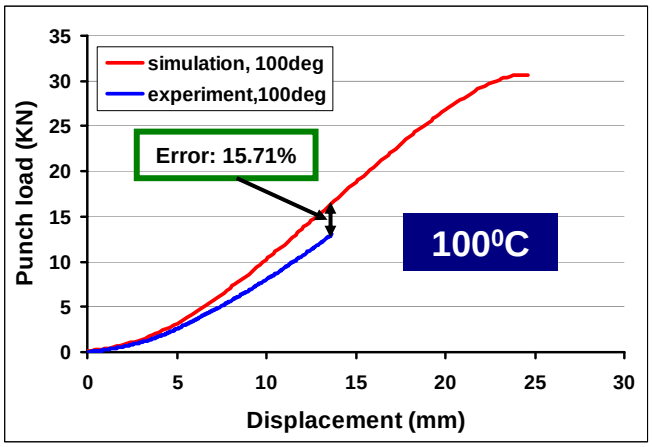


(a) T=100$^0$C

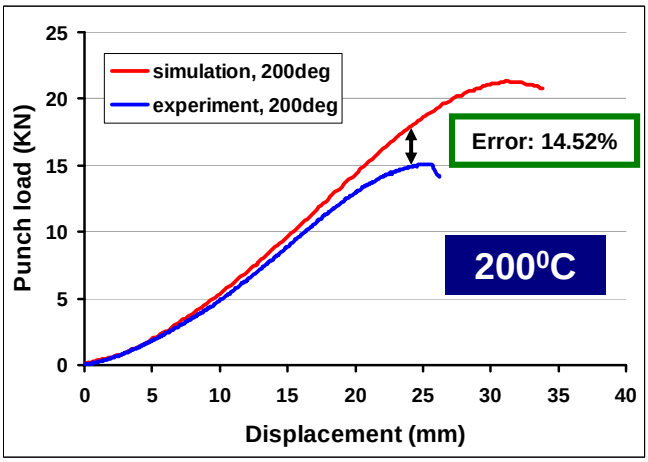


(b) T=200$^0$C

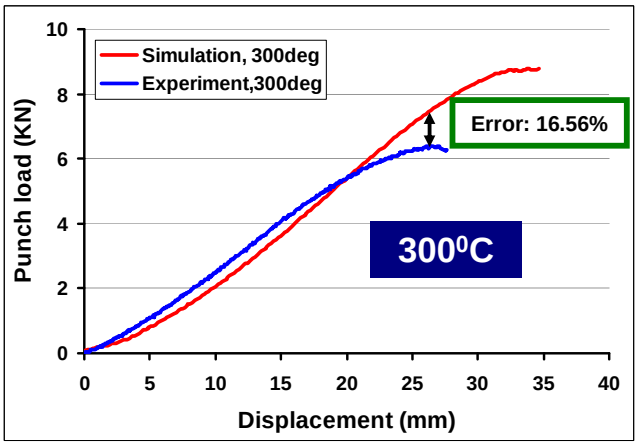


(c) T=300$^0$C

Fig.10. Punch load obtained from simulation and experiment at various temperatures (FORGE).

### 3.2.2 Thickness distribution analysis

Experimental thickness distribution is available at various temperatures obtained from ARAMIS system. Comparisons of the simulational and experimental results at $100^0$C and $200^0$C along a section of blank are shown in Fig.11 and Fig.12. The results are compared by various strain path denoted with different width in figure. The tendency of thickness distribution predicted by simulation fit with corresponding experiment result for all three geometry samples. However, less thickening and more thinning has been observed in the simulation as compared with the experiments. Maximum thinning has been observed in punch radius zone for both simulation and experiment. It is probably because the strength of the punch radius zone in warm forming is not uniform and depends on the temperature distribution. The temperature is higher in punch radius zone at all stroke positions. Therefore, low yield strength of the material at punch radius zone cause larger thinning rather than another position.

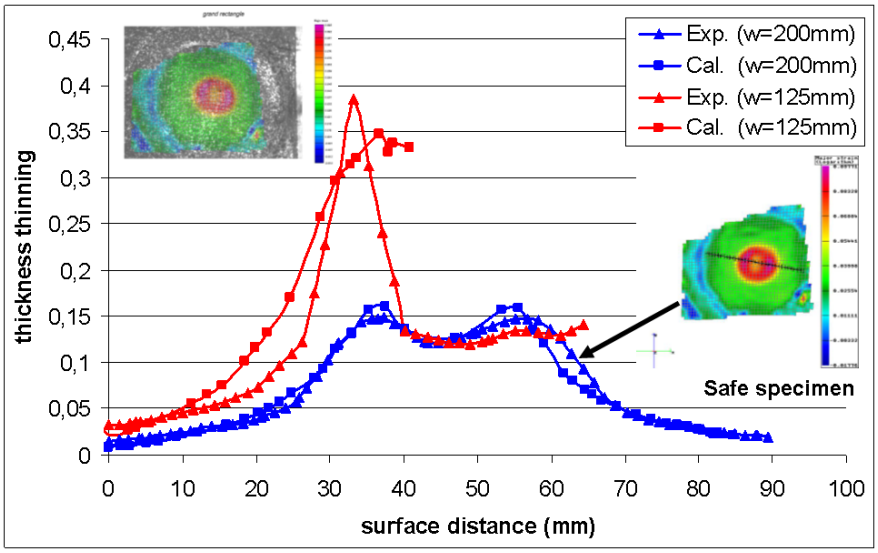


Fig.11. Thickness distribution from simulation and experiment at $100^0$C (FORGE).

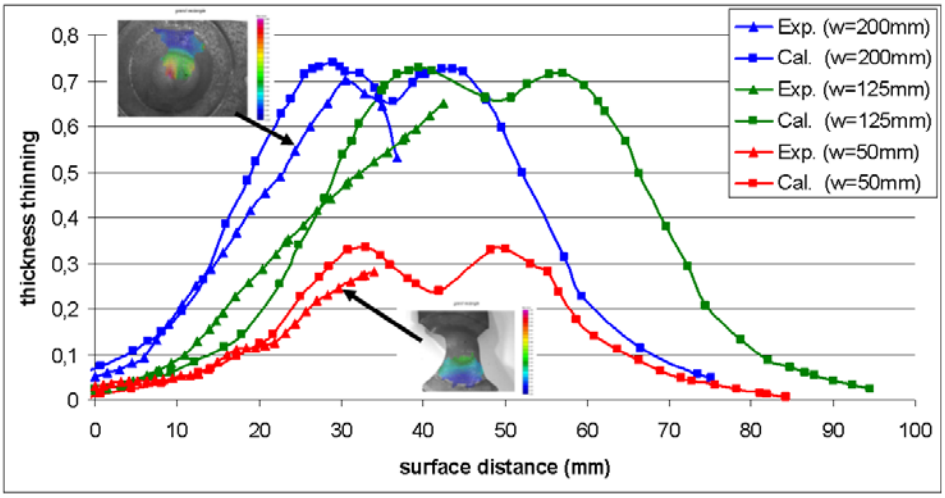


Fig.12. Thickness distribution from simulation and experiment at $200^0$C (FORGE).

Fig.13 illustrates the distribution of thickness thinning comparison between simulation and experiment at various temperatures in ABAQUS. The thickness is measured along centerline of the longitudinal direction. The figure shows the thickness variation at $100^0$C and $200^0$C with same geometry. It is shown that the similar tendency of the thickness variation and the discrepancy occurred for both comparisons, the fitting is better at $100^0$C than $200^0$C. But it is clearly shown that more thickness thinning has been observed in the simulation. This trend is same with simulation in FORGE.

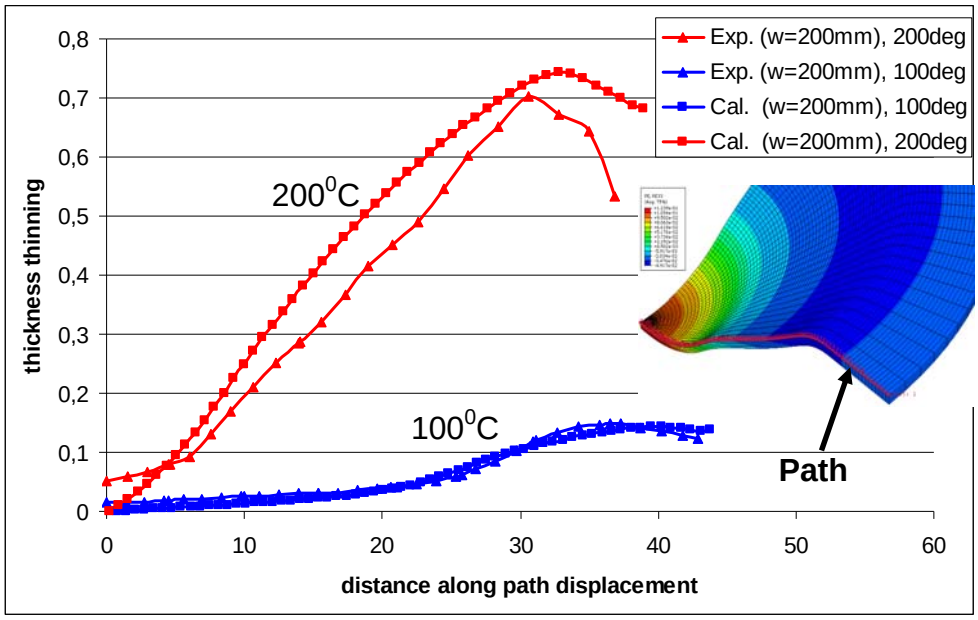


Fig.13. Thickness distribution from simulation and experiment at various temperatures (ABAQUS).

In comparison from FORGE and ABAQUS, more thinning and less thickening is observed in both simulations compared to experiments for the same process parameters. This indicate that the von Mises yield criterion used in simulation for determining yielding of the material probably over predict the yield stress in the flange where the radial stress is tensile and hoop stress is compressive [20]. It is necessary to study the influence of yield criterion on the stamping process simulation. Nowadays, much commercial finite element analysis software have interface allowing user to add own yield criterion. It is a way to compare various yield criterions in this simulation model. Meanwhile, the softening behavior also have important influence in this simulation, the softening parameters including in simulation is also a study subject in the future.

## 3.3 Comparison of simulation result in FORGE and ABAQUS

In order to compare the general result using two different simulation methods, the same hemisphere punch deep drawing simulations are conducted in FORGE and ABAQUS. Both finite element analysis codes can solve stamping process problem and similar quasi-static process. Both of them include extensive application in industry. ABAQUS is a general simulation software, including rich element types and material model. While FORGE is a professional material forming simulation software, it just use tetrahedron element in default and can be used user routine to extend material model. Table.2 shows the difference between FORGE and ABAQUS in this deep drawing simulation.

Table.2. Difference between FORGE and ABAQUS

| | FORGE | ABAQUS |
|---|---|---|
| Element type | Tetrahedron | S4R (shell element) |
| Meshing method | STL meshing | Free meshing |
| Analysis step | Static | ABAQUS/Standard (general static) |
| Material model | Stress-strain data | Stress-strain data |
| Contact model | Penalty explicit contact model | Penalty contact model |
| Friction model | Coulomb Explicit Formulation | Coulomb friction model |
| Solver technology | Newton Iteration | Based on stiffness solver |
| Failure model | Volumic failure model | Plastic failure model |
| Boundary condition | Axisymmetry | Axisymmetry |
| Blank holder load | Constant (10KN) | Constant (10KN) |

The results of punch load are compared in FORGE and ABAQUS. In the simulation, it is observed fluctuation in the load-displacement curve observed due to the oscillation of nodes in contact with the punch. Fig.14 shows the load displacement curves after smoothing in $100^0$C and $200^0$C. It is clearly shown that the curve from simulation is higher than experimental curve. Each simulation result is also different, the curve from ABAQUS is lower than FORGE at $100^0$C, but it is higher at $200^0$C. And the discrepancy between simulation and experiment is different in this two simulation software. The discrepancy increases with temperature in ABAQUS. It is probably because the friction is sensitive with temperature increasing. The same conclusion has been made in other study [21].

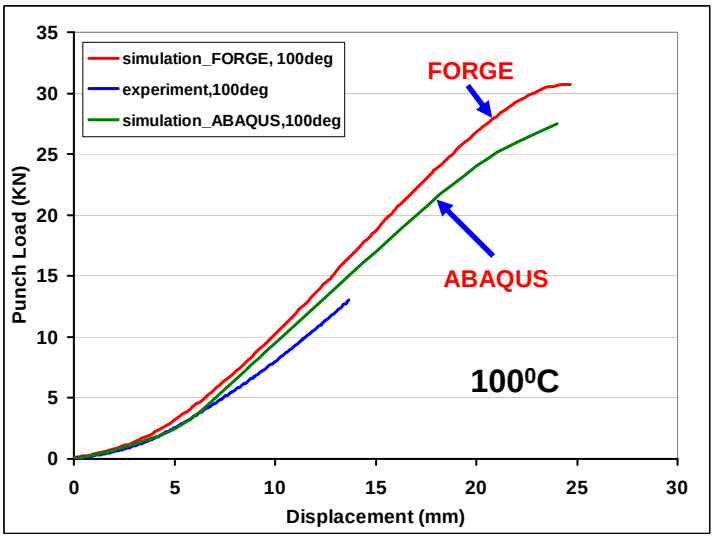


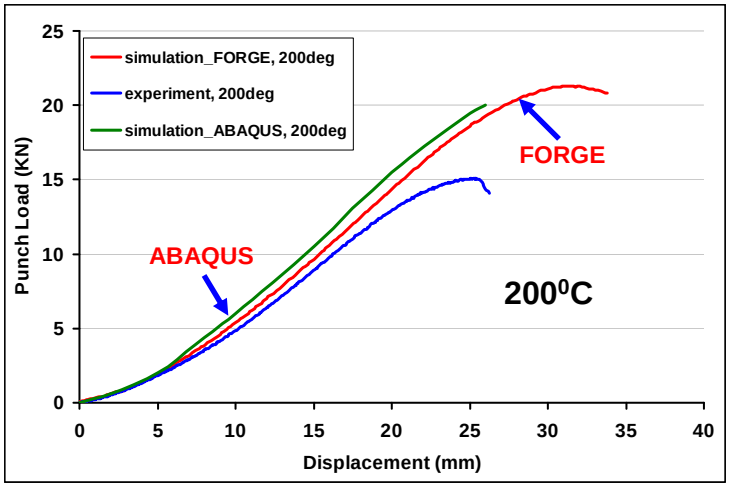


Fig.14. The comparison of punch load in FROGE and ABAQUS.

## 3.4 Damage model used in FORGE

Damage mechanics is initialed by Kachanov and then by Lemaitre *et.al* [22]. It is a useful tool to predict failure under general three dimensional monotonic loading. In the past decade, a lot of works have been done about damage or crack behavior, in which the Cockroft & Latham model and Lemaitre model are two widely used models in application [22, 23].

### 3.4.1 Cockcroft & Latham model

The application of ductile fracture criteria for predicting the forming limit of a sheet material has been studied by various researchers using formability tests such as uniaxial tensile test, plane-strain tension test, biaxial expansion test, etc. Takuda *et al.* concluded that Cockcroft & Latham criterion could be used effectively for various materials as a ductile fracture criterion [23]. In this study, the Cockcroft & Latham criterion has been studied in

simulation. By using this criterion, the critical damage values are determined through FEA of uniaxial tension test and then applied in the deep drawing analysis. Cockcroft & Latham criterion is based on very simple expression. It is given as following equation.

$$\int_0^{\bar{\varepsilon}} \frac{\sigma^*}{\bar{\sigma}} d\bar{\varepsilon} = C \tag{5.29}$$

Where, $\sigma^*$ is the maximum normal stress, $\bar{\sigma}$ is the effective stress, $\bar{\varepsilon}$ is the fracture strain and $C$ is a material constant called Critical Damage Value (CDV). This criterion is not including strain history, and it is a default damage model used in FORGE.

### 3.4.2 Lemaitre damage model

The Lemaitre damage model is formulated through the thermodynamics of irreversible processes by means of a state potential to define the energy involved in each process, which represented by a state variable, and a potential dissipation [22]. It gives the effective stress $\bar{\sigma}$ as a function of the damage value $D$, the latter evolving with strain and stress triaxiality according following equations [24].

$$\bar{\sigma} = \frac{\sigma}{1 - hD} \tag{5.30}$$

$$\dot{D} = \left( \frac{Y}{S_d} \right)^s \dot{\bar{\varepsilon}} \qquad (\varepsilon > \varepsilon_D) \tag{5.31}$$

$$D = D_c \quad \text{(Crack initiation)} \qquad (0 \le D \le D_c \le 1) \tag{5.32}$$

Where, $h$ is a parameter which equal to 0.2 for compression solicitation and 1 in the other cases. $D$ is the scalar damage variable, it is the surface density of micro defects in any plane of a representative volume element, $\dot{\bar{\varepsilon}}$ is the equivalent plastic strain rate. $S_d$ is the damage strength. $s$ is the damage exponent. The damage threshold $\varepsilon_D$ related to the density of energy stored in the material and the critical damage $D_c$ are parameters to be identified for material at each considered temperature. The expressions are following [24-25].

$$\dot{\bar{\varepsilon}} = \left( \frac{2}{3} \dot{\varepsilon}_{ij}^m \dot{\varepsilon}_{ij}^m \right)^{\frac{1}{2}} \tag{5.33}$$

$$\varepsilon_D = \varepsilon_{tD} \frac{\sigma_u - \sigma_f}{\sigma_{eqMAX} - \sigma_f} \tag{5.34}$$

Where, $\varepsilon_{tD}$ is the threshold in tension, $\sigma_u$ is the ultimate stress and $\sigma_f$ is the fatigue limit. Then, all together, five damage parameters at most need to be identified.

$Y$ is the strain energy density release rate, the expression is following.

$$Y = -\frac{\partial W_e}{\partial D} \tag{5.35}$$

$$Y = \frac{\sigma_{eq}^2 R_\upsilon}{2E(1-D)^2} \tag{5.36}$$

Where, $W_e$ is the elastic strain energy density. $\sigma_{eq}$ is the Von Mises equivalent stress and $R_\upsilon$ is the triaxiality function. The expressions are following.

$$R_\upsilon = \frac{2}{3}(1+\upsilon) + 3(1-2\upsilon)\left(\frac{\sigma_H}{\sigma_{eq}}\right)^2 \tag{5.37}$$

$$\sigma_H = \frac{1}{3}\sigma_{kk} \tag{5.38}$$

$$\sigma_{eq} = \left(\frac{3}{2}\sigma_{ij}^D \sigma_{ij}^D\right)^{\frac{1}{2}} \tag{5.39}$$

### 3.4.3 Damage prediction in deep drawing

The damage predictions are studied by FORGE and compared with real experiment result. The default damage model used in FORGE is Cockroft & Latham model, but the prediction is not precise without considered deformation history. And the softening behavior is obvious for magnesium alloy warm forming especially at higher temperatures, but this model can not be predicted in softening stage. So, Lemaitre damage model are then studied in FORGE, the parameters are identified by tensile tests using an inverse analysis. The parameters to be identified are damage exponent *s*, damage strength $S_d$ and $\varepsilon_D$ which is the strain threshold for damage. The behavior law chosen for the simulation is defined as same as tensile test identification Gavrus model. The expression is following.

$$\bar{\sigma} = k(\bar{\varepsilon} + \varepsilon_0)^n \cdot \exp(\beta / T) \cdot \exp\left[-(r_0 + r_1 \times T) \times \bar{\varepsilon}\right] \cdot \dot{\bar{\varepsilon}}^{(m_0 + m_1 \times T)} \tag{5.40}$$

Fig.15 shows the load-displacement curves for experiment and simulation with the Lemaitre damage model in tensile test. The parameters in Lemaitre damage model are then identified, and are used directly in deep drawing test simulation based on the assumption that the damage mechanism is not variable with different forming process for same material.

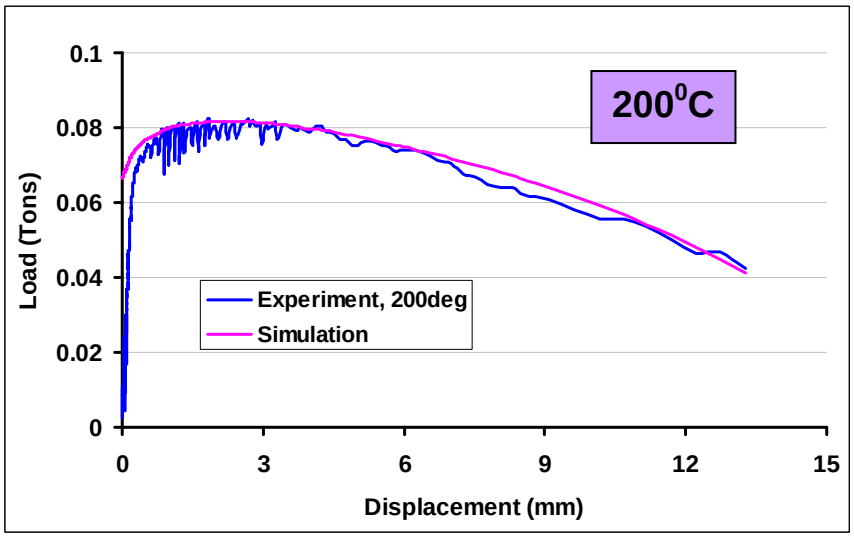


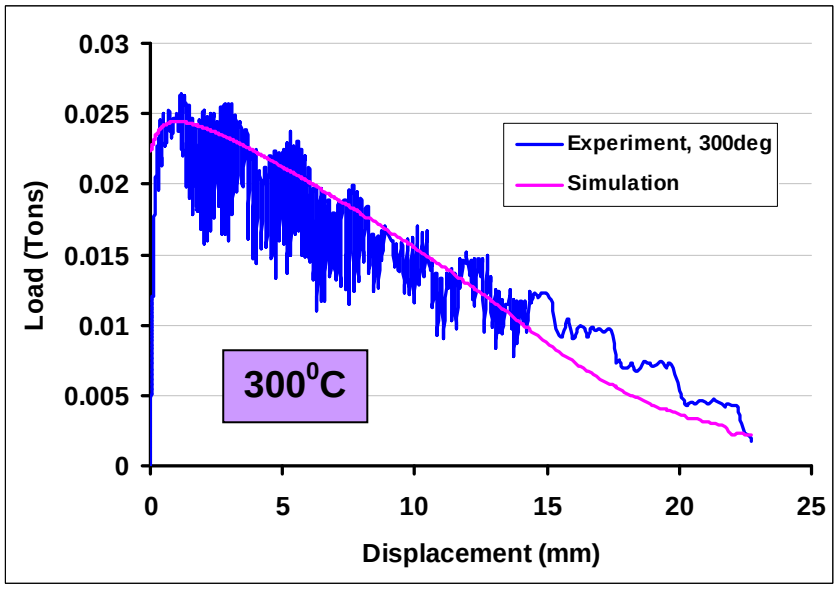


Fig.15. Comparison between experiment and simulation with Lemaitre damage model in tensile test ($\dot{\varepsilon}$=0.01s$^{-1}$).

Based on the identified parameters from tensile test simulation, i.e., damage exponent *s*, damage strength $S_d$ and damage strain threshold $\varepsilon_D$, the damage parameters in various forming conditions are then used in the deep drawing forming limit simulations. As for the identification of critical damage value *D,* the various strain path are simulated as same as real experiment in deep drawing simulation. The value *D* is identified based on the equivalent strain comparison from experiment and simulation. The value is obtained in the simulation when the equivalent strain approximately equal real equivalent strains from experiment. Finally, the damage value *D* at various strain paths is obtained from simulation. Fig.16 shows the value *D* obtained from simulation and display on the experimental FLCs.

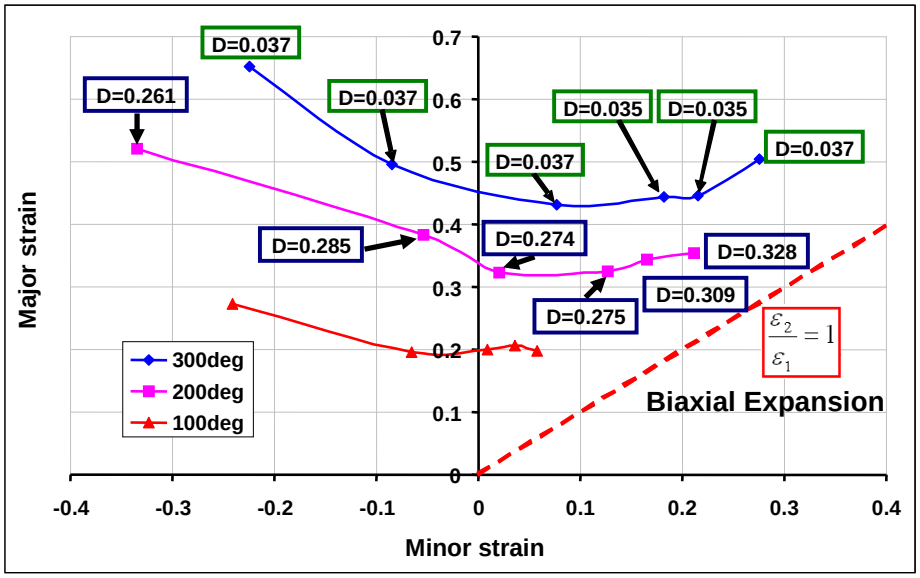


Fig.16. Damage parameters from forming limit simulation and compared with experimental FLD.

Fig.17 shows the comparison of *D* value with deformation path at the 200$^0$C and 300$^0$C. It is clearly observed that the damage value is lower at higher temperatures. It means the voids defect and volume variation decrease with temperature increasing. It is because the material plasticity improves with temperature increasing, and it is more difficult happening damage. And there is no obvious fluctuation for *D* value at each temperature. At 200$^0$C, the *D* value is a little variable for different strain, and the value is almost straight line at 300$^0$C. The damage is more stable at higher temperature.

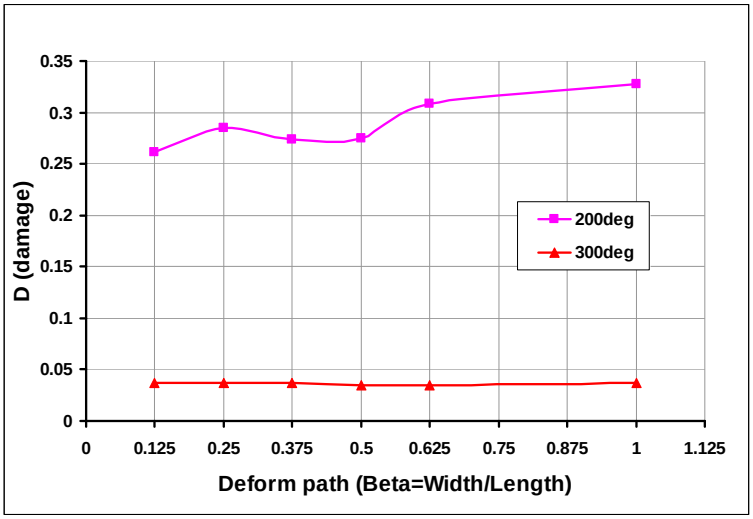


Fig.17. Damage value *D* for various strain paths at different temperatures.

The relationships of dome height and strain path are also compared by simulations. Fig.18 shows the dome height for various strain paths at 200$^0$C and 300$^0$C. The dome height

is not variable dramatically for various strain paths at $200^0$C. And the dome height is higher at $300^0$C than that at $200^0$C for each strain path. But there is some slight fluctuation for the dome height at $300^0$C. Because the material plasticity is better at higher temperature for each strain paths, and the deep drawing process is sensitive with high temperature. It is necessary to study deeply material plasticity at this temperature.

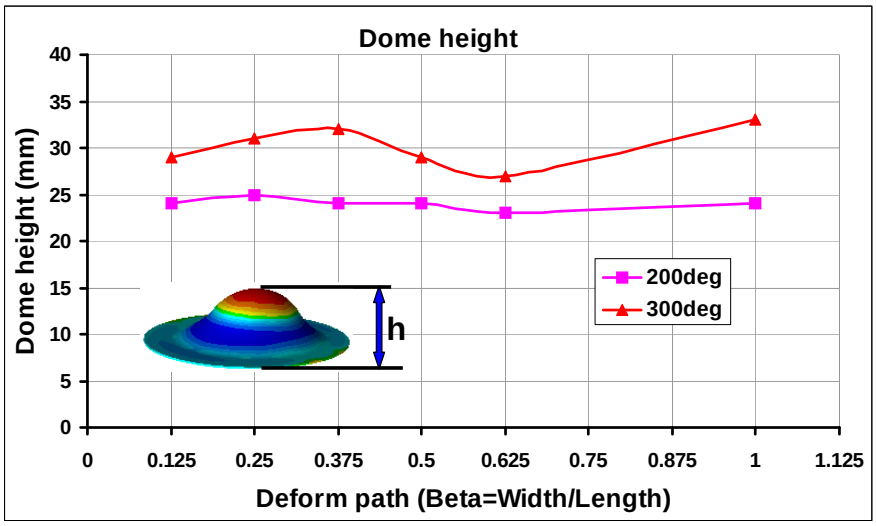


Fig.18. Dome - height for various strain paths.

# 4. Cross-shaped cup deep drawing simulation

The cross-shaped cup deep drawing simulation is the second benchmark of 8th NUMISHEET conference. The objective of this benchmark is to validate the capability of numerical simulation for a warm forming process [26]. Fig.19 shows this real cross-shaped cup deep drawing specimen, and the schematic view of tools is also shown in this figure, the pad is used to keep the bottom of cup flat.

As for the requirements, the simulation of this warm forming process should be a coupled thermal-deformation analysis considering the effect of temperature and strain-rate on material properties, particularly for stress-strain curves. For simplicity, the surface temperatures of all tools, whether heated or cooled, are assumed constant during the forming process, although this is not real case. At the beginning of forming process, the blank contact with all tools, its lower surface with the punch and the blank holder, and the upper surface with the pad (counter-punch) and the die. The punch does not start to move up until the temperature distribution in the blank reach a steady state.

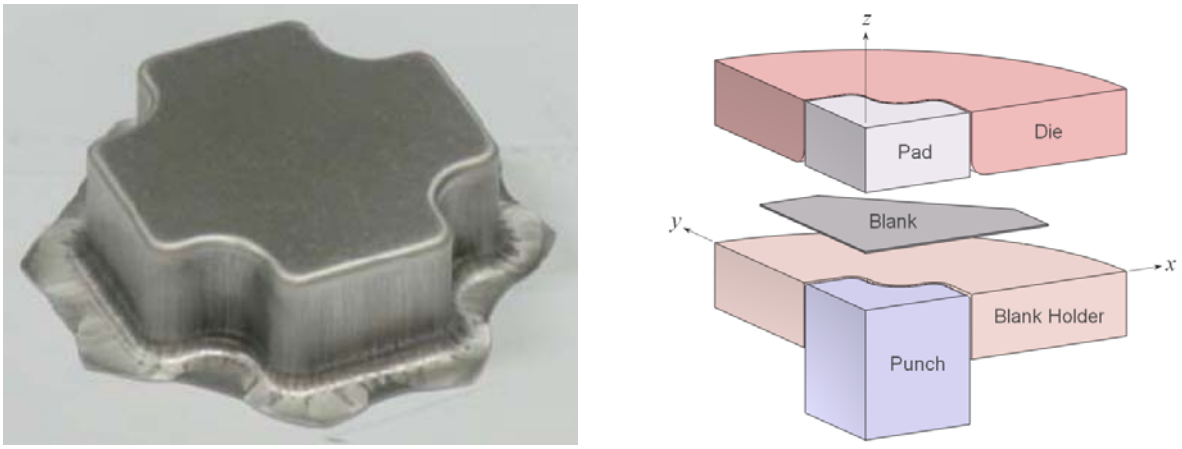


Fig.19. The cross - shaped cup deep drawing specimen and the schematic view of tools.

## 4.1. The model

This cross-shaped cup deep drawing simulations are conducted in FORGE. The geometry is just constructed quarter model about the Z-axis because of axisymmetric deformation mode. Fig.20 shows the layouts of simulation with the quarter model. In order to study the meshing influence, various meshed blanks are tested in simulations, and the thickness distribution is measured with two integration points along thickness direction. The material and the tools specification will be presented detailed in follows.

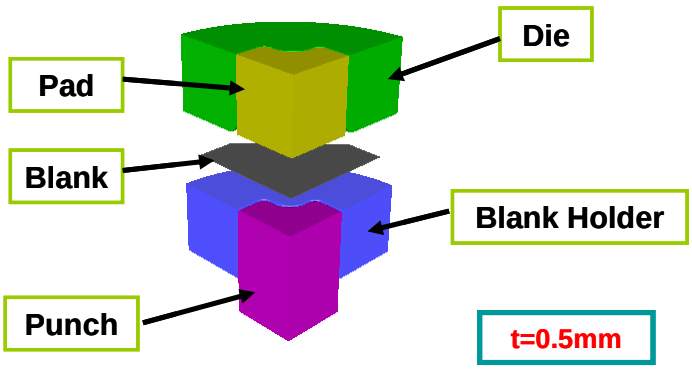


Fig.20. Quarter model used in FORGE.

As presented in the former chapter, the general technical descriptions of FORGE are shown in table.3. The element type in FORGE is volumic tetrahedron, and the standard uniform remeshing is used in forming process. The Coulomb friction model is used to simulate friction between blank and tools. The anisotropy properties are simulated with Hill'48 anisotropic criterion. The failure prediction model is default volumic failure model in FORGE, and it is used in deep drawing simulation instead of Lemaitre damage model because of application simplicity.

Table.3. General technical description of FORGE

| | |
|---|---|
| Element type: | Volumic tetrahedron |
| Contact property model: | Penalized explicit contact |
| Friction formulation: | Coulomb explicit formulation |
| Yield function/Anisotropy model: | Hill'48 anisotropic criterion |
| Failure prediction model: | Volumic failure model |
| Heat transfer model (Blank-tool interface): | Fourier thermal exchange model |

## 4.2 The material

All the tool parts are made of hardened tool steel SKD11. All surfaces which come in contact with the blank are to be ground with the surface roughness ($R_a$) less than 5 μm. The detailed material information can be founded in the conference handbook [27].

The blank material is AZ31B magnesium alloy sheet with the thickness of 0.5 mm. The initial blank has an octagonal shape. The material data used in simulation are from tensile test and transferred directly to FORGE using for point to point material model. The anisotropy data are also supported by conference and the R-values from uniaxial tension test are shown in table.4. Meanwhile, the mechanical and thermal properties are shown in table.5.

Table.4. Uniaxial tension test: R-value data [27]

| | Strain rate : 0.016 /s | | | | | |
|---|---|---|---|---|---|---|
| Test direction | Temperature [℃] | | | | | |
| | RT | 100 | 150 | 200 | 250 | 300 |
| 0° | 1.347 | 2.006 | 1.291 | 1.621 | 1.344 | 1.374 |
| 45° | 2.793 | 2.412 | 1.976 | 2.118 | 1.532 | 1.477 |
| 90° | 4.109 | 4.406 | 3.189 | 2.672 | 1.799 | 1.881 |
| Mean | 2.760 | 2.809 | 2.108 | 2.132 | 1.552 | 1.552 |

Table.5. Mechanical and thermal properties [27]

| | |
|---|---|
| Young's modulus | 45GPa |
| Poisson's ratio | 0.35 |
| Density | 1770kg/$m^3$ |
| Thermal conductivity | 96 W/(m.$^0$C) |
| Heat capacity | 1000 J/(kg.$^0$C) |
| Coulomb friction coefficient | 0.10 |
| Interface heat transfer coefficient | 4500 W/($m^2$.$^0$C ) |

## 4.3 Machine and tool specification

In order to maximize the deep drawability of the blank material, the die and the blank-holder are heated by heating cartridges embedded in each tool, while the punch and the pad are cooled by circulating water. Process parameters are as follows:

1) Surface temperature of the die and the blank-holder: $250^0$C

2) Surface temperature of punch and pad: $100^0$C

3) Punch velocity: 0.15 mm/s

4) Blank-holder force: 1.80 to 3.96 kN (linearly increases as shown in Fig.21.(a))

5) Pad force: 0.137 to 2.603 kN (linearly increases as shown in Fig.21.(b))

6) Lubricant: Teflon tape (for high temperature)

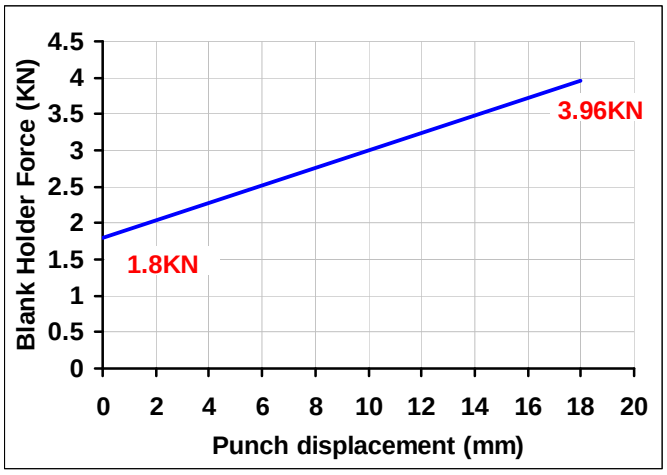


(a) Blank holder force

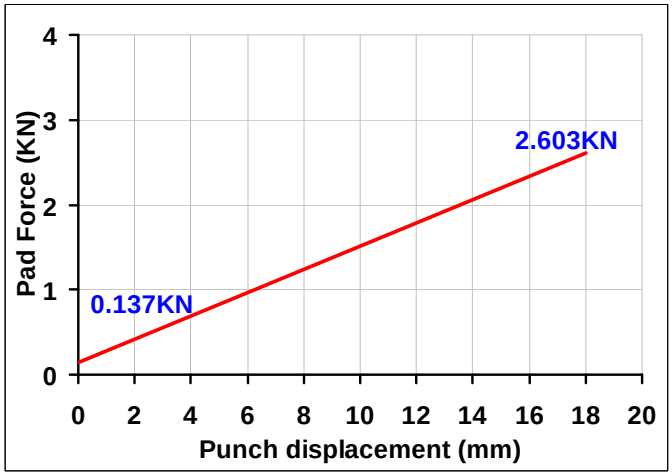


(b) Pad force

Fig.21. Variation of the blank holding force and pad force.

## 4.4 Result analysis

As for requirement of benchmark, the punch load, thickness and temperature distribution are obtained at each simulation. The thickness and temperature distribution are compared in the formed part along the 0°, 22.5°, 45°, 67.5° and 90° directions from the rolling direction at various punch displacements. Meanwhile, the punch load and thickness distribution curves are plotted and compared with results obtained from other simulation software. The meshing influence is also studied in simulation with various mesh sizes.

### 4.4.1 Thickness and temperature distribution

Thickness distributions are available in simulation at the punch displacement of 10mm and 18mm (Fig.22). It is obviously shown that the thickening occurs at flange zone and thinning at cup wall zone. The maximum thinning is observed at the die corner radius for both punch displacement which is contrary to the conventional stamping where the maximum thinning is obtained at punch radius zone. It is probably due the strength of the cup wall in this stamping forming is not uniform as in conventional isothermal stamping. Fig.23 shows the blank temperature distribution at various punch displacement. As the stamping is non-isothermal, the temperature distributes gradually along the wall. And similar phenomena are observed during all of processing, there are no obvious temperature changes at the punch radius and die radius zone. In the temperature distribution, the initial die and blank holder temperature ($250^0$C) are higher than the punch and pad temperature ($100^0$C). Therefore, the yield strength of the material at the die corner radius is lower compared to the material at punch corner caused thinning in the cup wall. The thickness distribution is sensitive with the temperature, and the plasticity improves dramatically with temperature increasing.

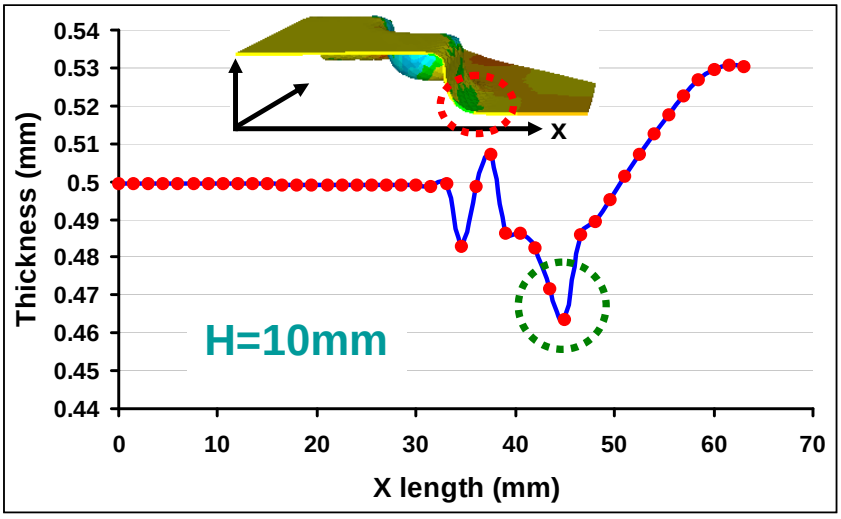

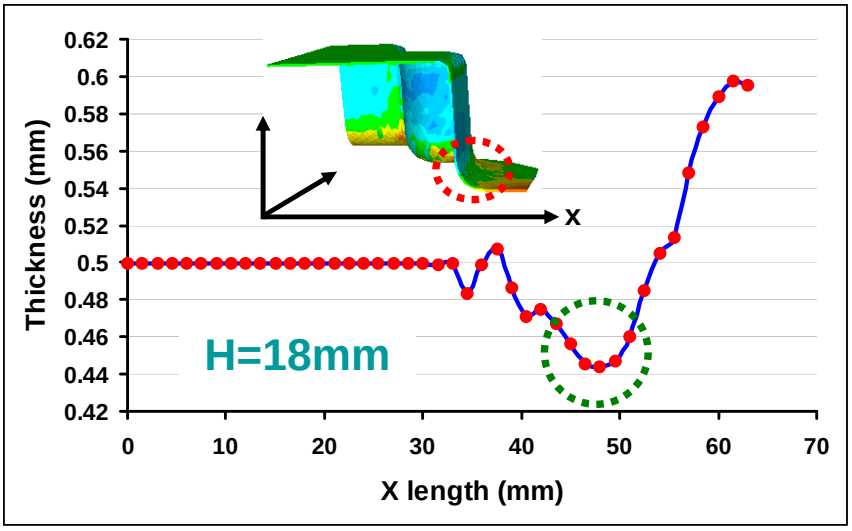


Fig.22. The thickness distribution along center line at the various punch displacement (RD).

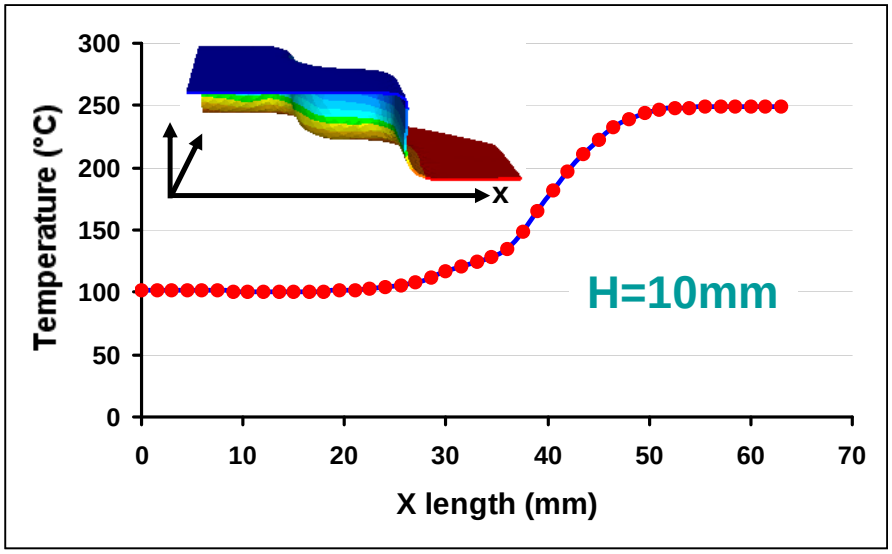


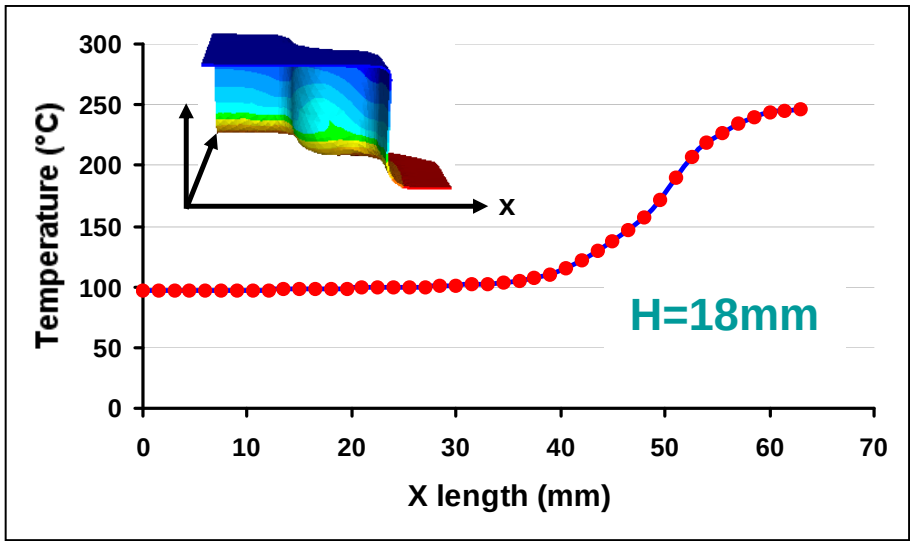


Fig.23. The blank temperature distribution along center line at the various punch displacement [RD].

### 4.4.2 Punch load analysis

The punch loads obtained from simulation are shown in Fig.24. The punch loads have not much difference with various meshing size, and there is slight fluctuation at each punch force curve, especially at high displacement. The possible reason is the temperature does not distribute uniformly during forming processing, the force distribution is fluctuated correspondingly. And other possible reasons are the boundary condition and contact changes which play an important role in simulation.

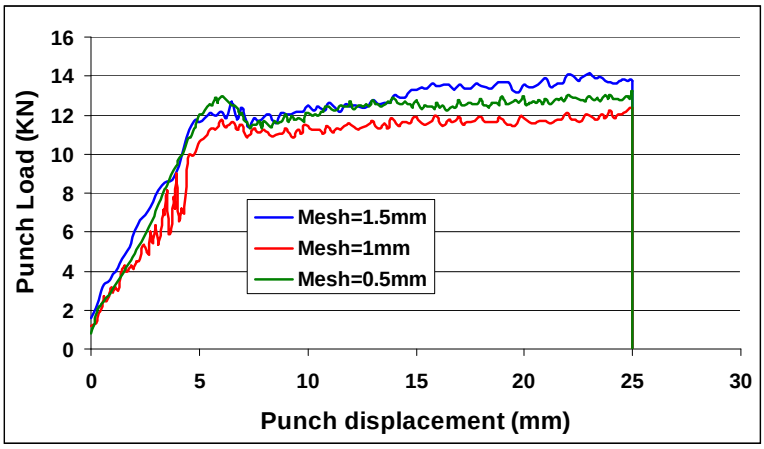


Fig.24. Punch load and displacement curves at various meshing.

### 4.4.3 Meshing analysis

The total CPU time in finite element simulation is sensitive with meshes. The simulation have been conducted with four cores CPU in this project. Fig.25 shows the CPU time comparison with various mesh size. It is clearly shown that the CPU time increase dramatically with the mesh size decreasing, meanwhile the node and element is increased correspondingly.

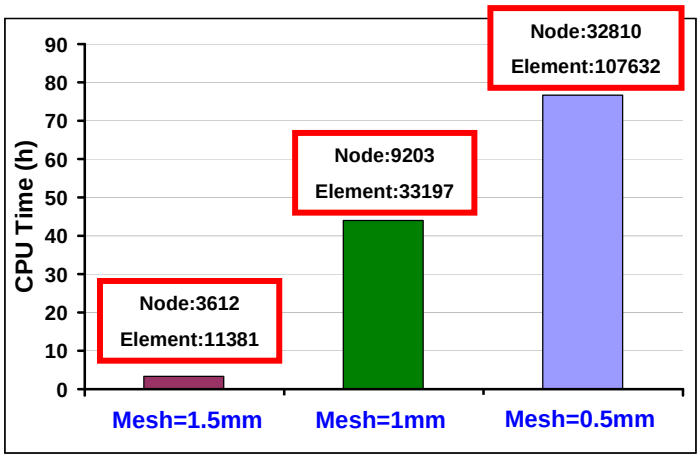


Fig.25. The CPU time with various mesh size.

The mesh size plays an important role in finite element simulation. Not only the blank mesh but also tool meshes have influence for total CPU time in simulation. Fig.26 and Fig.27 shows the comparison of the simulation with coarse mesh and finer mesh. The Total CPU time is decreased dramatically with coarse mesh and the volume variation is smaller correspondingly. It is the reason that it takes more times to keep convergence with finer mesh, and more iteration cost volume variation.

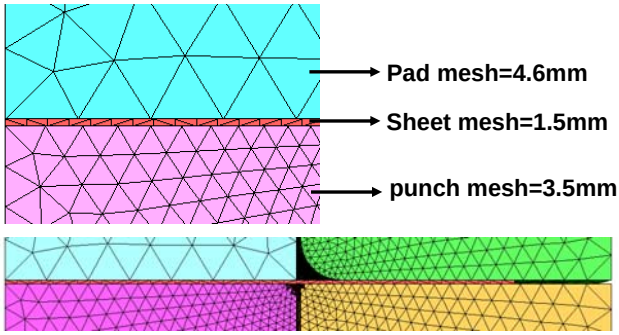


**Total CPU**
**1 h 44' 49"** s

**Volume variation:**
**0.616 %**

Fig.26. The simulation with coarse mesh.

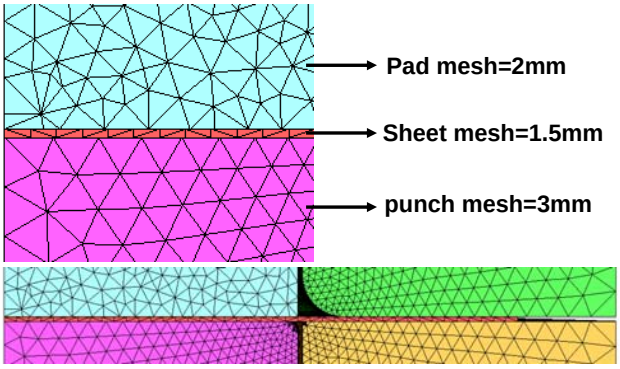


**Total CPU**
**5 h 40' 11"** s

**Volume variation:**
**2.601** %

Fig.27. The simulation with finer mesh.

## 4.5 Result comparison

This cross-shaped cup deep drawing benchmark results are compared with various simulation software in conference. The comparison with punch load, thickness distribution and temperature distribution are studied completely. Six results using various finite element solvers are compared with reference result. Various solving method, such as explicit (LS-Dyna, Radioss, JSTAMP, Dynaform) and implicit (ABAQUS, FORGE) method, are both used in this case. The CPU time is also compared in this case, and the explicit method takes less time than implicit method. Because the implicit method is based on amount of iteration, the solving time is longer than explicit method. As presented in finite element theory, the

disadvantage of explicit method is the conditional stability, the each time increment must be less than critical time step which determined by the system highest natural frequency [27].

### 4.5.1 Punch load

The punch loads from the various simulations are compared. Fig.28 shows the punch loads with punch stroke when the friction coefficient equal 0.1. The results vary with different finite element code. The reference curve is higher than the most curves, but all of result tendency is same that the punch load increase with punch stroke increasing until stable condition. The punch load result with Dynaform software is worse than others, and the result point is less to analyze the reason. The punch load result from FORGE is higher than the reference result. It is probably because the material data used in simulation is real tensile test data after mathematic fitting, and the friction is probably overestimated in the simulation. In sum, the punch load results from various simulations are close each other and match with reference.

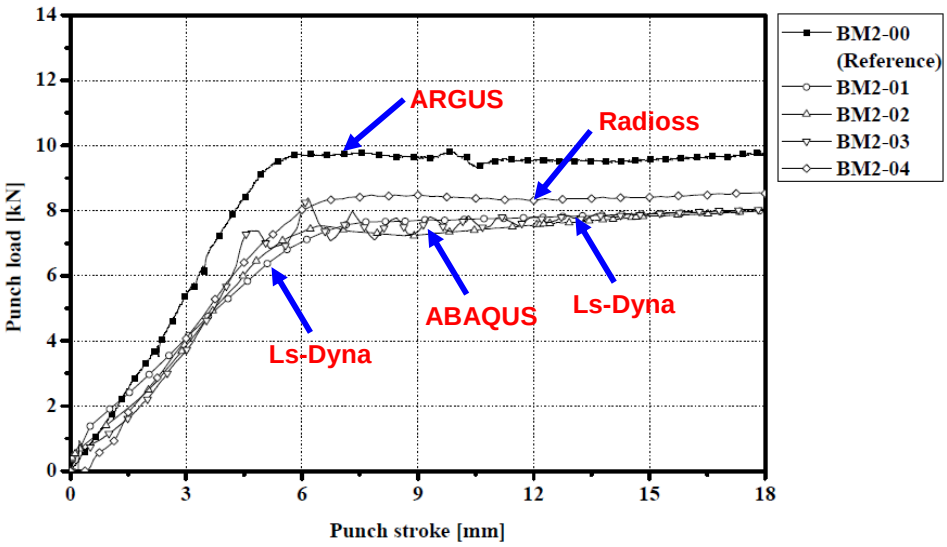

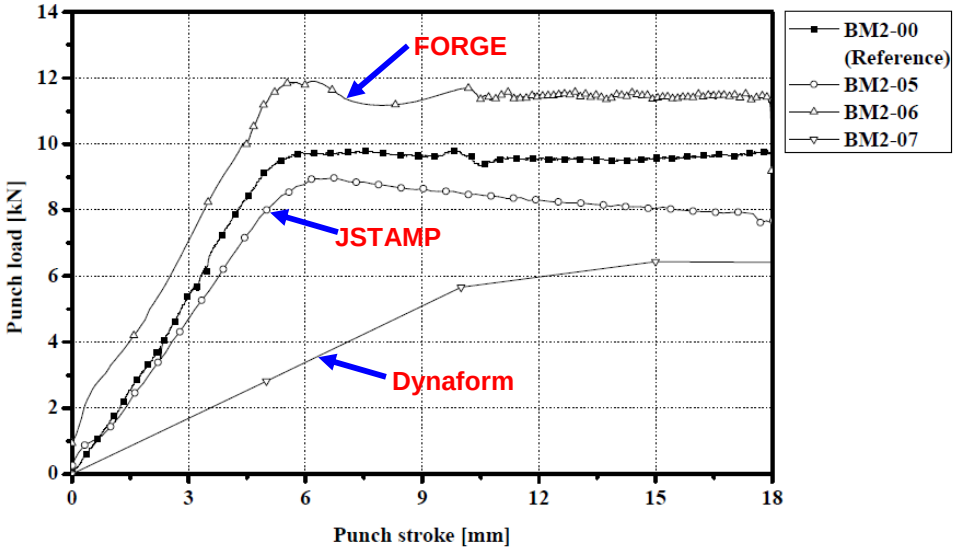


Fig.28. Punch load vs. punch stroke during the drawing process (μ=0.1) [27].

### 4.5.2 Thickness distribution

The thickness distribution from the various simulations is compared deeply. Fig.29 and Fig.30 show the thickness with travel length from the center toward the edge along the $0^0$ and $45^0$ directions with respect to the rolling direction. The results are close with different finite element code. Most of simulation predicts the thinning in wall area and thickening in flange area. The initial thickness of blank is 0.5mm, the thickness almost keep constant in the flat area. The reference curve simulated about 20% maximum thinning in the simulation, it is higher than the most curves. The thickness result with Dynaform software is worse than others, and the ABAQUS result predict unusual thickness distribution which the thickening happen at the wall area. The thickness result from FORGE is close with other simulations.

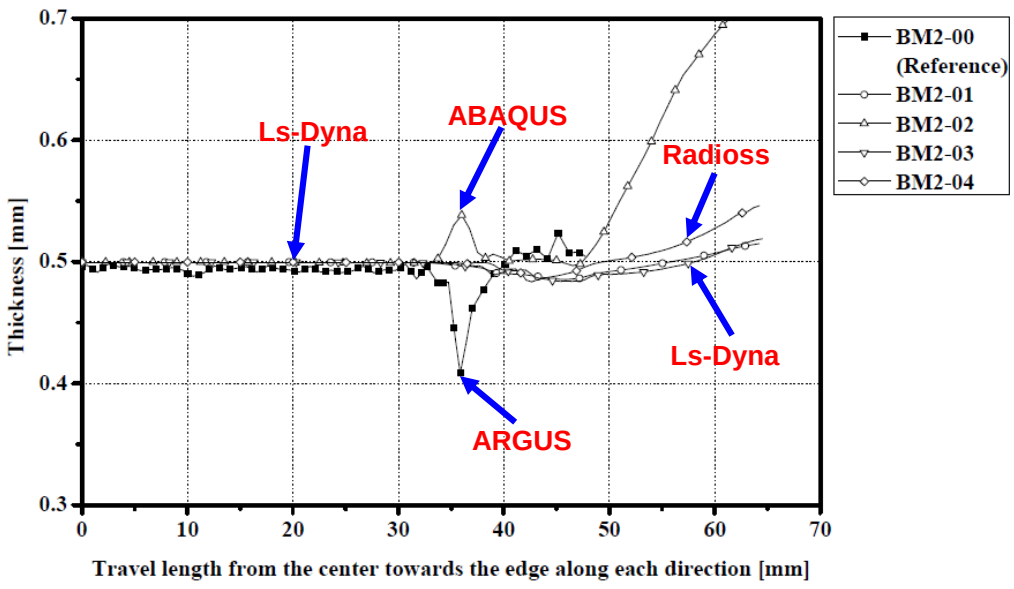

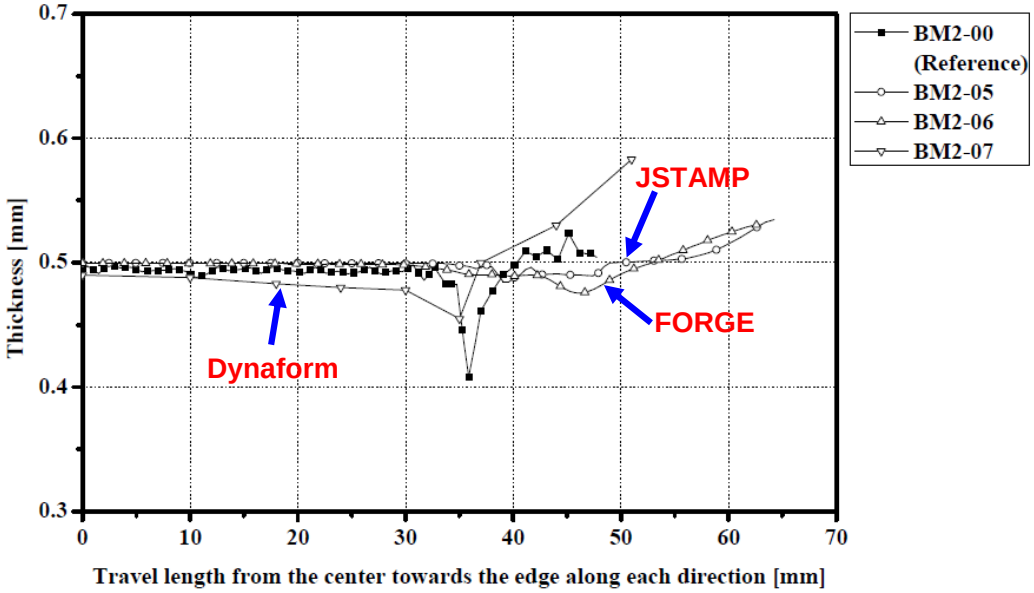


Fig.29. Thickness vs. Travel length from the center toward the edge [27].

(Punch stroke = 10mm, angle from the rolling direction $\theta = 0^0$)

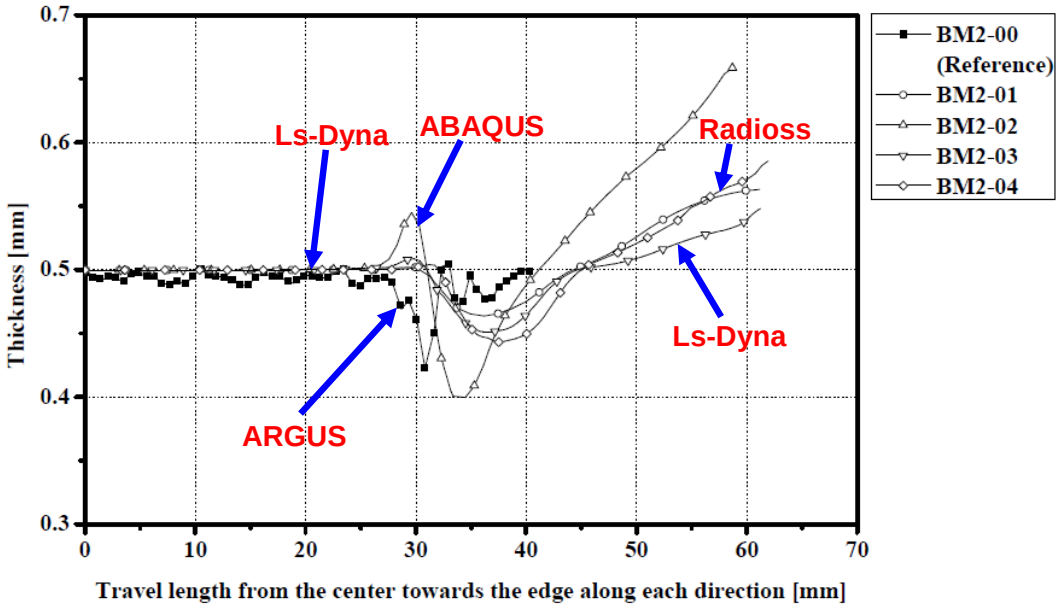

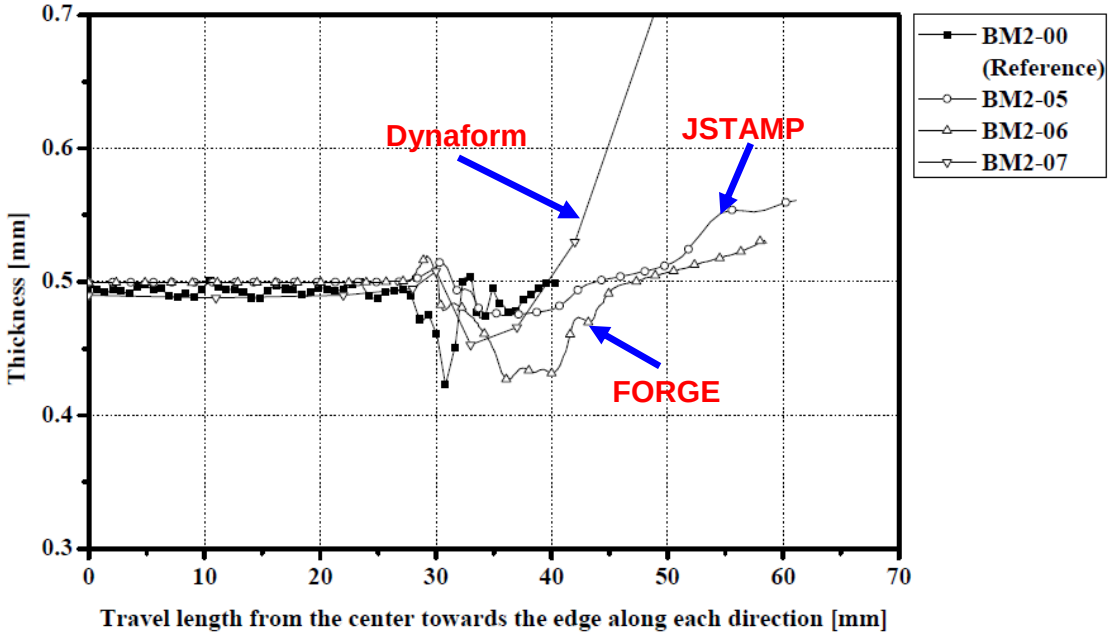


Fig.30. Thickness vs. Travel length from the center toward the edge [27].
(Punch stroke = 10mm, angle from the rolling direction $\theta = 45^0$)

# 5. Conclusion

In this chapter, the finite element simulations have been deeply studied to validate the forming process. Firstly, the hemisphere punch deep drawing simulations are carried out in FORGE and ABAQUS. This simulation conditions are referred completely with warm Nakazima stamping test. The purpose is to study the AZ31 magnesium alloy formability in numerical simulation. The punch force, temperature distribution and thickness distribution have been compared between simulation and experiments. The detailed analysis result have presented in result comparison section. In addition, the simulation performed by ABAQUS and FORGE are also compared to study the difference of various finite element analysis code. And then, the damage behaviors have been studied in FORGE. Two damage model, i.e., Cockcroft & Latham model and Lemaitre damage model have been used in this project. However, the Cockcroft & Latham model is not precise without considering deformation history. The parameters of Lemaitre damage model are identified from tensile test simulation, and these parameters are directly used in deep drawing simulation based on the assumption that the damage mechanism is not variable with different forming process for same material. The comparison leads to the conclusion that the damage value is lower at higher temperature, which is closed conclusion from experiment.

Secondly, a cross-shaped deep drawing cup simulation has been studied by FORGE software which is a benchmark of NUMISHEET 2011 conference. The objective of this

benchmark is to validate the capability of finite element simulation for a warm forming process. This is a coupled thermal-deformation analysis with temperature and strain rate influence. The punch load, thickness distribution and temperature distribution have been compared intensively. The details of analysis have presented in the result analysis section. Meanwhile, the results (FORGE) are also compared with other various simulation softwares in conference, such as explicit method (LS-Dyna, Radioss, JSTAMP, Dynaform) and implicit method (ABAQUS, FORGE). The detailed analysis results are presented in specific section.

# 6. References


[1] S. Kobayashi, T. Altan. Metal Forming and Finite Element Method, Oxford University Press, NY, 1989.

[2] A. H. van den Boogaard, P. J. Bolt, R. J. Werkhoven. Aluminum sheet forming at elevated temperatures. Simulation of Materials Processing: Theory, Method and Applications, 2001, pp.819-824.

[3] Giuseppe Pelosi. The finite-element method, Part I: R. L. Courant: Historical Corner. Antennas and Propagation Magazine, IEEE , 2007.

[4] Web:http://en.wikipedia.org/wiki/Finite_element_method. Finite element method, 2011.

[5] S. S. Rao. The finite element method in engineering. Butterworth-Heinemann, 2005.

[6] K. J. Bathe. Finite element method. Wiley Online Library, 2007.

[7] T. J. R. Hughes. The Finite Element Method: Linear Static and Dynamic Finite Element Analysis. Prentice-Hall, 1987.

[8] O. C. Zienkiewicz, R. L. Taylor. The finite element method for solid and structural mechanics. Butterworth-Heinemann, 2005.

[9] B. S. Thomas. A general forming limit criterion for sheet metal forming. International Journal of Mechanical Sciences, Vol.42, Issue 1 (2000), pp.1-27.

[10] I. Babuska. The finite element method with Lagrangian multipliers. Numerische Mathematik. Volume 20, Number 3 (1973), 179-192.

[11] I. Babuska, A. K. Aziz. Lectures on mathematical foundations of the finite element method. Technical Report, 2008.

[12] N. Sukumar, N. Moës, B. Moran, T. Belytschko. Extended finite element method for three-dimensional crack modeling. International Journal for Numerical Methods in Engineering, Vol.48, Issue 11 (2000), pp.1549-1570.

[13] M. A. Crisfield. Nonlinear finite element analysis of solids and structures. Wiley, New York, 2008.

[14] J. M. Duncan. State of the art: Limit equilibrium and finite-element analysis of slopes. Journal of geotechnical engineering, Vol.122, Issue 7 (1996), pp.577-596.

[15] FORGE software documentation-data file. 2009.

[16] R. Knockaert. Numerical and experimental study of the strain localization during sheet forming operations. PhD thesis, Ecole de mines de paris - CEMEF, Sophia-antipolis, France, 2001.

[17] S. Novel. Etude de l'adaptation de logiciel forge aux produits minces. Technique report,

Ecole de mines de paris - CEMEF, Sophia-antipolis, France, 1998.

[18] K. Droder. Analysis on forming of thin magnesium sheets, Ph.D.Dissertation, IFUM, University of Hanover, 1999.

[19] S. L. Semiatin, E. W. Collings, V. E. Wood, T. Altan. Determination of the interface heat transfer coefficient for non-isothermal bulk forming process. Journal of Industrial Engineering, 109 (1987), pp.49-57.

[20] S. H. Kim, H. W. Lee, S. Choi. Experimental and analytical studies on mechanical properties and formability of AZ31B magnesium alloy sheet. In: Proceedings of the ESAFORM, 2008, pp.149-154.

[21] H. Palaniswamy, G. Ngaile, T. Altan. Finite element simulation of magnesium alloy sheet forming at elevated temperatures. Journal of Materials Processing Technology, 146 (2004), pp.52-60.

[22] J. Lemaitre, R. Desmorat, M. Sauzay. Anisotropic damage law of evolution. European Journal of Mechanics A/Solids, Vol.19 (2000), pp.187-208.

[23] H. Takuda, K. Mori, N. Hatta. The application of some criteria for ductile fracture to the prediction of the forming limit of sheet metals. Journal of materials processing technology, 95 (1999), pp.116-121.

[24] J. Lemaitre, J. P. Sermage. One damage law for different mechanisms. Computational Mechanics, 20 (1997), pp.84-88.

[25] J. Lemaitre, J. P. Sermage, R. Desmorat. A two scale damage concept applied to fatigue. International Journal of Fracture, 97 (1999), pp.67-81.

[26] Z. G. LIU, E. Massoni, P. Lasne. Benchmark 2: Simulation of the Cross-shaped Cup Deep-drawing Process. The 8th Internatinal Conference and Workshop on Numerical Simulation of 3D Sheet Metal Forming Processes. Seoul, Korea. 21-26 August, 2011.

[27] Benchmark Study, the 8th International Conference and Workshop on Numerical Simulation of 3D Sheet Metal Forming Processes. PART C: Benchmark Problems and results. Seoul, Korea. 21-26 August, 2011.

# Chapter 6 Conclusions and perspectives

In the thesis, the ductility and formability of AZ31-O magnesium alloy are studied extensively in experimental and numerical aspect. The magnesium alloy provide low ductility for cold forming operation due to HCP (Hexagonal Close-Packed) crystal structure. The formability is improved obviously at elevated temperature. So, the experiment and numerical simulation are conducted for warm forming process. In this chapter, conclusions are presented and perspectives are given for further research.

## Experimental studies

### Warm forming test

Warm tensile tests have been performed at various temperature and strain rate by Instron tensile test machine. The ARAMIS strain measurement system is used to measure material deformation. The temperatures and strain rates influence are considered in these experiments. Finally, the analysis result shows higher yield stress and smaller elongation at room temperature with higher strain rate, but it improves significantly with temperature increasing and strain rate decreasing. Three different specimens are used with various orientations with respect to the rolling direction in order to study material anisotropy property. The experiment results obviously indicate that the material shows anisotropy in lower temperature, but anisotropy decrease with temperature increasing and it is not obvious over 200°C. So, the anisotropic property is not considered in this project. The true stress and true strain data are derived from the load stroke data initially getting from experiment. And these data are used to identify constitutive equation in the project.

Warm Nakazima tests (hemisphere punch deep drawing test) in various temperature and strain rate are performed using six geometries specimens. These tests are performed in laboratory with Dartec tension-compression hydraulic testing machine. Each specimen represents a strain path. Three temperatures and two test velocities are considered. The purpose is to study material forming limits. The ARAMIS system is also used to obtain the principal strains (major strain and minor strain). Three types of stamped blanks are obtained after experiment, which are safe, necking and fracture specimens respectively. Finally, The FLDs (Forming Limit Diagram) with fracture specimens are obtained and the results distinctly show that the material formability is better at higher temperature. The experimental

influence parameters have taken into account in order to analyze their respective influence on formability, e.g., temperature, process speed, lubrication and strain path, etc. The analysis results have presented in the thesis. The conclusion is higher temperature and lower strain rate, the better formability of material.

# Numerical studies

## Material modeling

The constitutive equation is identified with stress and strain data in MATLAB Genetic Algorithm (GA) toolbox. Firstly, it is analyzed by power law type equation which just include strain hardening exponent $n$ and strain rate exponent $m$. And it can only fit well with experimental curves at the strain hardening stage. So, a new mathematical model is studied to describe the softening behavior of material. That is Gavrus law including 8 parameters and two parts to describe the hardening and softening behaviors, and the related parameters are obtained by fitting the equation with the experimental data. The genetic algorithm has been used to obtain the global optimal fitting parameters. The comparison between the fitted and experimental data proves the effectiveness of the model.

## Forming limits prediction modeling

The forming limits predictions are carried out in M-K model which is a widely used prediction model in application. The prediction FLD with M-K model have compared with experiment FLD at various temperature and imperfection status. It is clearly shown that the curves which appeared near the plane strain state fit much better than another area. And the curves fit better at $300^0$C, it is probably because M-K model calculate the localized necking limit strains when the specimens appeared broken, and the localized necking strain is close the fracture strain at high temperature. However, the tendencies of experimental and theoretical FLD both clearly indicate that the formability is better at higher temperature.

## Finite element modeling

Firstly, the hemisphere punch deep drawing simulations are performed in FORGE and ABAQUS. The same models are used in simulation and experiment. Punch forces, temperature and thickness distributions are compared between simulations and experiments. The punch load results indicate that the simulation curves are higher than experimental curves. There are probably several reasons to explain the discrepancies, such as friction, material

properties, heat transfer and isotropy properties, etc. The temperatures located at the punch radius zone are higher than another zone during the process. In the thickness distribution, maximum thinning has been observed in punch radius zone for both simulation and experiment. However, less thickening and more thinning has been observed in the simulation as compared with experiments. It is probably because the strength of the punch radius zone in warm forming is not uniform and depends on the temperature distribution which is higher in punch radius zone at all stroke positions. The simulation conducted in FORGE and ABAQUS are compared in order to study the validation of finite element simulation. The comparison shows that the curve from simulation is higher than experimental curve. And the discrepancy between simulation and experiment is different in this two simulation software. The discrepancy increases with temperature in ABAQUS. It is probably because the friction is sensitive with temperature increasing.

Secondly, the damage behavior are studied in FORGE, the default damage model is Cockcroft & Latham model. The damage prediction with this model is not precise because it does not consider the deformation history. Since the Lemaitre damage model with several damage parameter is introduced in FORGE. The damage parameters obtained from warm tensile test simulation are used in deep drawing simulation, the damage value $D$ are obtained from each simulation. The damage values with deformation path are compared at $200^0$C and $300^0$C. It is clearly shown that the damage value is lower at higher temperatures, and there is no obvious fluctuation for $D$ value at each temperature. The dome height with deformation path shows similar conclusion. The dome height is not variable dramatically for strain paths at $300^0$C, but there is some tiny fluctuation for the dome height at $200^0$C.

Finally, the Cross-shaped deep drawing cup simulations are performed with FORGE. The simulation is a benchmark of NUMISHEET 2011 conference. The objective of this benchmark is to validate the capability of numerical simulation for a warm forming process. This warm forming process simulation is a coupled thermal-deformation analysis considering the effect of temperature and strain-rate on material properties. The punch load, thickness and temperature distribution are obtained at each simulation. The thickness and temperature distribution are compared in the formed part along the 0°, 22.5°, 45°, 67.5° and 90° directions with respect to the rolling direction at various punch displacements. The punch load and thickness-displacement curves are plotted and compared with results obtained from other simulation software. The meshing influence is also studied in simulation with various mesh sizes. In the punch load comparison, the punch loads have not much difference with various meshing size, and there is slight fluctuation at each punch force curve especially at high

displacement. For the thickness and temperature distribution, the thickening occurs at flange zone and thinning at cup wall zone. The maximum thinning is observed at the die corner radius for both punch displacement which is contrary to the conventional stamping where the maximum thinning is obtained at punch radius zone. The temperature distributes gradually along the wall during forming process. And there are no obvious temperature changes at the punch radius and die radius zone. The meshing influences are also analyzed by comparing total CPU time, The Total CPU time is decreased dramatically when the tool mesh is finer keeping same scale with blank mesh and the volume variation is smaller correspondingly.

This benchmark simulation results (FORGE) are also compared with various simulation software in conference, such as explicit method (LS-Dyna, Radioss, JSTAMP, Dynaform) and implicit method (ABAQUS, FORGE). The CPU time is also compared in this case, and the explicit method takes less time than implicit method. Because the implicit method is based on amount of iteration, the solving time is longer than explicit method. In the punch load comparison, the results vary with different finite element code. The reference curve is higher than the most curves, but all of result tendency is same that the punch load increase with punch stroke increasing until stable condition. For the thickness distribution comparison, two kind of curves are compared which is the thickness with travel length from the center toward the edge along the $0^0$ and $45^0$ directions with respect to the rolling direction. The results are close with different finite element code. Most of simulation predicts the thinning in wall area and thickening in flange area. The initial thickness of blank is 0.5mm, the thickness almost keep constant in the flat area. The reference curve simulated about 20% maximum thinning in the simulation, it is higher than other curves.

# Perspectives

Firstly, the magnesium alloy property includes the hardening and softening. The softening behaviors are obvious at high temperature and it is very difficult to describe the softening deformation in suitable constitutive equations. The power law can only fit the hardening, and the Gavrus law can describe softening behavior with unsatisfied discrepancy. It is a possible way to take into account the evolution of microstructure and introduce microstructure parameters into the constitutive equation.

Secondly, the forming processes of AZ31 magnesium alloy are carried out in warm environment. The experiment tests are difficult to perform, especially for the strain measurement system. There are not very good strain measurements solutions for warm

forming test at present. Because the necking phenomenon is very obvious for AZ31 and the pattern is easy to disappear with large deformation at higher temperature. So, the warm forming experiments are necessary to be improved in the future.

Finally, the deep drawing simulation is difficult to perform with optimal parameters such as friction, heat exchange, material model and damage model, etc. There are still many dissatisfactory during finite element simulation in sheet metal forming. The discrepancies between the simulation and experiment must be decreased. The damage model is also difficult to use appropriately in warm forming simulation. So, it is still the way to improve the finite element method used in sheet metal forming process.

# Annex 1: Gavrus constitutive model identification

In this project, the Gavrus constitutive model has been identification by Matlab genetic algorithm (GA) toolbox. The equation is explicitly expressed as follows:

$$\bar{\sigma} = k(\bar{\varepsilon} + \varepsilon_0)^n * \exp(\beta / T) * \exp(-(r_0 + r_1 * T) * \bar{\varepsilon}) * \dot{\bar{\varepsilon}}^{(m_0 + m_1 * T)} \qquad \text{(annex.1)}$$

The detailed explanations of parameter have been presented in chapter 3. the objective function is expressed as follows:

$$O(f) = \frac{\sum_i^n (\sigma_i^{\exp} - \sigma_i^{cal})^2}{\sum_i^n (\sigma_i^{\exp})^2} \qquad \text{(annex.2)}$$

Finally, the following fitness function (fitness.m) is written by Matlab. The identification is performed based on this function.

```
function f = fitness (x)                        %function definition
  f = 0;                                        % function initialization
    for sig = [0.1, 0.01, 0.001];
       for T = [20,100,200,235,300];
          f = f + sum((sigma1(sig,T)-sigma2(sig,T,x)).^2)/sum(sigma1(sig,T).^2);      // set objective function
    end
  end
end

  function s = sigma1(sig,T)                                    % return experimental stress data
    global experiment data;                                     % import experiment data
       sel = find(data(:,4) = = sig & data(:,3) = = T);         % define the thread of location
       s = data(sel,2);                                         % find experimental stress data
  end

  function s = sigma2(sig,T,x)                                  % return calculated stress data
    global experiment data;                                     % import experimental data
      sel = find(data(:,4) = = sig & data(:,3) = = T);          % define the thread of location
      sigma3 = data(sel,1);                                     % find strain data
      s = x(1)*(sigma3.^x(2));
      s =s*exp(x(3)/T);
      s= s.*exp(-(x(4)+x(5)*T).*sigma3);
      s = s*sig^(x(6)+x(7)*T);                          % find calculated stress data
  end
```

# Annex 2: Forming limit prediction program by M-K model

The principle of M-K model have extensively discussed in chapter 4, the implementation program written by C++ is presented as follows.

```
//**************Prediction FLD.CPP **************//
#include <math.h>
#include <stdio.h>
#include <iostream.h>

// define initial material constant
#define  data_strn1b      0.01          // initialize principle strain increment Δε1b
#define  nvalue           0.02          // initialize n value
#define  mvalue           0.22          // initialize m value
#define  f                0.995         // initialize thickness ratio, f=tb0/ta0;
#define  evalue           1e-6

//define global variables
double fai_a, rou_a, beta_a, alfaa;     // define φa , ρa , βa , αa
double fai_b, rou_b, beta_b, alfab;     // define φb , ρb , βb , αb
double n_ds=1.0/nvalue;

////////////////////////////////////////////////////////////////////////////

// calculation procedure for principle strain increment in A zone Δε1a
double cmpt_dt_sn1a(double strain1a, double strain1b, double dtsn1a1)
{
        double dtsn1a2, datastrn1a;
        double diff1, diff2;

        double add=0.001;

        do
        {
                datastrn1a=cmpt(strain1a,strain1b,dtsn1a1);
                diff1=dtsn1a1-datastrn1a;

                dtsn1a2=dtsn1a1-add;

                datastrn1a=cmpt(strain1a,strain1b,dtsn1a2);
                diff2=dtsn1a2-datastrn1a;

                if(add<=evalue)
                        return(dtsn1a1);
                else
                        if(fabs(diff1)<=evalue)
                                return(dtsn1a1);
                        else
                                if(fabs(diff2)<=evalue)
                                        return(dtsn1a2);
                                else
                                        if(fabs(diff2)<fabs(diff1))
                                                dtsn1a1=dtsn1a2;
```

```
                                        else
                                                if(fabs(diff2)>fabs(diff1))
                                                        add=add/2.0;
                                                else
                                                        return(datastrn1a);
        }
        while (add>evalue);
        return(dtsn1a2);
}

////////////////////////////////////////////////////////////////////////////
double cmpt(double strn1a, double strn1b, double datastrn1a)
{
        double strn2, strnia, strnib;
        double datastrn2, datastrnia, datastrnib;
        double strn3a, strn3b;
        double fai, betarou, strn;
        double mdata, dtstrn1a;

        // strain calculation in A zone;
        strn2=rou_a*strn1a;
        strnia=beta_a*strn1a;

        datastrn2=rou_a*datastrn1a;

        strn3a=-(strn1a+strn2);
        strn3b=-(strn1b+strn2);

        // calculated stress ration and strain ratio in B zone;
        rou_b=datastrn2/data_strn1b;
        alfab=(2.0*rou_b+1.0)/(2.0+rou_b);
        fai_b=sqrt(1.0-alfab+pow(alfab,2.0));
        beta_b=2.0*fai_b/(2.0-alfab);

        // calculated equivalent strain in B zone;
        strnib=sqrt(2.0/3.0*(pow(strn1b,2.0)+pow(strn2,2.0)+pow(strn3b,2.0)));
        datastrnib=data_strn1b*beta_b;

        strnib=strnib+datastrnib;
        strn=strn3b-strn3a;

        ////////////////////////////////
        fai=fai_a/fai_b;
        betarou=(beta_b*rou_a)/(rou_b*beta_a);

        mdata=f*exp(strn)*fai*pow(strnib,nvalue)*pow(betarou,mvalue);
        datastrnia=pow(mdata,n_ds)-strnia;

        if(datastrnia<0)
                datastrnia=0.0;

        dtstrn1a=datastrnia/beta_a;

        return(dtstrn1a);
}

////////////////////////////////////////////////////////////////////////////
//main function
void main()
{
```

```
    FILE *fp;
    fp=fopen("fld_predict.txt","a+");

    double data_strn1a, datastrn1a;
    double strn1a, strn1b, strn2;
    double chazhi;

    fprintf(fp," initial thickness ration: %f\n",f);
    fprintf(fp," n value: %f\n  m value: %f\n", nvalue, mvalue);
    fprintf(fp," the minor strain and major strain in the fracture: \n");

    alfaa=0.10;                         // initialize stress ratio in A zone
    while(alfaa<1.05)
    {
            // initialize strain
            strn1a=0.0;
            strn1b=0.0;

            // assume initial strain increment in A zone
            data_strn1a=data_strn1b;            // provisional value

            fai_a=sqrt(1-alfaa+pow(alfaa,2.0));
            beta_a=2.0*fai_a/(2.0-alfaa);
            rou_a=(2.0*alfaa-1.0)/(2.0-alfaa);

            // calculated strain ratio increment in A zone
            datastrn1a=cmpt_dt_sn1a(strn1a,strn1b,data_strn1a);
            data_strn1a=datastrn1a;

            do
            {
                    strn1b=strn1b+data_strn1b;
                    strn1a=strn1a+data_strn1a;

                    datastrn1a=cmpt_dt_sn1a(strn1a,strn1b,data_strn1a);
                    data_strn1a=datastrn1a;

                    if(data_strn1a<0)
                            data_strn1a=0.0;

                    chazhi=data_strn1a-data_strn1b/10.0;

            }
            while(chazhi>0);

            // calculated minor strain
            strn2=rou_a*strn1a;

            // print result
            fprintf(fp," the stress ratio in A zone: %f\n",alfaa);
            fprintf(fp,"%f\t%f\n",strn2,strn1a);

            alfaa=alfaa+0.05;
    }
    fprintf(fp,"\n");
    fclose(fp);
}
```

## Étude numérique et expérimentale de AZ31-O feuille en alliage de magnésium formage à chaud

**RESUME :** Dans ce projet, le matériau est l'alliage de magnésium AZ31-O en tôle. L'épaisseur de tôles est de 1,2 mm. Les essais de traction à chaud sont réalisés afin d'étudier la ductilité de l'alliage de magnésium AZ31-O, la température et l'influence la vitesse de déformation sont incluses dans tous les tests. Le résultat d'analyse montre que la ductilité est renforcée avec une température croissante et une vitesse de déformation décroissante, le phénomène d'adoucissement est évident à la température élevée. La propriété anisotrope n'est pas considérée dans ce projet. Les essais Nakazima à chaud avec le poinçon d'hémisphère sont réalisés pour étudier la formabilité de l'alliage de magnésium AZ31-O. Enfin, la FLD (Forming Limit Diagram) est identifiée et les comparaisons montrent que la formabilité est préférable à une température plus élevée. En outre, les prédictions des limites de formage sont effectuées dans le modèle M-K. Les simulations des éléments finis sont effectuées pour un emboutissage par poinçon hémisphérique et un emboutissage en croix. Tout d'abord, les simulations d'emboutissage de poinçon hémisphérique sont réalisés sur FORGE® et sur ABAQUS®. Les résultats des simulations de FORGE et de ABAQUS sont comparés afin d'étudier la différence de divers codes de simulation des éléments finis. Deuxièmement, le comportement de d'endommagent est étudié dans FORGE par modèle d'endommagement Lemaitre. Enfin, la simulation d'emboutissage en croix qui est un benchmark de la conférence 2011 NUMISHEET est réalisée avec FORGE. La charge de poinçon, l'épaisseur et la distribution de température sont obtenues et comparées pour chaque simulation. En outre, ces résultats de la simulation de benchmark (FORGE) sont également comparés à d'autres logiciels de simulation en conférence.

**Mots clés :** En alliage de magnésium, AZ31, Thermo expérience mécanique, Nakazima emboutissage à chaud, Formabilité, La méthode des éléments finis.

## Numerical and experimental study of AZ31-O magnesium alloy warm sheet forming

**ABSTRACT :** In this project, the material is AZ31-O magnesium alloy sheet. The sheet thickness is 1.2mm. Warm tensile tests are performed to study ductility of AZ31-O magnesium alloy, the temperature and strain rate influence are included in all tests. The analysis result shows the ductility is enhanced with temperature increasing and strain rate decreasing, and the softening phenomenon is obvious at high temperature. The anisotropic property is not considered in this project. Warm Nakazima tests with hemisphere punch are performed to study formability of AZ31-O magnesium alloy. Finally, the FLD (Forming Limit Diagram) is identified and the comparisons distinctly show that the formability is better at higher temperature. Moreover, the forming limits predictions are performed in M-K model. Finite element simulations are performed for a hemisphere punch deep drawing and a cross-shaped deep drawing. Firstly, the hemisphere punch deep drawing simulations are performed in FORGE® and ABAQUS®. The simulation result from FORGE and ABAQUS are compared in order to study the difference of various finite element simulation codes. Secondly, the damage behavior is studied in FORGE by Lemaitre damage model. Finally, the cross-shaped deep drawing simulation which is a benchmark of NUMISHEET 2011 conference is performed with FORGE. The punch load, thickness and temperature distribution are obtained and compared for each simulation. Furthermore, this benchmark simulation results (FORGE) are also compared with other various simulation software in conference.

**Keywords** : Magnesium alloy, AZ31, Thermo mechanical experiment, Nakazima warm stamping test, Formability, Finite element method.

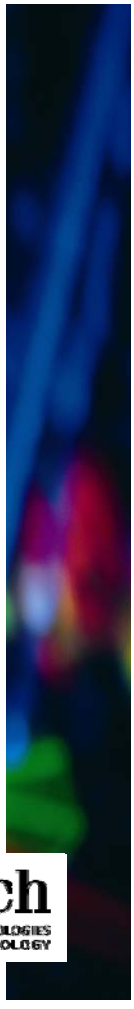

MINES ParisTech

ParisTech
INSTITUT DES SCIENCES ET TECHNOLOGIES
PARIS INSTITUTE OF TECHNOLOGY